HEAT TRANSFER ENHANCEMENT IN SINGLE-PHASE FORCED CONVECTION WITH BLOCKAGES AND IN TWO-PHASE POOL BOILING WITH NANO-STRUCTURED SURFACES

A Dissertation

by

HEE SEOK AHN

Submitted to the Office of Graduate Studies of
Texas A&M University
in partial fulfillment of the requirements for the degree of

DOCTOR OF PHILOSOPHY

May 2007

Major Subject: Mechanical Engineering

HEAT TRANSFER ENHANCEMENT IN SINGLE-PHASE FORCED CONVECTION WITH BLOCKAGES AND IN TWO-PHASE POOL BOILING WITH NANO-STRUCTURED SURFACES

A Dissertation

by

HEE SEOK AHN

Submitted to the Office of Graduate Studies of
Texas A&M University
in partial fulfillment of the requirements for the degree of

DOCTOR OF PHILOSOPHY

Approved by:

Co-Chairs of Committee,	Sai C. Lau
	Debjyoti Banerjee
Committee Members,	Nagamangala K. Anand
	Je C. Han
	Yassin A. Hassan
Head of Department,	Dennis O'Neal

May 2007

Major Subject: Mechanical Engineering

ABSTRACT

Heat Transfer Enhancement in Single-Phase Forced Convection with Blockages and
in Two-Phase Pool Boiling with Nano-Structured Surfaces. (May 2007)

Hee Seok Ahn, B.S.; M.S., Korea University

Co–Chairs of Advisory Committee: Dr. S. C. Lau
Dr. D. Banerjee

The first study researched turbulent forced convective heat (mass) transfer downstream of blockages with round and elongated holes in a rectangular channel. The blockages and the channel had the same cross section, and a distance equal to twice the channel height separated consecutive blockages. Naphthalene sublimation experiments were conducted with four hole aspect ratios (hole-width-to-height ratios) and two hole-to-blockage area ratios (ratios of total hole cross-sectional area to blockage area). The effects of the hole aspect ratio, for each hole-to-blockage area ratio, on the local heat (mass) transfer distribution on the exposed primary channel wall between consecutive blockages were examined. Results showed that the blockages with holes enhanced the average heat (mass) transfer by up to 8.5 and 7.0 times that for fully developed turbulent flow through a smooth channel at the same mass flow rate, respectively, in the smaller and larger hole-to-blockage area ratio (or smaller and larger hole diameter) cases. The elongated holes caused a higher average heat (mass) transfer and a larger spanwise variation of the local heat (mass) transfer on the channel wall than did the round holes.

The second study explored the heat transfer enhancement for pool boiling on nano-structured surfaces. Experiments were conducted with three horizontal silicon surfaces, two of which were coated with vertically aligned multi-walled carbon nanotubes (MWCNT) with heights of 9 and 25 μm, respectively, and diameters between 8 and 15 nm. The MWCNT arrays were synthesized on the two silicon wafers using chemical vapor deposition. Experimental results were obtained over the nucleate boiling and film boiling regimes under saturated and sub-cooled (5°C and 10°C) boiling conditions. PF-5060 was the test fluid. Results showed that the MWCNT array with a height of 25 μm enhanced the nucleate and film boiling heat fluxes on the silicon surface by up to 380% and 60%, respectively, under saturated boiling conditions, and by up to 300% and 80%, respectively, under 10°C sub-cooled boiling conditions, over corresponding heat fluxes on a smooth silicon surface. The MWCNT array with a height of 9 μm enhanced the nucleate boiling heat flux as much as the taller array, but did not significantly enhance the wall heat flux in the film boiling regime.

DEDICATION

To my father (in memoriam) and my mother

To my father-in-law and my mother-in-law

To my wife, *Mi Kyung*

To my daughter, *Yeo Won* and my son, *Keon Woo*

ACKNOWLEDGMENTS

I would like to gratefully acknowledge my graduate committee members: Dr. S. C. Lau, Dr. D. Banerjee, Dr. N. K. Anand, Dr. J. C. Han, and Dr. Y. A. Hassan. Their continued support and direction made my time at Texas A&M University pursuing a Ph.D. degree an immeasurably satisfying learning experience. Especially, I would like to thank my advisor, Dr. S. C. Lau, for supporting me during my entire study and giving me an opportunity to research and teach. Without his assistance, none of this would have been possible. I greatly appreciate my co-advisor, Dr. D. Banerjee, for supporting me and guiding me through a new field of study: micro-scale boiling. I sincerely thank Dr. N. K. Anand for his help throughout all aspects of my research. His guidance will never be forgotten. I am deeply indebted to Dr. J. C. Han for being a role model and providing me with invaluable knowledge of heat transfer. His passion toward his research is inspiring. I wish to express appreciation to Dr. Y. A. Hassan for being always helpful to me and generous with good advice. I appreciate all he did for me.

I deeply appreciate Dr. T. Lalk for giving me encouragement, guidance, and the opportunity to be an instructor. I cannot forget his kind advice and trust. Thank you, Mr. Y. Ramirez for helping me to conduct my experiments successfully. He is one of the nicest people I have ever met. My deep appreciation to Mr. M. Walker for helping me use machines when I built the experimental apparatus.

My gratitude goes to my colleagues at Texas A&M University: Mr. Sang W. Lee, Mr. Yong H. Lee, Mr. Sung H. Oh, Mr. K. Subramanian, and Mr. P. Venkata in the convective heat transfer lab, and Mr. N. Sinha and Mr. V. Sathyamurthi in

the multi-phase flow and heat transfer lab. I really appreciate their smiles and help with my experiments.

I am very thankful to my wife, Mi Kyung, who helped me during my studies, doing an outstanding job as a friend, a wife, and a mother of my beloved children, Yeo Won and Keon Woo. She was always with me whenever I needed her help. I am deeply grateful to my father (in memoriam) and mother for their love, prayers, and encouragement. They have never hesitated to sacrifice anything for my happiness. I am most grateful to my father-in-law and mother-in-law for supporting my family during my study. I cannot forget their love, efforts, and assistance. Thank you to my sister and her husband for praying for my family and guiding us in the right way. I am also thankful to my brothers-in-law and sisters-in-law for their love and assistance of my family.

The experimental set-up in Chapter III and the experiments in Chapter IV were built and conducted, respectively, by the author with the assistance of Mr. S. W. Lee, who assisted me when I built the experimental apparatus for heat transfer experiments and ran the experiments. I cannot forget a summer semester we spent together in the machine shop.

The experimental set-up in Chapter VII and the experiments in Chapter VIII were built and conducted, respectively, by the author with the assistance of various individuals. Dr. R. H. Baughman, Dr. M. Zhang, and Dr. S. Fang at the Nanotech Institute, University of Texas at Dallas, provided the carbon nanotube arrays after growing them on silicon wafers. Mr. N. Sinha provided the thin film thermocouples after fabricating them on a silicon wafer. Mr. V. Sathyamurthi assisted me when I conducted the boiling experiments on a bare silicon surface and carbon nanotube (9 μm and 25 μm) coated surfaces. He readily took turns whenever I needed his help and conducted 10°C sub-cooled boiling experiments for the 25 μm-height carbon

nanotube case. I am grateful to all of them for helping me conduct my experiments successfully. The FE-SEM acquisition was supported by the NSF under Grant No. DBI-0116835.

TABLE OF CONTENTS

CHAPTER Page

LIST OF TABLES

TABLE Page

LIST OF FIGURES

FIGURE Page

NOMENCLATURE

a	width of round or elongated holes in blockages, m
A_c	flow cross-sectional area of test channel, m^2
A_s	surface area, m^2
$A_{s,rd}$	surface area for round silicon wafer, m^2
$A_{s,rt}$	surface area for rectangular silicon wafer, m^2
b	center-to-center spacing between adjacent holes in blockages, m
C_{max}	experimental constant for calculating critical heat flux
C_{min}	experimental constant for calculating minimum heat flux
d	diameter of holes in blockages, m
D_h	hydraulic diameter of test channel, m
f	friction factor
f_0	reference friction factor for fully developed turbulent flow in smooth channel
g	gravitational acceleration, m/s^2
$\bar{h}$	average heat transfer coefficient, W/m$^2 \cdot$ K
h_{fg}	latent heat, kJ/kg
h_m	local mass transfer coefficient, m/s
$\bar{h}_m$	average mass transfer coefficient, m/s
H	height of test channel, m
I	current, A
k	thermal conductivity of air, W/m $\cdot$ K
$\dot{m}$	air mass flow rate, kg/s
$\dot{M}_n$	rate of total mass transfer from upstream naphthalene surface, kg/s

$\dot{M}_n''$	local naphthalene mass flux, $\mathrm{kg/m^2 \cdot s}$
Nu	local Nusselt number
$\overline{Nu}$	average Nusselt number
Nu_0	reference Nusselt number for fully developed turbulent flow in smooth channel
p	pressure, $\mathrm{N/m^2}$
$p_{v,w}$	vapor pressure on naphthalene surface, $\mathrm{N/m^2}$
Pr	Prandtl number
P_w	perimeter of test channel, m
q_{loss}	rate of extraneous heat losses, W
q''	wall heat flux, $\mathrm{W/m^2}$
q''_{max}	critical heat flux, $\mathrm{W/m^2}$
q''_{min}	minimum heat flux, $\mathrm{W/m^2}$
R_{th}	thermal resistance between boiling surface and top surface of heater, °C/W
$R_{t,rd}$	thermal resistance for round silicon wafer, °C/W
$R_{t,rt}$	thermal resistance for rectangular silicon wafer, °C/W
Re	Reynolds number
Sc	Schmidt number
Sh	local Sherwood number
$\overline{Sh}$	average Sherwood number
Sh_0	reference Sherwood number for fully developed turbulent flow in smooth channel
T	temperature, K
T_c	top surface temperature of heater, °C
$\bar{T}_m$	average bulk temperature, K

TP	thermal performance
T_s	boiling surface temperature, °C
T_w	wall temperature, K
$\bar{T}_w$	average wall temperature, K
$\bar{u}$	average velocity, m/s
V	voltage, V
$\dot{V}$	volumetric flow rate of air, m^3/s
W	width of the test channel, m

Greek Symbols

ΔM_n	total mass transfer from naphthalene surface to air, kg
Δp	pressure drop across two consecutive blockages, $\mathrm{N/m}^2$
Δt	duration of experiment, s
ΔT	axial temperature gradient along centerline of heater, K
Δx	distance between two pressure taps, m
Δy	axial distance between the thermocouples, m
Δz	local change of elevation on naphthalene surface, m
μ	dynamic viscosity of air, $\mathrm{N \cdot s/m}^2$
ρ	density of air, $\mathrm{kg/m}^3$
ρ_l	density of liquid, $\mathrm{kg/m}^3$
ρ_v	density of vapor, $\mathrm{kg/m}^3$
σ	surface tension, N/m
ω	Uncertainty

CHAPTER I

INTRODUCTION

A. Motivation of the First Study (Single-Phase Forced Convection with Blockages)

Moon and Lau [1] and Lau et al. [2] studied heat transfer for flow through blockages with holes in a turbine blade channel. As will be mentioned in Chapter II, however, Moon and Lau [1] focused their research on blockages with round holes, i.e., the effect of hole size and configuration of round holes on local heat transfer distribution on a channel wall and pressure drop across two consecutive blockages. In a similar fashion, but with a different wall temperature measurement technique, Lau et al. [2] focused their research on blockages with round and square holes, i.e., heat transfer enhancement on a channel wall by blockages with round and square holes. Therefore, it is interesting to investigate the effect of blockages with different hole shape (hole aspect ratio) and size (hole-to-blockage area ratio) on heat transfer on a channel wall and pressure drop across two consecutive blockages.

The objective of this study was to examine, for turbulent air flow through holes in blockages, the effects of the aspect ratio (width-to-height ratio) of the holes and the hole-to-blockage area ratio on average heat transfer and local heat transfer distribution on the two principal walls between consecutive blockages, and pressure drop across the blockages. These blockages were oriented perpendicular to the main flow direction in a wide rectangular channel and had the same cross section as the flow channel. Naphthalene sublimation experiments were conducted to obtain the average mass transfer and local mass transfer distribution for two flow rates corresponding to Reynolds numbers (based on the channel hydraulic diameter) of 7,000 and 17,000.

The journal model is *IEEE Transactions on Automatic Control.*

The heat and mass transfer analogy was used to relate the mass transfer enhancement to the heat transfer enhancement. Experiments using copper plate heaters with embedded thermocouples were also conducted to determine the average heat transfer on the channel wall at Reynolds numbers of 7,000, 12,000 and 17,000. During the experiments, pressure drops across two consecutive blockages were measured to estimate the thermal performance of the blockages.

B. Outline of the First Study (Single-Phase Forced Convection with Blockages)

As a new approach to blade internal passage cooling, blockages with staggered holes were introduced into a rectangular channel with an aspect ratio of 12 in the main stream direction to examine their effect on average and local heat transfer, friction factor, and thermal performance for turbulent flow at Reynolds numbers of 7,000, 12,000, and 17000. In this study, hole-to-blockage area ratios, 0.2 and 0.3, and hole aspect ratios, 1.0, 1.8, 2.6, and 3.4, were the main parameters of investigation. For a hole aspect ratio of one, the hole shape was a round type and, for the rest of the aspect ratios, the hole shape was an elongated type. For an average heat transfer on the channel walls, experiments using copper heaters with embedded thermocouples were conducted for eight different hole cases at three different Reynolds numbers ($Re = 7,000$, 12,000, and 17,000). For local heat (mass) transfer distribution on the channel walls, naphthalene sublimation experiments were conducted using two aluminum cassettes at two different Reynolds numbers ($Re = 7,000$ and 17,000). Pressure drops across two consecutive blockages were measured using a pressure transducer for the calculation of thermal performance, i.e., heat transfer per unit pumping power. The experiments that were conducted to study heat transfer and friction factor in a rectangular channel through blockages with various hole configurations are summarized as follows:

1. To estimate average heat transfer on the channel wall, experiments using copper heaters with embedded thermocouples were performed. In these experiments, hole-to-blockage area ratio and hole aspect ratio were the main parameters studied.
2. To study the heat transfer mechanism on the channel wall, detailed local heat transfer distribution on the channel walls were measured by using the naphthalene sublimation technique.
3. Pressure drops across two consecutive blockages with various hole configurations were measured to evaluate thermal performance of the blockages.

C. Motivation of the Second Study (Two-Phase Pool Boiling with Nano-Structured Surfaces)

1. Heat Transfer on Nano-Structured Surface

For heat transfer enhancement in pool boiling, nano-structured surface has been studied by a number of researchers. Recently, CNT were subjected to a boiling experiment because of their prominent thermal properties. The research on CNT for the application to pool boiling, however, was just launched. Except Ujereh et al. [3], no research on this topic has been reported. As will be discussed in Chapter VI, however, Ujereh et al. [3] focused their research on nucleate boiling under saturated conditions. They did not report the effect of the CNT on heat transfer in film boiling and under subcooled conditions. In their study, only one size of the CNT with 20-30 μm in length was examined to investigate the effect of the CNT on heat transfer enhancement in nucleate boiling. However, (1) the heat transport mechanism in film boiling is totally different from that in nucleate boiling. In film boiling, cold spots caused by liquid-solid contact are believed to transfer a major portion of the total heat flux. On the other hand, micro-layer evaporation, surface quenching, and convective bulk fluid motion are the dominant heat transport mechanism during nucleate boiling. (2) Sub-cooling is one of the major factors which can influence the boiling performance by condensing the departing bubbles in the nucleate and film boiling regimes. Sub-cooling also affects the heat transfer at the CHF and MHF points. (3) Size of the CNT is an important factor which may potentially affect the efficacy of heat transfer mechanisms during boiling, especially in film boiling. Film boiling on a horizontal surface encompasses hydrodynamic instabilities. The boiling process is considered to be related to Taylor instability wave behavior. According to Banerjee and Dhir [4, 5] and Banerjee et al. [6], the dynamic value of the minimum vapor film thickness of the wave for film boiling of PF-5060 was approximately 15-20 μm. Hence, it is meaningful to investigate how the height of MWCNT forests that are higher or shorter than the dynamic value of the minimum vapor film thickness affects the boiling performance under various conditions.

The objective of this study was to examine the efficacy in enhancing heat transfer on the MWCNT-deposited-surfaces in nucleate and film boiling under saturated and sub-cooled conditions. To study the effect of the MWCNT height on pool boiling heat transfer, two different heights of MWCNT were selected and examined. The heat transfer enhancement obtained by using the MWCNT was compared to the heat transfer data obtained from a smooth surface using a bare silicon wafer.

2. Surface Temperature Measurement Using TFT

To enhance heat transfer from a heated surface, arrays of multi walled carbon nanotubes were grown on silicon wafers and employed in pool boiling experiments. In this study, however, the wall temperature cannot be measured directly during the experiments due to the complicated morphology of the nano-structured surfaces. To solve this problem, a direct surface temperature measurement method used a micro-machined thin film thermocouple, fabricated on a silicon wafer. The measurement method selected must satisfy a number of requirements as follows:

- accurate surface temperature measurement is required to deduce the thermal resistance between the boiling surface (silicon wafer) and the top surface of the heater (copper cylinder).
- the measurement method should not cause vapor film disruption during the film boiling experiment. The device size (thermocouple junction), especially height, must be less than the dynamic value of the minimum film thickness.

Once the surface temperature data was recorded during the boiling experiment, the overall thermal resistance correlation was induced for predicting surface temperature for the experiments with MWCNT.

D. Outline of the Second Study (Two-Phase Pool Boiling with Nano-Structured Surfaces)

1. Heat Transfer on Nano-Structured Surface

The ultimate goal of this study was to investigate the effect of nano-structured surfaces on boiling heat transfer during saturated and subcooled pool boiling.

To study the effect of the MWCNT height on pool boiling heat transfer, two different heights of MWCNT (9 μm for Type-A MWCNT and 25 μm for Type-B MWCNT) were deposited on silicon wafers and examined. The heat transfer enhancement obtained by using the MWCNT was compared to the heat transfer data obtained from a smooth surface using a bare silicon wafer (this served as the control experiment). The test fluid was PF-5060 (manufacturer: 3M Company). The main component of the experimental apparatus consisted of one of the three silicon wafers held in place on the top of a copper cylinder. The cylinder was submerged in PF-5060, and cartridge heaters supplied heat to the copper cylinder. The wall heat flux was determined from the measured temperature distribution in the copper cylinder. The relationship between the wall heat flux and the wall superheat was determined for nucleate and film boiling on each silicon wafer surface.

2. Surface Temperature Measurement Using TFT

The target of this study was to measure the surface temperature of a smooth silicon wafer during nucleate and film boiling and to deduce the overall thermal resistance correlation for predicting surface temperatures for other applications (boiling experiments performed on MWCNT surfaces).

For this purpose, this supplementary experiment was conducted using a micro-machined K-type thin film thermocouple (TFT). The thermocouple was formed by Chromel and Alumel on a silicon wafer surface using the photolithography and metal deposition technologies. The thermocouple junction with 50 μm in width and 0.25 μm in height was designed to detect surface temperature fluctuations with a high temporal resolution during the boiling experiment. Adhesive bonding with silver paint technique was explored for packaging of the TFT. Using the temperature data recorded, the overall thermal resistance correlation between the boiling surface (silicon wafer) and the top surface of the heater (copper cylinder) was obtained. This correlation was used for predicting wall superheat values during the experiments with the MWCNT forests.

CHAPTER II

SINGLE-PHASE FORCED CONVECTION WITH BLOCKAGES: LITERATURE REVIEW

A. Background

Cooling of turbine vanes and blades is critical to implement the requirements of high turbine inlet temperature to increase the performance of gas turbine engines. Increasing turbine inlet temperature is one of the most effective methods to enhance the thermal efficiency of turbine engines. The ability to increase the turbine inlet temperature depends on the improvement of cooling technology as well as the developing technology of super-alloys. According to Takeishi [7], cooling technology improves turbine inlet temperature by 25°C per year, whereas the developing technology of super-alloy accomplishes only 10°C per year. Hence, it can be concluded that the contribution of cooling technology to improve the thermal efficiency of gas turbine engines is superior to that of the developing technology of super-alloys.

As a major cooling method in turbine blades, a number of internal cooling technologies have been developed and used by supplying air from a compressor to the internal channel of the turbine blades. In the early stages of developing turbine engines, only an impinging jet to the surface of the blades was used in the vicinity of leading edges because the turbine inlet temperature was not so high as to necessitate the use of other cooling technologies at this time. As the turbine inlet temperature was gradually increased for high turbine performance, however, a number of turbulators, ribs through serpentine passages, and pin fins near trailing edges, were employed. The cooling air which enters the internal passages of the blades removes heat from the inner-side wall as it passes the ribs or pin fins before it exits the stationary vanes or rotating blades through film cooling holes.

B. Experimental Methodology

From a turbine blade designer's point of view, it is very important to keep the maximum metal temperature of the turbine blades under the allowable metallurgical temperature limit for reliable operation and to lower the metal surface temperature with a minimum of cooling air for the improvement of turbine engine efficiency. For this purpose, designers need to predict the average temperature level and local temperature distribution on the blade walls with high accuracy by performing a heat transfer analysis. Various methods for measuring the wall temperature under steady state and transient conditions have been developed by a number of researchers, among which the representative methods are: (1) heater with thermocouple method, (2) thermochromic liquid crystal method, (3) naphthalene sublimation method.

Han and Park [8] and Han and Zhang [9] conducted their experiments with the foil heater and thermocouple method to investigate local heat transfer distribution in rectangular channels and regional average heat transfer in a square channel, respectively, with various rib turbulators for fully developed turbulent flow. VanFossen [10] used commercially available electric heaters encased in a polymide base film and thermocouples to study heat transfer enhancement in a rectangular channel with staggered arrays of short pin fins. Even though one can measure local temperature distribution on a turbine blade surface with a great number of thermocouples, this technique is appropriate for regional average wall temperature measurement due to its spatial resolution limitation.

Thermochromic liquid crystal behaves in a way that the structure allows the crystal to reflect incident light over the visible light wavelength range when the crystal is at a specific temperature. The temperature measurement technique with thermochromic liquid crystal is one of the common methods used for observing local heat transfer distribution on channel walls under a steady or transient condition and is classified as a steady state technique and a transient technique. Taslim and Spring [11] employed the steady state thermochromic liquid crystal technique to investigate the effect of profile and spacing of transverse ribs on local heat transfer distribution in a channel. Kukreja and Lau [12] presented local heat transfer distribution for turbulent flow in rib-roughened turbine blade internal cooling passages with the transient thermochromic liquid crystal technique.

Using the heat and mass transfer analogy, the naphthalene sublimation method has been employed to measure heat (mass) transfer distribution on a turbine blade channel wall. This technique provides a relatively high resolution with no heat loss and axial conduction effect. Kukreja et al. [13] and Lau et al. [14] used the naphthalene sublimation method to study local heat (mass) transfer distribution in a square channel with full and V-shaped ribs, and in a rectangular channel with pin-fins, respectively. By employing the naphthalene sublimation method, Lau et al. [2] studied heat transfer enhancement on a channel wall by blockages with staggered round and square holes for turbulent airflow in a rectangular channel.

C. Review of Prior Research on Internal Channel Cooling

1. Rib-Roughened Wall

According to the survey results presented by Han et al. [15] and Lau [16], the study of heat transfer enhancement in a channel has been conducted by many researchers in the field by using turbulent promoters which include ribs and pin fins, and impinging jets, with and without channel rotation. There have been a number of studies of heat transfer enhancement for internal channel flow using ribs of various configurations and parameters which include channel aspect ratio, rib height-to-hydraulic diameter ratio, rib pitch-to-height ratio, rib height-to-width ratio, rib-angle-of attack, and blockage ratio.

Han and Park [8] investigated the effect of rib angle-of-attack and channel aspect ratio on local heat transfer in rectangular channels with two opposite rib-roughened walls. In their experiments, the rib angles-of-attack of 90° , 60° , 45° and 30° and channel aspect ratios of 1, 2 and 4 were examined with small channel length-to-hydraulic diameter ratios, ranging from 10 to 15. Results showed that the ribs with an angle-of-attack of 60° drew the highest average Nusselt number, accompanied by the highest friction, for the rectangular channels with aspect ratios of 1 and 2, whereas the transverse ribs caused the highest average Nusselt number for the rectangular channel with an aspect ratio of 4. They postulated that these results were caused by the secondary flow induced by the angled ribs. For the rectangular channel with aspect ratios of 1 and 2, the secondary flow with swirl motion enhanced the wall heat transfer. As the channel aspect ratio was increased, however, the secondary flow caused by the ribs with angle-of-attack on both the top and bottom walls cancelled out each other due to the reduced channel height. They also concluded that the ribs with an angle-of-attack of 30° for the square channel and 45° for the rectangular channels with aspect ratios of 2 and 4 have the highest heat transfer per unit pumping power.

Lau et al. [17] examined the heat transfer, friction factor, and thermal performance for turbulent flow in square channels with many different angles-of-attack of V-shaped ribs on two opposite walls. The angles-of-attack of the rib arrays considered in this study were 45° , 60° , 90° , 120° , and 135° and rib pitch-to-height ratios were 10 and 20, with parallel or crossed rib arrays on the two opposite walls. The authors concluded that the 60° V-shaped ribs with a rib pitch-to-height ratio of 10 had the highest ribbed wall and smooth wall heat transfer and thus high thermal performance, which was superior to the 60° full ribs, even though it caused a higher pressure drop than the corresponding angled full ribs and transverse full ribs. However, the reverse V-shaped ribs, having rib angles-of-attack more than 90° , showed high pressure drops and low thermal performances. They also postulated that the rib crossing on the two opposite walls enhanced neither heat transfer from the channel walls nor thermal performance. Doubling the rib pitch-to-height ratio decreased the rib wall heat transfer, smooth wall heat transfer, friction factor, and thermal performance.

Kukreja and Lau [13] conducted experiments to measure local heat transfer for turbulent flow through a straight square channel with solid and perforated ribs on two opposite walls. They conducted their experiments with 90° and 60° solid and perforated full ribs and 60° solid V-shaped ribs, having a height-to-hydraulic diameter ratio of 0.125 and a rib pitch-to-height ratio of 10, on the channel walls. They determined that the perforated ribs enhanced less overall heat transfer than the solid ribs because the jet stream passing through the holes weakened the flow reattachment on the wall downstream of a rib. Although the perforated ribs caused a lower pressure drop, replacing the solid ribs with the perforated ribs did not improve thermal performance. Results showed that increasing the size of the holes, the number of holes, or the total hole area did not improve the overall heat transfer. They also recommended V-shaped ribs for the internal cooling of gas turbine blades.

Buchlin [18] conducted her experiment with five different shapes of perforated ribs and presented the effect of the configuration of the perforation, pitch of the perforated ribs, and open area ratio (ratio of the clearance area to the total frontal area of the ribs) on heat transfer on a wall in a wind tunnel. The author observed an increase of the local heat transfer immediately downstream of the perforated ribs when compared with the corresponding local heat transfer for the solid ribs and recommended an optimal design with a chevron type perforation of the ribs.

A critical consideration in designing a cooled turbine airfoil is the restriction in size and shape of the leading and trailing edges due to the aerodynamics of the airfoil. In this respect, the turbulator blockage ratio (or height-to-channel hydraulic diameter ratio), as one of the major design factors for internal passage cooling, can be frequently greater than 0.2. Bailey and Bunker [19] examined the effect of the turbulator blockage ratios, ranging from 0.193 to 0.333, on heat transfer and friction factor of the channel walls. The authors conducted their experiment with 45° staggered turbulators in a rectangular channel having an aspect ratio of 0.4 while keeping turbulator pitch-to-height ratio constant at 10 for all rib geometries. They speculated that turbulators with a high blockage ratio enhanced Nusselt number up to 3.6 when compared with that of a smooth channel, whereas the turbulators accompanied the increase in friction factor of as much as 65. For the channel with high blockage-ratio-turbulators on two opposite walls, Nusselt number for the 45° turbulators was lower than that of the 90° transverse turbulators at a given blockage ratio.

2. Channel with Pin-fins

Due to the shape and size of the trailing edges of gas turbine blades, use of pin fins has been the most effective method to increase internal heat transfer in the parts of the blades. By increasing internal wetted surface area and turbulence intensity, pin fins enhance the heat transfer from walls to flowing air which passes in between the consecutive pin fins aligned in each row. The main parameters to be considered in this cooling technology include pin height-to-diameter ratio, streamwise pin spacing-to-diameter ratio, and spanwise pin spacing-to-diameter ratio.

A review of staggered array pin fin heat transfer and friction factor in turbine cooling application was conducted by Armstrong and Winstanley [20]. The authors presented the effect of geometric parameters such as pin height-to-diameter ratio and pin spacing on heat transfer and friction factor. After their review of the prior research of VanFossen [10], Metzger and his associates [21, 22, 23, 24], and Zukauskus [25], they concluded that the average heat transfer over pin fins array correlates with Reynolds number to a power of 0.6 and 0.7, depending on pin height-to-diameter ratio. Based on the research of Brigham and VanFossen [26], the results showed that heat transfer was not affected by the pin height-to-diameter ratio for the ratio less than two, whereas heat transfer increased by increasing the pin height-to-diameter ratio for a ratio greater than two. They speculated that the heat transfer for short pin fins was dominated by the endwall interaction, whereas the heat transfer for long pin fins was dominated by the cylinder interaction which improved the heat transfer in long pin fins. For friction factor, they recommended Metzger's correlation [23] for a large range of pin height-to diameter ratios and pin spacings.

With regard to channel cooling in the trailing edge region of turbine blades, some of the cooling air exits the channel through small ejection holes along the trailing edge and the rest through the blade tip. Studies of heat transfer and pressure drop in a pin fin channel with ejection holes were conducted by Lau et al. [27, 28]. The authors presented overall heat transfer and pressure drop results for a number of channels with ejection hole/slot geometries. Lau et al. [29] demonstrated the effect of lateral flow ejection on heat transfer and friction factor for turbulent flow in pin fin channels. With a rectangular channel that had staggered arrays of eight streamwise rows of pins with a pin height-to-diameter ratio of 1 and a spanwise pin spacing of 2.5 forming an array of equilateral triangles, the authors investigated segmental heat transfer results for various sizes and numbers of ejection holes through the side wall of the test section. They postulated that, when air exited through the ejection holes, the regional heat transfer dropped much faster along the segments in a streamwise direction than a straight-flow-only case (without ejection holes in the channel) due to the reduction in the mass flow rate that exited through the channel outlet. The results also showed that increasing the size or number of the ejection holes decreased the channel heat transfer and the overall channel friction factor.

3. Channel with Blockages

Using blockages with holes as a different type of turbulator, the cooling air is forced to flow to the blockage wall and then hit the surface of the wall to give an impinging effect to the surface. Although the blockages with holes tend to increase the pressure drop across the blockages, the effect of impinging of the cooling air to the wall combined with the vigorous mixing of the flow gives a significant enhancement of convective heat transfer from the wall of turbine blades.

Moon and Lau [1] presented heat transfer between blockages with holes for turbulent flow in a rectangular channel with the liquid crystal technique. They conducted their experiments with nine different staggered arrays of holes in the blockages to see the effect of the hole configurations on heat transfer on the channel wall. With the hole configurations they tested, they found that the blockages enhanced heat transfer by five to eight times compared to a smooth channel but significantly increased pressure drop across the blockage. Because of the large pressure drop, the heat transfer per unit pumping power was lower with the blockages than without them. The local heat transfer distribution was strongly dependent on the configuration of the hole array in the blockages.

Lau et al. [2] studied heat (mass) transfer enhancement on a channel wall by blockages with staggered round and square holes for turbulent airflow in a rectangular channel. The authors used the naphthalene sublimation method to measure average and local heat (mass) transfer on the wall and determined that the blockages enhanced the average heat transfer on the wall by five to six times and increased pressure drop by up to 490 times that for fully developed turbulent flow through a smooth channel. The blockages with square holes enhanced more heat transfer on the wall than the blockages with round holes.

CHAPTER III

SINGLE-PHASE FORCED CONVECTION WITH BLOCKAGES: EXPERIMENTAL APPARATUS AND PROCEDURE

A. Experimental Apparatus

1. Mass Transfer Measurement

The main components of the test apparatus for this study were the test section, a settling chamber, an orifice flow meter, a control valve, and two centrifugal blowers (Fig. 1). The test section was a rectangular channel that had a cross section of 30.5 cm (width) by 2.54 cm (height), and thus, an aspect ratio of 12:1. The walls of the test section were constructed of 1.27-cm thick oak plywood. As shown in the schematic of the top view of the test section with the top wall removed in Fig. 2, there were four blockages with round or elongated holes in the test section. These blockages had the same cross section as the cross section of the test section. They were constructed of acrylic and were 1.14-cm thick, and the distance between consecutive blockages was equal to 5.08 cm, or, two times the height of the channel. Figure 2 also shows that the holes in consecutive blockages were staggered to induce secondary flows, as air passes through the blockages during the experiments, to enhance the mass transfer on the exposed surfaces of the primary walls of the test channel. For this study, the round or elongated holes in the four blockages had a diameter of either 1.27 cm or 1.91 cm, or, $\frac{1}{2}$ or $\frac{3}{4}$ of the height of the channel. There were eight sets of blockages with different hole configurations. Figures 3 and 4 show the blockages with holes that had diameters of 1.27 cm and 1.91 cm, respectively. Table I lists the dimensions of the holes and the spacings between holes in the various blockages. While the aspect ratio of the holes ranges from 1.0 (round holes) to 3.4, and the total number of holes varied from 2 to 12, the ratios of the total hole-to-blockage areas were kept constant, and were equal to about 0.2 and 0.3, respectively, in the $d = 1.27$ cm and $d = 1.91$ cm cases.

The first blockage was located at 26.0 cm from the entrance and the distance between two successive blockages was 5.08 cm, which equals two times the height of the channel. In order to give impinging effect and to increase mixing rate of the air, the holes were arrayed staggeringly in each blockage as shown in Figs. 3 and 4.

In this study, two different cases, i.e., Case S and Case L, classified by the hole-to-blockage area ratio, defined as the ratio of total hole cross-sectional area to blockage area perpendicular to the main stream direction, were considered. The hole-to-blockage area ratios considered in this study were 0.2 for Case S and 0.3 for Case L. In accordance with the hole aspect ratio, defined as hole-width-to-height ratio, each case is sub-divided by four different cases: i.e., Case S-1 to Case S-4 for Case S (small hole-to-blockage area ratio) and Case L-1 to Case L-4 for Case L (large hole-to-blockage area ratio). The hole aspect ratios considered in this study were 1.0, and 1.8, 2.6 and 3.4.

The top wall of the test channel consisted of three rectangular slots into each of which a removable section of the top wall may be inserted (Fig. 1). To facilitate the measurements of the overall mass transfer coefficient and the distribution of the local mass transfer coefficient on the exposed surface of one of the primary walls between two blockages, two naphthalene cassettes were inserted into the slot between the two blockages in the top wall. Each cassette was constructed of aluminum and was about half as wide as the test channel. Each cassette had a 2.0-mm-deep cavity that was filled with naphthalene during a casting process. Once installed, the two cassettes rested side by side in the slot, on top of the two blockages and the test channel sidewalls, exposing a smooth, flat, naphthalene surface. Each naphthalene

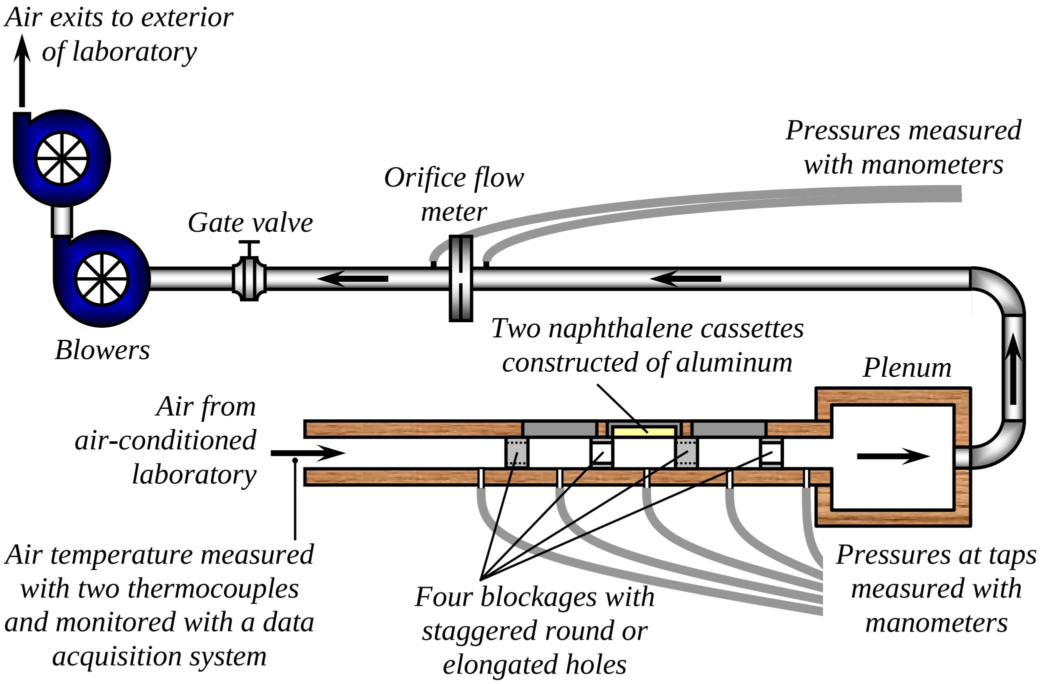

Fig. 1. Schematic of experimental apparatus for mass transfer experiments (not to scale).

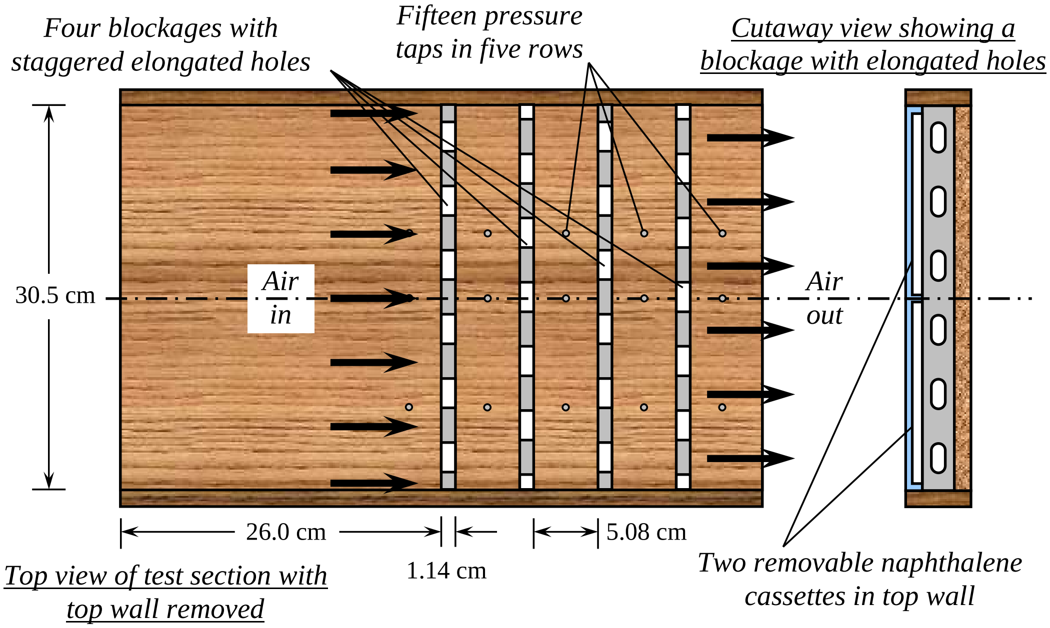

Fig. 2. Schematic of test section showing four blockages with elongated holes and naphthalene cassettes in top wall for mass transfer experiments.

Table I. Dimensions of staggered hole arrays in the blockages in this study.

Smaller holes, $d = 1.27$ cm	Case S-1	Case S-2	Case S-3	Case S-4
Number of holes	12	6	4	3
Shape of holes	Round	Elongated	Elongated	Elongated
Width of holes, “a” (cm)	1.27	2.27	3.27	4.27
C-to-C spacing, “b” (cm)	2.54	5.08	7.62	10.2
Cross-sectional Area (cm^2)	1.27	2.53	3.80	5.07
Hole-to-blockage area ratio	0.2	←	←	←
Hole aspect ratio	1.0	1.8	2.6	3.4

Larger holes, $d = 1.91$ cm	Case L-1	Case L-2	Case L-3	Case L-4
Number of holes	8	4	3	2
Shape of holes	Round	Elongated	Elongated	Elongated
Width of holes, “a” (cm)	1.91	3.40	4.90	6.40
C-to-C spacing, “b” (cm)	3.81	7.62	10.7	15.2
Cross-sectional Area (cm^2)	2.85	5.70	8.55	11.4
Hole-to-blockage area ratio	0.3	←	←	←
Hole aspect ratio	1.0	1.8	2.6	3.4

Blockages with twelve 1.27-cm round holes

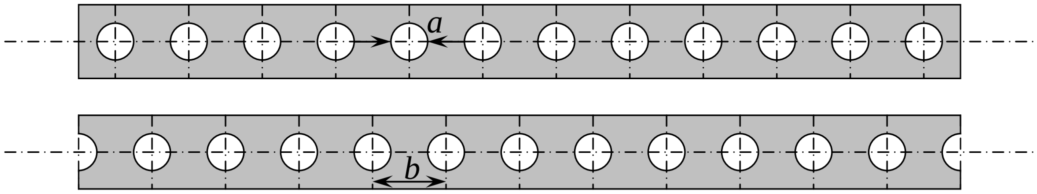

Blockages with six 2.27 cm × 1.27 cm elongated holes

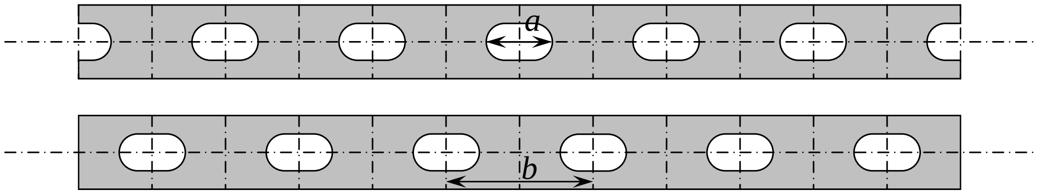

Blockages with four 3.27 cm × 1.27 cm elongated holes

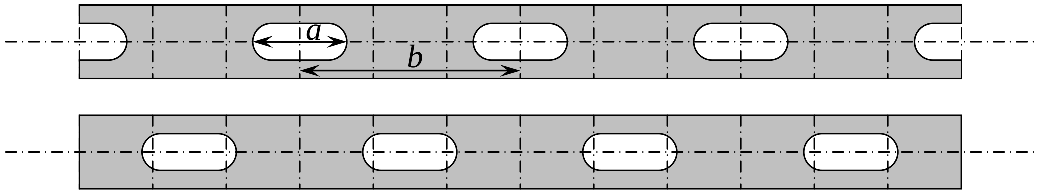

Blockages with three 4.26 cm × 1.27 cm elongated holes

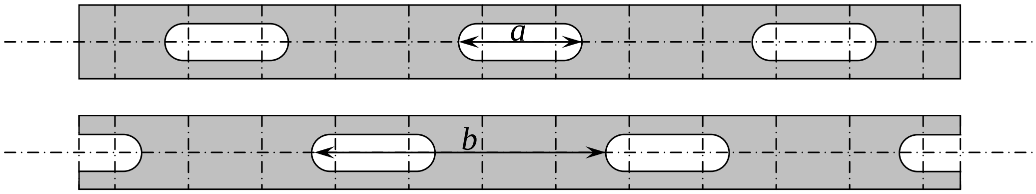

Fig. 3. Blockages with round or elongated holes for Case S installed in test section to improve heat transfer rate: diameter of holes equals 1/2 of channel height.

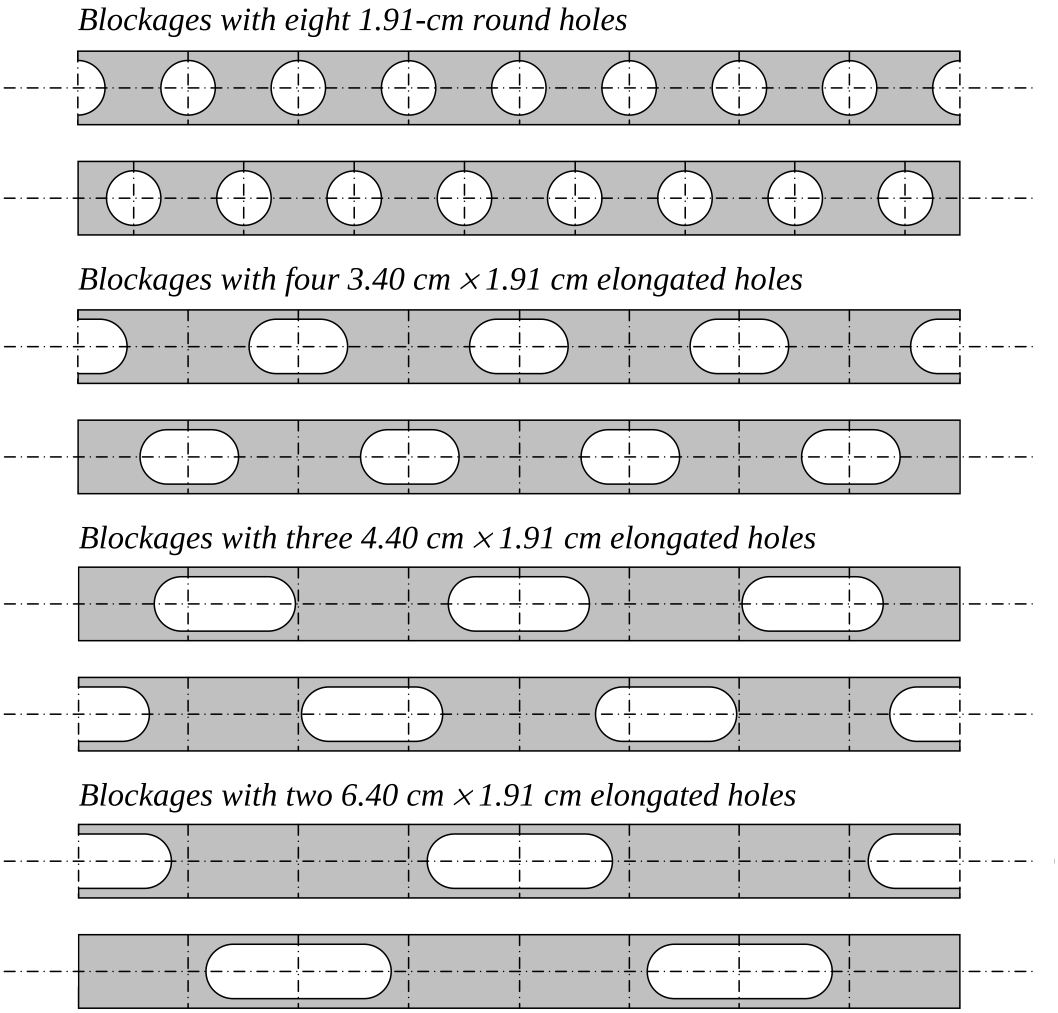

Blockages with eight 1.91-cm round holes

Blockages with four 3.40 cm × 1.91 cm elongated holes

Blockages with three 4.40 cm × 1.91 cm elongated holes

Blockages with two 6.40 cm × 1.91 cm elongated holes

Fig. 4. Blockages with round or elongated holes for Case L installed in test section to improve heat transfer rate: diameter of holes equals 3/4 of channel height.

surface with 14.54 cm long and 5.08 cm wide covered half of the area of the top wall between two consecutive blockages.

During an experiment, mass was transferred from the naphthalene surfaces of the two cassettes to the air that flowed through the test channel and the holes in the blockages, but all other surfaces exposed to the air were mass transfer inactive. To prevent air leakage, balsa wood was used at every contact surfaces of the cassettes and a number of weights were put on the cassettes to press them against the blockages during an experiment.

The two naphthalene cassettes were designed so that they could be quickly inserted into and removed from one of the three slots in the top wall. At the beginning and at the end of an experiment for determining the average mass transfer coefficient, the cassettes were weighed one at a time with a Sartorious electronic balance, which has a range of up to 160.0 g and a resolution of 0.1 mg.

To determine the distribution of the local mass transfer coefficient in an experiment, the elevations on the naphthalene surface and on the top surface of the rim of each cassette were measured with a Starrette electronic depth gage at the beginning and at the end of the experiment. The depth gage has a lever type LVDT head, a range of ±0.2 mm, and a resolution of 0.002 mm. A Velmax NF90 controller, two stepper motors, a desktop computer, National Instruments data acquisition hardware, and a LabView computer program were used to move the cassette on a coordinate table into position to facilitate the elevation measurements and to record the output from the electronic depth gage. The elevation measurements on the top surface of the rims of the cassette were needed to determine two reference planes of the naphthalene surface for calculating the elevation changes at the 960 points of the naphthalene surface. Fig. 5 shows the automated data acquisition system and the computer that were used in this study.

During an experiment, air was drawn into the test channel from the air-conditioned laboratory and exited the test apparatus to the outside of the building in which the laboratory is located. The temperature of the air was measured with two thermocouples and monitored with the computer controlled data acquisition system throughout the duration of the experiment. These thermocouples were calibrated with a constant temperature bath against a calibrated standard that was traceable to NIST. Also, before each experiment, the electronic depth gage and the electronic balance were calibrated with calibration standards that were supplied by the respective manufacturer.

2. Heat Transfer Measurement

The test section for this study was a rectangular channel with a cross section of 30.5 cm (width) by 2.54 cm (height), and thus, an aspect ratio of 12:1. The walls of the test section were constructed of 1.27-cm thick oak plywood. As shown in the schematic of the side view of the test section in Fig. 6, there were four blockages with staggered round or elongated holes in the test section. These blockages were constructed of acrylic. They had the same height as the channel and were 1.14-cm thick. The distance between two consecutive blockages was 5.08 cm, or twice the height of the channel.

For this study, there were eight sets of four blockages with different hole configurations, and the holes had a height (or diameter, in the round hole case) of either 1.27 cm or 1.91 cm. Table I lists the widths of the holes and the center-to-center spacings between holes in the various blockages. While the aspect ratio of the holes ranged from 1.0 (round holes) to 3.4, and the total number of holes varied from 2 to 12, the ratios of the total hole-to-channel cross-sectional areas were kept constant, and were equal to about 0.2 and 0.3, respectively, in the smaller and larger hole cases. Figure

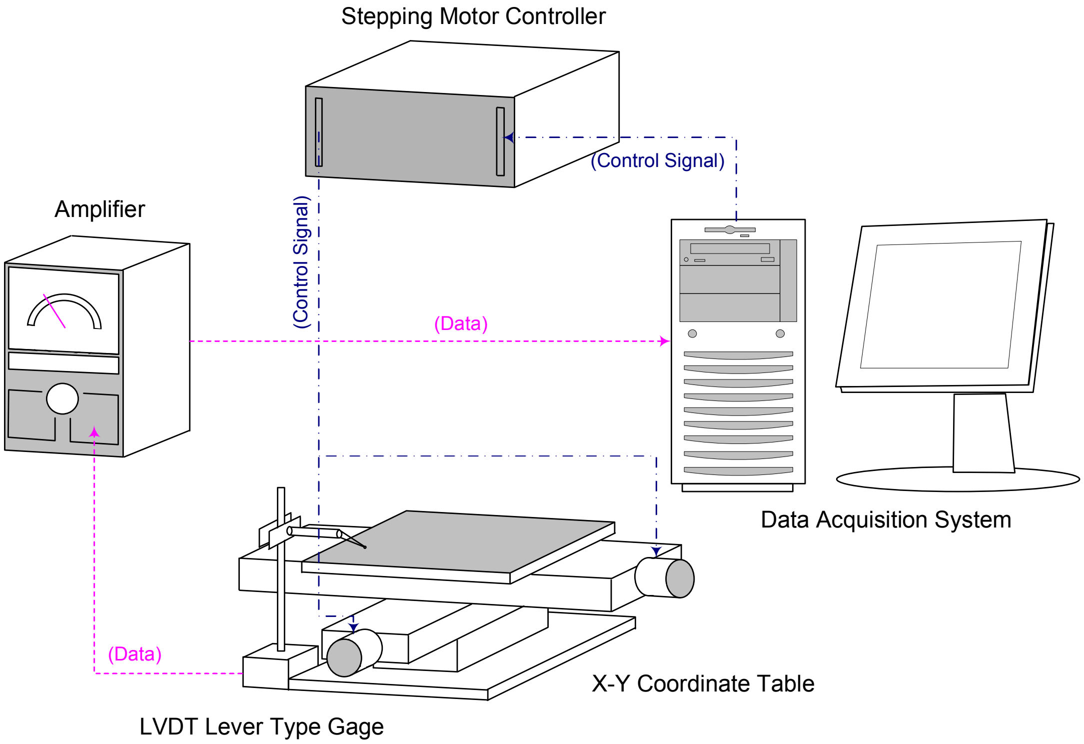

Fig. 5. Automated local mass transfer measurement system.

3 and 4 show two of each set of these blockages with staggered holes.

Air was the working fluid. During an experiment, it was drawn through the test section with two centrifugal blowers that were connected in series. After the air left the test section, it passed through a settling plenum, an orifice flow meter, and a gate valve and a bypass valve, before it was ducted to the outside of the laboratory.

Figure 7 shows the top views of the top and bottom walls of the test section. To determine the average heat transfer on one of the two principal walls of the test section downstream of the blockages, three copper plates were installed in three slots in the top wall of the test section. Each copper plate measured 5.08 cm by 30.5 cm and was 1.27 cm thick. During an experiment, heat was supplied to each copper plate from a flexible electric heater that was attached with silicon rubber adhesive onto the outer surface of the copper plate. Balsa wood with a thickness of 3.2 mm was attached, also with silicon rubber adhesive, onto the four edges of each copper plate. After the copper plate was installed in one of the three slots in the top wall of the test section, the wooden rim rested on top of the two blockages and the two sidewalls, such that the balsa wood minimized the heat transfer by conduction to the acrylic blockages. Styrofoam insulation was used to minimize extraneous heat losses to the surroundings, and silicon sealant was used to prevent air leakage at the interfaces between the copper plates and the top wall.

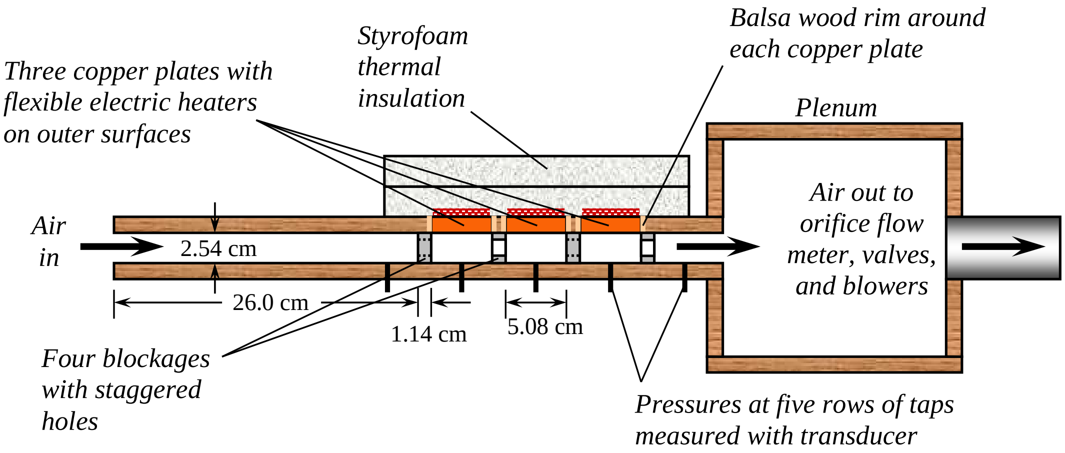

Fig. 6. Schematic of experimental apparatus for heat transfer experiments (not to scale).

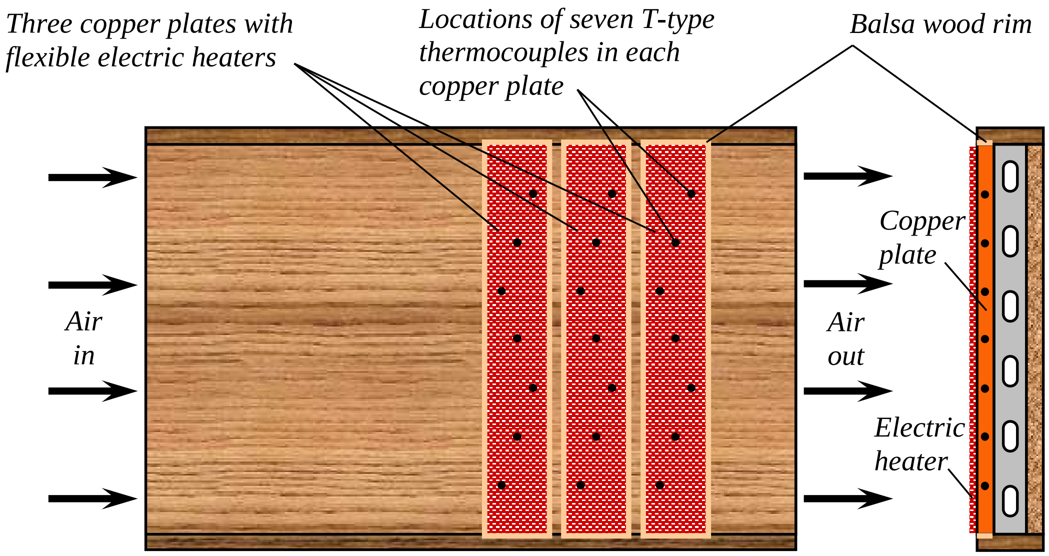

(a) ***Top view of top wall of test section***

(c) ***End view of test section showing a blockage with elongated holes***

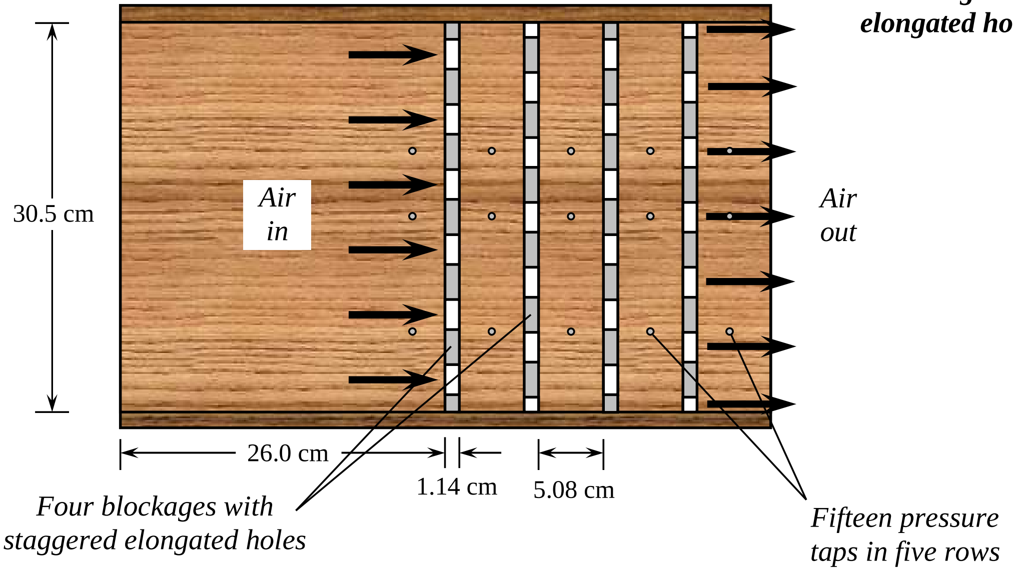

(b) ***Top view of bottom wall of test section with top wall removed***

Fig. 7. Schematic of top and bottom walls of wide (12:1) rectangular channel with four blockages for heat transfer experiments.

B. Experimental Procedure

Local heat (mass) transfer distribution with the naphthalene sublimation technique and average heat transfer measurement employing copper heaters with thermocouples technique were conducted as described in this section.

1. Mass Transfer Measurement

a. Naphthalene Molding

The naphthalene cassettes were prepared by a casting process. A number of solid naphthalene pieces (Manufacturer: Willert Enoz Mothball) were placed into a glass beaker. A hot plate was used to melt the naphthalene until it began to boil. While the naphthalene was melting, one of the aluminum cassettes was pre-heated on the hot plate for 10 seconds. Then the cassette was placed on a highly polished, flat stainless steel plate to form a mold. A funnel and two tubes were place on pre-drilled holes and then the cassette was secured to the plate with a weight. When the naphthalene was boiling, it was removed from the hot plate. Molten naphthalene was then poured through the funnel into the cavity of the cassette. After the naphthalene solidified, the weight, the tubes, and the funnel were removed from the cassette. The cassette was separated from the plate by tapping on one side with a hammer. The exposed naphthalene surface on the cassette must be as smooth as the surface of the highly polished stainless steel plate. The other aluminum cassette was prepared in the same way. To ensure that the naphthalene in the cassettes was in thermal equilibrium with the air in the air-conditioned laboratory, the cassettes were stored in sealed plastic bags in the laboratory for approximately 12 hours before an experiment.

b. Mass Transfer Experiment

For the average mass transfer measurement, each naphthalene cassette was weighed before and after an experiment was run. The weighing process was repeated five times for uncertainty analysis. The difference between the average weights gave the mass transfer from the naphthalene surface to the air flow during the experiment. The rate of mass transfer was used to calculate the average mass transfer coefficient on the naphthalene surface.

To determine the distribution of the local mass transfer coefficient in an experiment, each cassette was affixed onto the top plate of the x-y coordinate table, then the elevations at a grid of 1,100 points (50×22) on the naphthalene surface and on the top surface of the rim of each cassette were measured with the electronic depth gage immediately before and after the experiment. The automated local elevation measurement process took about 30 minutes per cassette. The elevation differentials at the grid points were calculated to determine the local mass transfer distributions on the channel wall.

Average and local mass transfer measurements were conducted for turbulent air flow rates which corresponded to two Reynolds numbers of approximately 7,000 and 17,000. At the beginning of each experiment, the liquid levels of the manometers were adjusted to zero. For each experiment, the Reynolds number was carefully set by regulating the control valve in the flow loop so that the pressure drop across the orifice meter indicated by the inclined manometer closely corresponded to the predetermined Reynolds number. During each experiment, the air temperature at the test channel entrance, ambient temperature, the pressure upstream of the orifice meter, and the pressure drop across the orifice meter were recorded every 5 minutes.

Supplementary experiments were conducted to determine the amounts of mass transfer during blower startup and shutdown for the experiments. The mass transfer corrections were needed because the duration of an experiment was defined as the period of time during which air flowed steadily through the test channel.

2. Heat Transfer Measurement

For each experiment, after a steady state was attained, the heater voltage drops and currents were measured with two TRMS digital multimeters. The temperature of each of the three copper plates was measured with seven 36-gage T-type thermocouples along with a computer-controlled data acquisition system. The pressure drops across the blockages were measured with fifteen static pressure taps at five streamwise stations along with a calibrated pressure transducer. Figure 7 shows the locations of the twenty-one thermocouples in the three copper plates and the locations of the fifteen static pressure taps at five streamwise stations in the bottom channel wall.

Experiments were conducted with each set of blockages to obtain the average heat transfer coefficient on the wall segments downstream of the blockages and the pressure drops across the blockages for three air mass flow rates corresponding to Reynolds numbers of about 7,000, 12,000, and 17,000. Separate experiments were conducted to calibrate the instruments for measuring the air mass flow rate, the wall and air temperatures, and pressures, and to determine the extraneous heat loss to the surroundings.

C. Data Reduction

1. Mass Transfer Measurement

The average and local mass transfer coefficients were defined, respectively, as

$$\bar{h}_m = \frac{\Delta M_n/\Delta t}{A_s(\rho_{v,w} - \overline{\rho}_{v,b})} \tag{3.1}$$

$$h_m = \frac{\dot{M}_n''}{\rho_{v,w} - \rho_{v,b}} = \frac{\rho_s \Delta z/\Delta t}{\rho_{v,w} - \rho_{v,b}} \tag{3.2}$$

where ΔM_n is the net mass transfer from a naphthalene surface to the air in [kg], $\dot{M}_n''$ is the local naphthalene mass flux in [kg/m$^2 \cdot$ s], Δz is the local change of elevation on the naphthalene surface in [m], Δt is the duration of the experiment in [s], and ρ_s is the density of solid naphthalene in [kg/m^3]. In the above equations, $\rho_{v,w}$ is the local vapor density of naphthalene at the wall in [kg/m^3], and was evaluated using the ideal gas law, in which the vapor pressure was determined using the vapor pressure-temperature correlation for naphthalene by Ambrose et al. [30].

$$T_w log(p_{v,w}) = \frac{a_0}{2} + \sum_{s=1}^{3} a_s E_s(x) \tag{3.3}$$

with

$$E_1(x) = x, \quad E_2(x) = 2x^2 - 1, \quad and \;\; E_3(x) = 4x^3 - 3x \tag{3.4}$$

where $a_0 = 301.6247$, $a_1 = 791.4937$, $a_2 = -8.2536$, $a_3 = 0.4043$ and $x = (2T_w - 574)/114$. The vapor pressure correlation by Ambrose et al. [30] is shown in Fig. 8

The average bulk vapor density of naphthalene, $\overline{\rho}_{v,b}$, in Eq. 3.1 is the average of the bulk vapor densities at the upstream and downstream edges of the naphthalene surface in [kg/m^3], and was calculated as

$$\bar{\rho}_{v,b} = \frac{1}{2}\left[\left(\frac{\dot{M}_n}{\dot{V}}\right)_{upstream} + \left(\frac{\dot{M}_n}{\dot{V}}\right)_{downstream}\right] \tag{3.5}$$

The bulk vapor density was equal to zero upstream of the naphthalene surface,

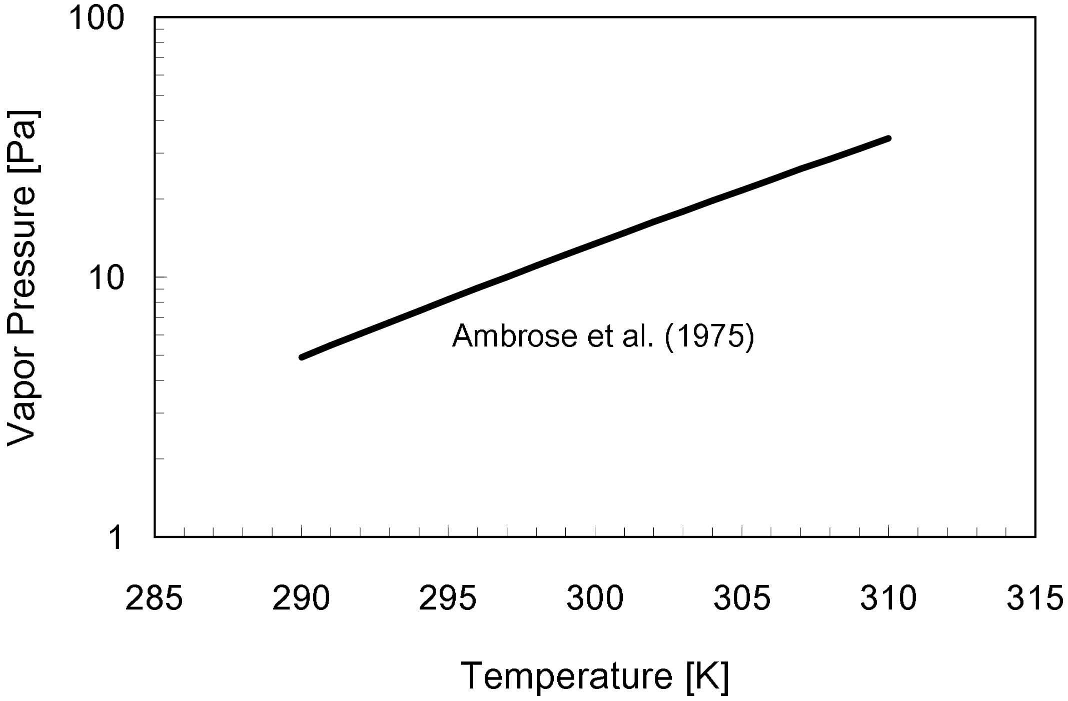

Fig. 8. Vapor pressure correlation by Ambrose et al., 1975 [30].

because there was no naphthalene vapor in the air passing through the holes in the upstream blockage. The local bulk vapor density, $\rho_{v,b}$ in [kg/m^3], in Eq. 3.2 for determining the local mass transfer coefficient at a point on the naphthalene surface is the rate of total mass transfer from the naphthalene surface upstream of the point divided by the air volumetric flow rate.

The average and local Sherwood numbers were defined, respectively, as

$$\overline{Sh} = \frac{\bar{h}_m D_h}{\sigma} \tag{3.6}$$

$$Sh = \frac{h_m D_h}{\sigma} \tag{3.7}$$

where σ is the mass diffusion coefficient for naphthalene vapor in the air in [m^2/s]. A correlation suggested by Goldstein and Cho [31] was used to determine the mass diffusion coefficient.

$$\sigma = 0.0681 \left(\frac{T}{298.16}\right)^{1.93} \left(\frac{1.013 \times 10^5}{p}\right) \times 10^{-4} \tag{3.8}$$

Figure 9 displays mass diffusion coefficient correlation by Goldstein and Cho [31]. According to the analogy between heat transfer and mass transfer described in Eckert [32],

$$\frac{\overline{Nu}}{Nu_0} = \frac{\overline{Sh}}{Sh_0} \tag{3.9}$$

$$\frac{Nu}{Nu_0} = \frac{Sh}{Sh_0} \tag{3.10}$$

where the reference Nusselt number and Sherwood number were based on the Dittus-Boelter correlation that is for a fully developed turbulent flow at the same Reynolds

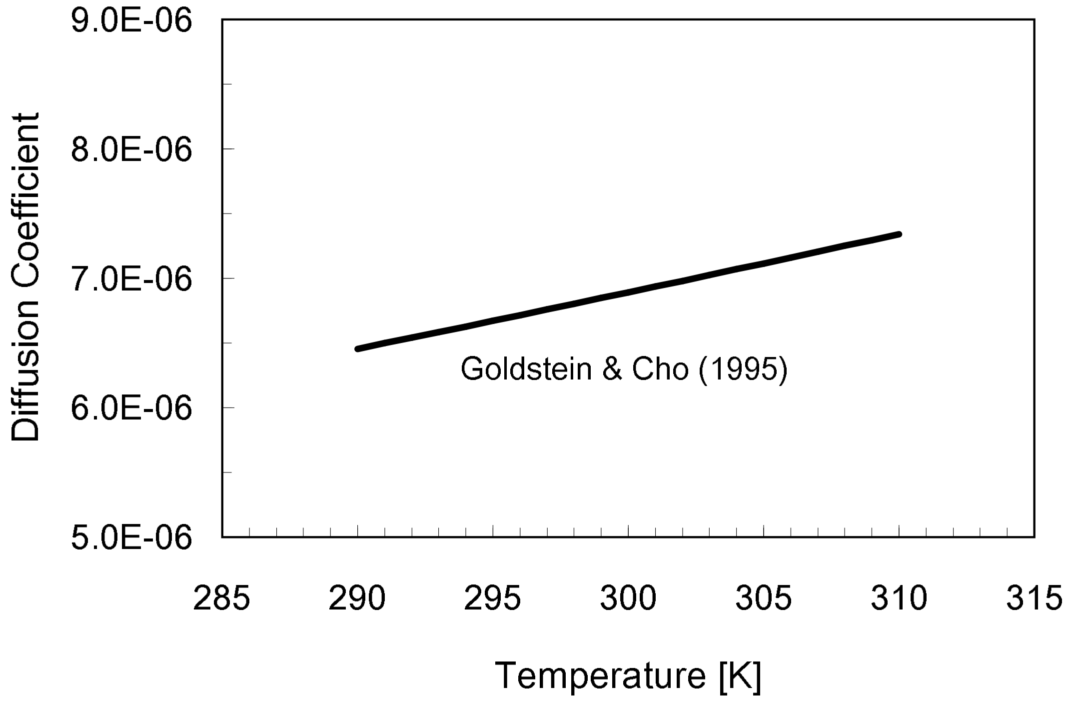

Fig. 9. Mass difussion coefficient correlation by Goldstein and Cho., 1995 [31].

number through a smooth channel with the same hydraulic diameter as the test channel.

$$Nu_0 = 0.023Re^{0.8}Pr^{0.4} \tag{3.11}$$

$$Sh_0 = 0.023Re^{0.8}Sc^{0.4} \tag{3.12}$$

where Pr is the Prandtl number and Sc is the Schmidt number determined by

$$Sc = 2.28\left(\frac{T}{298.16}\right)^{-0.1526} \tag{3.13}$$

The Reynolds number for the air flow through the test channel was also defined based on the hydraulic diameter of the test channel, and might be written as

$$Re = \frac{4\dot{m}}{\mu P_w} = \frac{2\dot{m}}{\mu(W+H)} \tag{3.14}$$

where $\dot{m}$ is the mass flow rate of air in [kg/s], μ is the dynamic viscosity of air in [N/m$^2 \cdot$ s], P_w is the wetted perimeter of the test section in [m], and W and H are the width and the height of the test section in [m], respectively.

2. Heat Transfer Measurement

The average Nusselt number for each of the three wall segments between two blockages was defined as

$$\overline{Nu} = \frac{\bar{h}D_h}{k} \tag{3.15}$$

where the average heat transfer coefficient was evaluated as

$$\bar{h} = \frac{IV - q_{loss}}{A_s(\overline{T}_w - \overline{T}_m)} \tag{3.16}$$

Based on the pressure gradient across the blockages, the friction factor was determined as

$$f = \frac{(\Delta p/\Delta x)D_h}{\rho \bar{u}^2/2} = 2\rho\left(\frac{\Delta p}{\Delta x}\right) D_h \left(\frac{A_c}{\dot{m}}\right)^2 \tag{3.17}$$

where Δx is the distance between pressure taps for measuring the pressure drops across two consecutive blockages in [m], $\bar{u}$ is the average air velocity in [m/s], and A_c is the cross-section area of the test channel in [m^2]. The friction factor was compared with a reference friction factor that is for fully developed turbulent flow in the channel with smooth walls.

$$f_0 = [0.79ln(Re) - 1.64]^{-2} \tag{3.18}$$

The average Nusselt number and friction factor were normalized, respectively, with the Nusselt number and friction factor for fully developed turbulent flow through a smooth channel at the same Reynolds number, given by

$$Nu_0 = 0.023Re^{0.8}Pr^{0.4} \tag{3.19}$$

The thermal performance was defined as

$$TP = (\overline{Nu}/Nu_0)(f/f_0)^{-1/3} \tag{3.20}$$

This parameter compares the heat transfer enhancement by the blockages per unit pumping power relative to the heat transfer for fully developed turbulent flow through a smooth channel.

D. Uncertainty Analysis

1. Mass Transfer Measurement

The calculations of the uncertainty values of the Reynolds number, the Sherwood number, and the friction factor were based on a confidence level of 95%, uncertainty values of ±1.0% for all properties of the air, and ±0.5% for all physical dimensions [33]. Based on the maximum uncertainties for pressure at the orifice flow meter, the pressure drop across the orifice, and the Reynolds number for flow through the orifice flow meter of ±2.0%, ±3.9%, and ±2.4%, respectively, the maximum uncertainty of the air mass flow rate was calculated to be ±2.2%. The corresponding maximum uncertainty of the Reynolds number was ±2.5%.

Based on the uncertainty values of ±6.3% for ΔM_n, ±4.3% for $\rho_{v,w}$, and ±6.5% for $\rho_{v,b}$, the maximum uncertainty of the average mass transfer coefficient was found to be 7.9%. Similarly, using uncertainty value of ±1.0% for ρ_s, ±9.5% for Δz , ±0.1% for Δt , the maximum uncertainty of the local mass transfer coefficient was calculated to be ±10.4%. With the uncertainty value of ±2.0% for the diffusion coefficient of naphthalene vapor in air using the equation suggested by Goldstein and Cho [31], the estimated values of the maximum uncertainties for the average and local Sherwood numbers were ±8.2% and ±10.6%, respectively.

2. Heat Transfer Measurement

The uncertainties of the Reynolds number, Nusselt number, and friction factor were estimated based on the uncertainty analysis method of [33] and a confidence level of 95%. With the uncertainties of ±1.0% for all properties of the air and ±0.5% for all physical dimensions, the uncertainty of the mass flow rate was calculated to be ±2.2%, and the uncertainty of the Reynolds number was estimated to be ±2.5%.

The uncertainties for the heater voltage and current were found to be ±2.2% and ±1.2%, and those for the average wall and bulk temperatures, ±2.5% and ±2.6%, respectively. With these values, the uncertainty of the Nusselt number was calculated to be ±6.1%.

Using the maximum uncertainty values of ±6.8% for Δp and ±2.2% for $\dot{m}$, the maximum value of the uncertainty of the friction factor was estimated to be ±8.4%.

CHAPTER IV

SINGLE-PHASE FORCED CONVECTION WITH BLOCKAGES: EXPERIMENTAL RESULTS

A. Mass Transfer Measurement

According to the heat/mass transfer analogy [32], local and average heat transfer coefficients, and heat transfer enhancement, are related to, respectively, local and average mass transfer coefficients, and mass transfer enhancement, by $Nu/Nu_0 = Sh/Sh_0$ and $\overline{Nu}/Nu_0 = \overline{Sh}/Sh_0$ [Eqs. 3.9 and 3.10]. In this section, we will present local and average mass transfer results in terms of Sh/Sh_0 and $\overline{Sh}/Sh_0$, respectively, and it is understood that we may apply the presentation and discussion of these results to heat transfer, and replace Nu/Nu_0 and $\overline{Nu}/Nu_0$ by and throughout.

1. Local Mass Transfer

In this study, the local mass transfer coefficient distributions on one of the two primary channel walls between two consecutive blockages were determined by measuring the changes of the elevations at a regular grid of 960 points (20×48) on the naphthalene surface of one of two cassettes during an experiment. Recall that the two naphthalene cassettes were installed side by side in a slot in the top channel wall between two blockages, exposing a smooth, flat, naphthalene surface to the air flow during an experiment. Local mass transfer results were obtained for eight different hole configurations, with aspect ratios between 1.0 and 3.4, and for two Reynolds numbers of 7,000 and 17,000.

We will first discuss the variations of the local Sh/Sh_0 distribution downstream of the first, second, and third blockages, in the two cases of round holes and elongated holes with the largest aspect ratio of 3.4. We will then present the local Sh/Sh_0 distributions downstream of the second blockage only and examine the effect of the configuration of the holes on the local Sh/Sh_0 distribution. In subsequent sections, we will present the results on the effects of the hole configuration on the average mass transfer.

a. Variation of Sh/Sh_0 Downstream of Three Consecutive Blockages

In Figs. 10 and 11, the local Sh/Sh_0 distributions downstream of the blockages are presented for the case of the smaller round holes (Case S-1) and in the case of the smaller elongated holes with the largest aspect ratio of 3.4 (Case S-4), respectively. In these figures, arrows indicate the direction of the main flow, which is from left to right, and the un-shaded portions of the four blockages indicate the locations of the staggered holes. Also, only half of each of the Sh/Sh_0 distributions is shown - a broken line shows a symmetry plane.

In the case of the round holes (Case S-1, Fig. 10), there is a monotonic increase of the Sh/Sh_0 value from less than 5.0 to over 12.0 between two blockages along the main flow direction. The local mass transfer is quite low immediately downstream of a blockage, but is very high immediately upstream of a blockage. The spanwise variation of Sh/Sh_0 is much smaller than the streamwise variation. Immediately upstream of a blockage, the Sh/Sh_0 value is slightly lower at a hole than between two adjacent holes. The Sh/Sh_0 distributions on the three segments of the channel wall are quite similar, with Sh/Sh_0 values of 5.0 or less over 40 to 50 percent of each wall segment, and values of over 12 over only small discrete regions upstream of a blockage between two holes. Comparing Fig. 10(a) and Fig. 10(b), it appears that the blockages cause slightly higher Sh/Sh_0 distributions when $Re = 7,000$ than when $Re = 17,000$.

After the air flows through the round holes in a blockage, a large portion of the jet impinges onto the upstream face of the downstream blockage, because the holes in consecutive blockages are staggered. There does not appear to be any reattachment of the air jets. The air is then deflected toward the two primary channel walls, causing the very high local mass transfer immediately upstream of the downstream blockage. The deflected airflow toward each channel wall may turn tangential to the wall before it is lifted from the wall and is forced to flow through the holes along the downstream blockage. A portion of the deflected airflow may turn upstream along the wall and is drawn into the recirculation zones with relatively slow moving flow between the air jets passing through the holes in the upstream blockage and the wall. The individual jets of air cause a periodic spanwise variation of the local mass transfer over each wall segment between consecutive blockages, although the spanwise variation is small compared with the streamwise variation between the blockages.

In the case of the elongated holes with an aspect ratio of 3.4 (Case S-4, Fig. 11), the spanwise variation of Sh/Sh_0 is quite large, although it is not as large as the streamwise variation. The local mass transfer is still very high immediately upstream of a blockage, with Sh/Sh_0 values of over 12.0. However, the local mass transfer is also quite high in an isolated region downstream of a hole, with Sh/Sh_0 values of over 12.0, while the values may be as low as less than 5.0 downstream of a blockage between two holes. The Sh/Sh_0 distribution downstream of the first blockage is slightly different than the similar distributions downstream of the second and third blockage. Comparing Fig. 11(a) and Fig. 11(b), while corresponding Sh/Sh_0 distributions are similar, the blockages with the elongated holes again cause slightly higher Sh/Sh_0 distributions when $Re = 7,000$ than when $Re = 17,000$.

After the air flows through the wide opening of an elongated hole in a blockage, a portion of the flow impinges onto the upstream face of the downstream blockage between two staggered holes. The deflected airflow toward each channel wall again causes the high mass transfer immediately upstream of the downstream blockage between two holes. The local mass transfer distributions in Fig. 11 show that there is reattachment of the air jet on the channel wall, causing the isolated region of high mass transfer downstream of the hole. Also, the low mass transfer region that is sandwiched between two regions of even lower mass transfer regions (with Sh/Sh_0 values below 5.0), downstream of a blockage, may indicate the existence of two counter-rotating vortices downstream of the blockage between two holes. The differences between the mass transfer distribution on the first wall segment and the similar mass transfer distributions on the two downstream wall segments may be the results of the airflow approaching the first blockage from an open wide channel while the airflow leaves an upstream blockage as individual jets before it approaches the second and third blockages. The effect of the entrance on the mass transfer distribution is more evident in Fig. 11 for Case S-4 with elongated holes than in Fig. 10 for Case S-1 with round holes.

In Figs. 12 and 13, the local Sh/Sh_0 distributions are presented for the cases of the larger round holes (Case L-1) and the larger holes with the largest aspect ratio of 3.4 (Case L-4), respectively. The Sh/Sh_0 distributions in Fig. 12 are similar to those in Fig. 10, except that the Sh/Sh_0 values are higher immediately downstream of the larger holes, resulting in larger periodic spanwise variations of the Sh/Sh_0 distributions in Case L-1 for the larger holes than in Case S-1 for the smaller holes. In Fig. 12(a), for $Re = 7,000$, distinctive local high mass transfer regions upstream of a blockage indicate that there may be flow reattachment of the air jets from the holes along an upstream blockage. The Sh/Sh_0 values in these reattachment regions, however, are much smaller than those in the very high mass transfer region immediately upstream of a blockage resulting from the deflection of the jets off the upstream face of the blockage. Flow reattachment downstream of the large round holes is not as evident for $Re = 17,000$. These results are consistent with those for round holes obtained in an earlier study in [2].

In the case of the larger holes with the largest aspect ratio of 3.4 (Case L-4), there are only two holes along each blockage and there is a rather wide section of the blockage between two holes that does not allow the flow to pass. Figure 13 shows that the Sh/Sh_0 values are large downstream of the holes, where flow reattachment is clearly evident, and in a wide region upstream of a blockage between two holes, where the flow is deflected toward the channel wall. However, there are large regions of very low Sh/Sh_0 values downstream of the blockage between two holes and between a hole and the channel sidewall. Because of the geometry of the blockages in Case L-4, with two large "slots" separated from each other and from the sidewalls by very wide sections of the blockage, the spanwise variation of Sh/Sh_0 may be larger than the streamwise variation, and the Sh/Sh_0 distributions are different on the three wall segments between consecutive blockages. Figure 13 also shows that the Sh/Sh_0 distribution is the lowest on the first wall segment and the highest on the third and last wall segment.

Comparing the Sh/Sh_0 distributions in Fig. 12(a) and Fig. 12(b), and those in Fig. 13(a) and Fig. 13(b), it can be seen that the blockages with the larger holes also cause slightly higher mass transfer enhancement at a lower air flow rate.

b. Effect of Hole Configuration on Sh/Sh_0 Distribution Downstream of Second Blockage

To examine the effect of the hole aspect ratio on the local mass transfer distributions downstream of blockages with holes, the Sh/Sh_0 distributions on the second wall segment, between the second and third blockages, for the four cases with the smaller

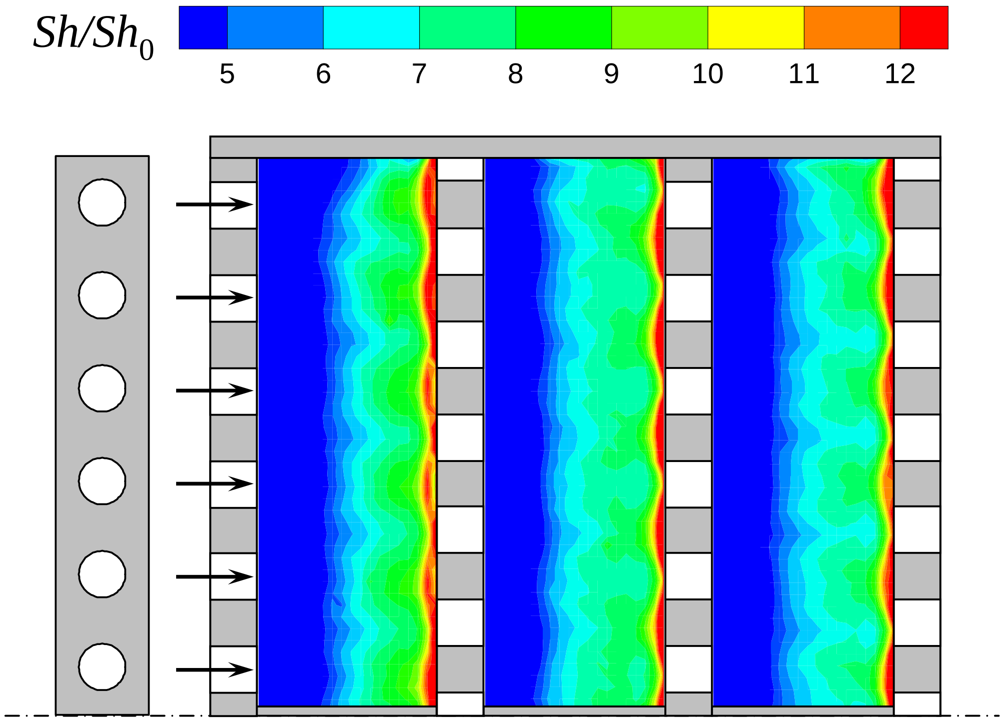

(a) *Re* = 7,000

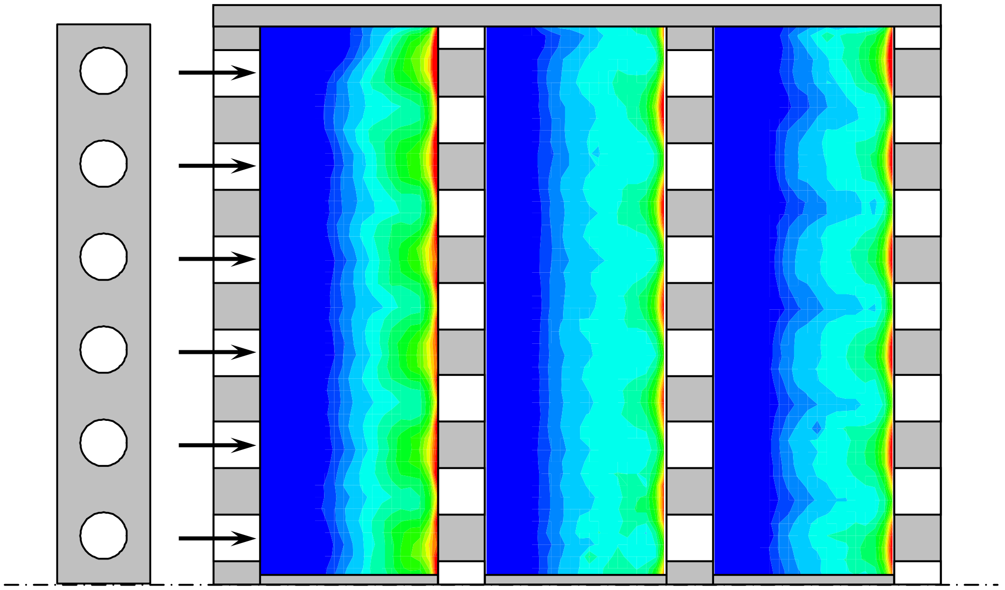

(b) *Re* = 17,000

Fig. 10. Local mass transfer distributions on three wall segments downstream of blockages with the smaller round holes, Case S-1.

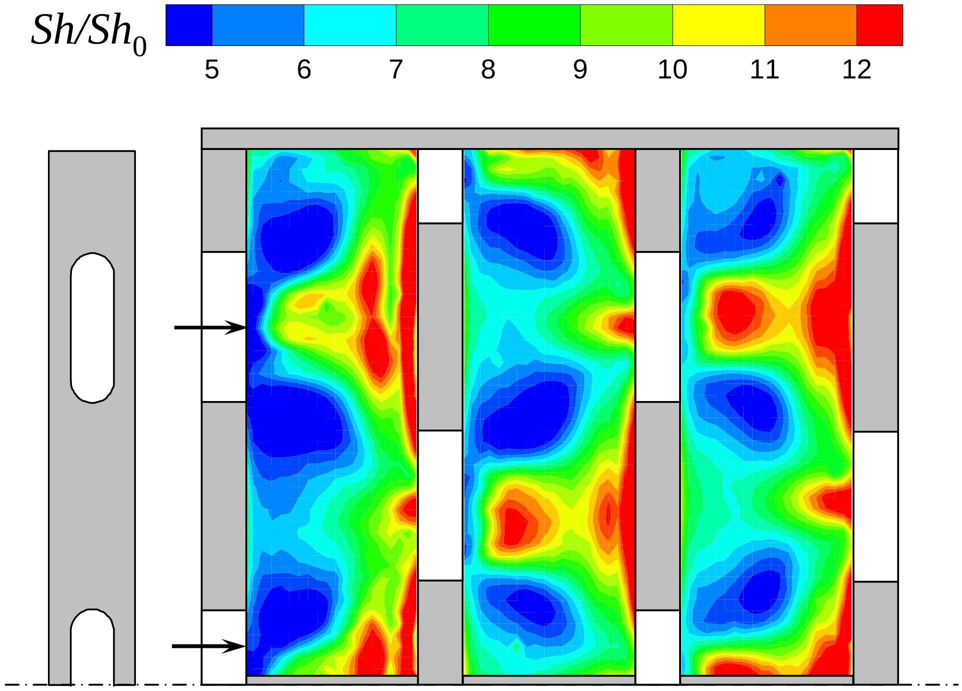

(a) *Re* = 7,000

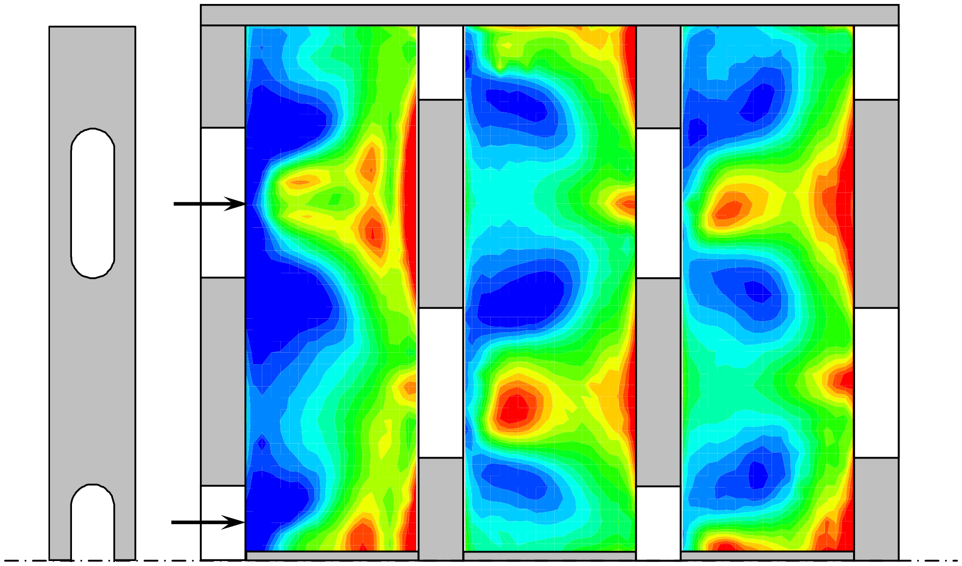

(b) *Re* = 17,000

Fig. 11. Local mass transfer distributions on three wall segments downstream of blockages with the smaller elongated holes, Case S-4.

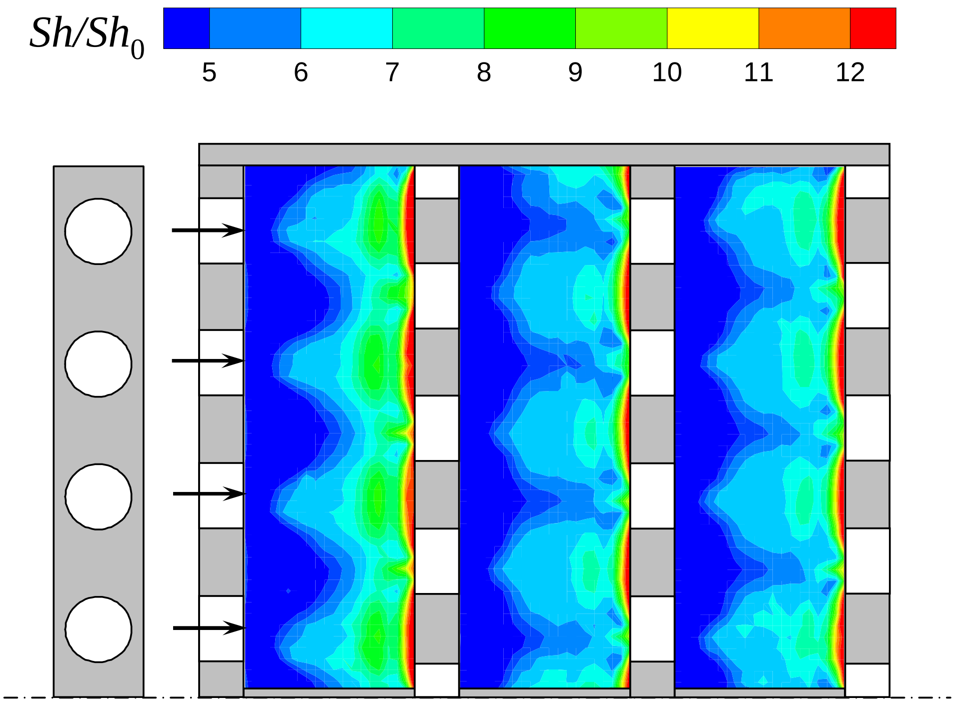

(a) *Re* = 7,000

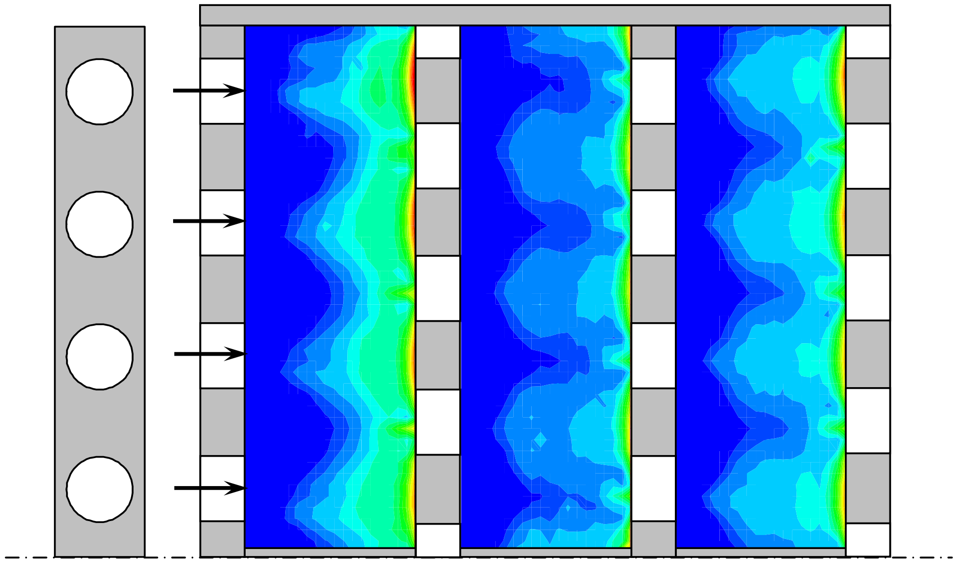

(b) *Re* = 17,000

Fig. 12. Local mass transfer distributions on three wall segments downstream of blockages with the larger round holes, Case L-1.

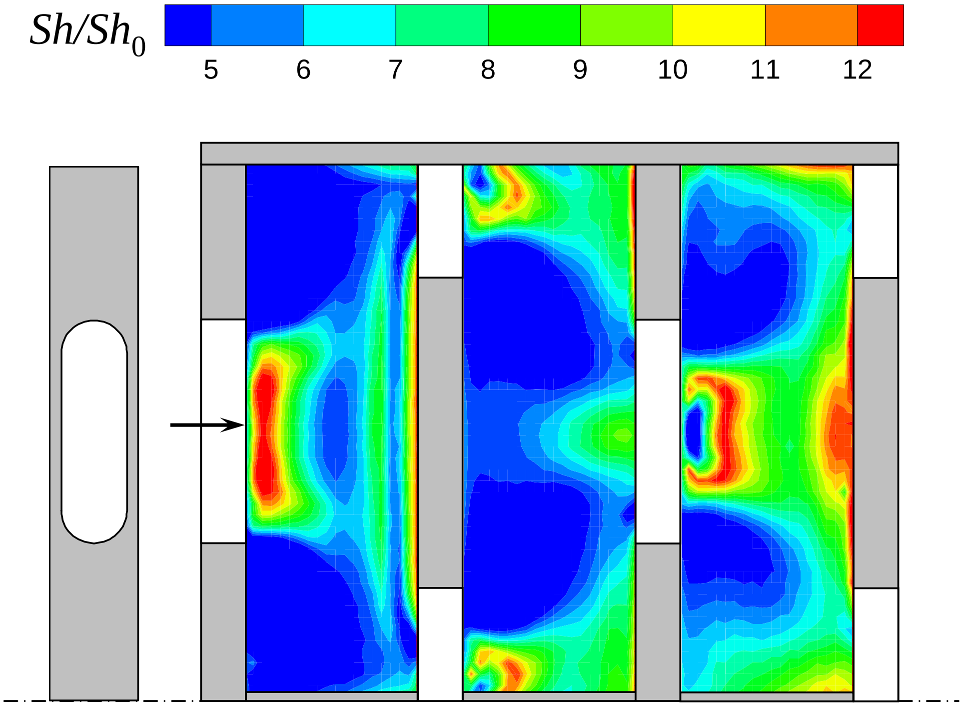

(a) Re = 7,000

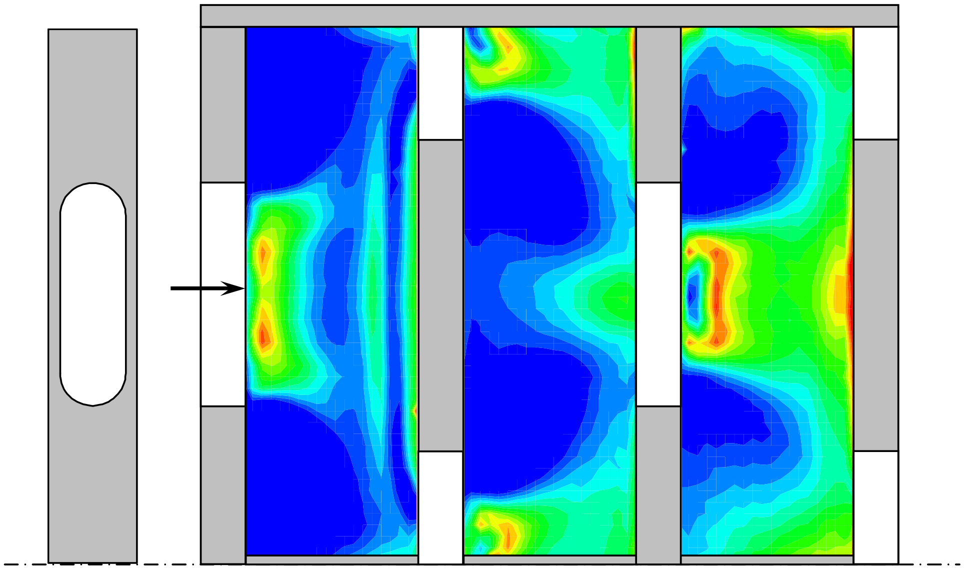

(b) Re = 17,000

Fig. 13. Local mass transfer distributions on three wall segments downstream of blockages with the larger elongated holes, Case L-4.

holes (Cases S-1, S-2, S-3, and S-4) are presented in Figs. 14 and 15, for $Re = 7,000$ and 17,000, respectively. In the case of the round holes, Figs. 14(a) and 15(a) again show that the monotonic variation of Sh/Sh_0 in the main flow direction is much larger than the spanwise Sh/Sh_0 variation. It can be seen from Figs. 14 and 15 that, increasing the hole aspect ratio increases the spanwise Sh/Sh_0 variation. Increasing the hole aspect ratio appears to increase the overall mass transfer on the wall segment, since there are larger regions of higher mass transfer in the larger hole aspect ratio cases. In Cases S-3 and S-4, there are regions with relatively high mass transfer downstream of the holes in the second blockage. There are also regions with clearly very high mass transfer upstream of the third blockage between two holes, and the size of these regions increases with increasing hole aspect ratio.

The Sh/Sh_0 distributions on the second wall segment for the four cases with the larger holes (Cases L-1 through L-4) are presented in Figs. 16 and 17, for $Re = 7,000$ and 17,000, respectively. To maintain the same total hole-to-blockage area ratio of 0.3 in these four cases, doubling the area of a round hole reduces the number of holes from eight in Case L-1 to four in Case L-2. In Case L-3, for the holes with an aspect ratio of 2.6, there are only three holes in each blockage, while in Case L-4, for the holes with an aspect ratio of 3.4, there are only two holes in a blockage. These large elongated holes, or slots, are spaced rather far apart along the blockages. Figures 16 and 17 show that the mass transfer is very low downstream of the wide sections of the upstream blockage between holes, and the size of the low Sh/Sh_0 regions increases with an increase of the distance separating the holes. As a result, for the three cases with large elongated holes, the mass transfer distribution appears to be lower when the distance separating the holes is larger. It will be shown in the next section that the average mass transfer is lower in Case L-3 than in Case L-2, and is lower in Case L-4 than in Case L-3.

The flow reattaches on the channel wall downstream of the large elongated holes in Cases L-2, L-3, and L-4. The spanwise Sh/Sh_0 variation is larger in these three cases than in Case L-1 for the round holes, as a result of the large Sh/Sh_0 values in the regions of flow reattachment downstream of the elongated holes and upstream of the downstream blockage where the flow is deflected toward the channel wall, and the very low Sh/Sh_0 values downstream of the upstream blockage between the holes.

Comparing Figs. 14 and 15, and Figs. 16 and 17, corresponding Sh/Sh_0 distributions for the same hole aspect ratio are very similar, and the Sh/Sh_0 distributions are higher when $Re = 7,000$ than when $Re = 17,000$. Thus, increasing the air flow rate does not significantly change the local mass transfer distribution downstream of a blockage with holes, but it decreases the overall mass transfer enhancement.

Based on the local mass transfer results presented in Figs. 14 through 17, the smaller elongated holes with the largest aspect ratio of 3.4 in Case S-4 appear to enhance the mass transfer the most. The mass transfer may be enhanced further by increasing the number of these holes in the blockages, since the mass transfer is quite high downstream of the holes and decreasing the spacing between two holes also reduces the size of the low mass transfer regions downstream of the blockages between two holes. Also, increasing the number of holes, which increases the hole-to-blockage area ratio, should reduce the pressure drop across the blockages.

2. Average Mass Transfer

The average mass transfer on a wall segment was obtained both by weighing the two naphthalene cassettes, located side by side in a slot in the top channel wall between two blockages, before and after each experiment, and by determining the area-weighted average of the 960 local Sh/Sh_0 values, on the naphthalene surface of one of the two cassettes, that were measured in a separate experiment. For all of the

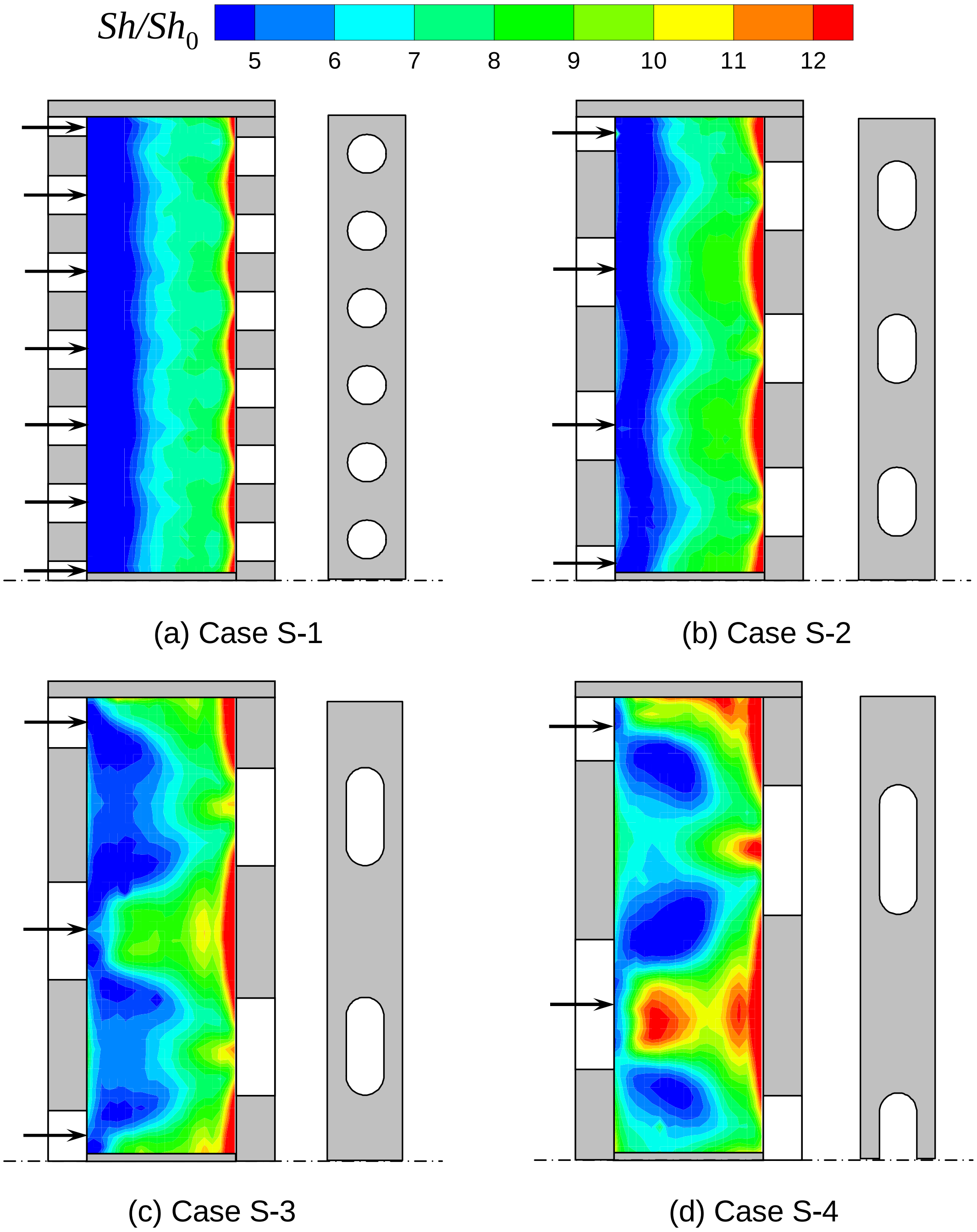

(a) Case S-1

(b) Case S-2

(c) Case S-3

(d) Case S-4

Fig. 14. Local mass transfer distributions on second wall segment downstream of second blockage with the smaller holes, Cases S-1 through S-4, for *Re*=7,000.

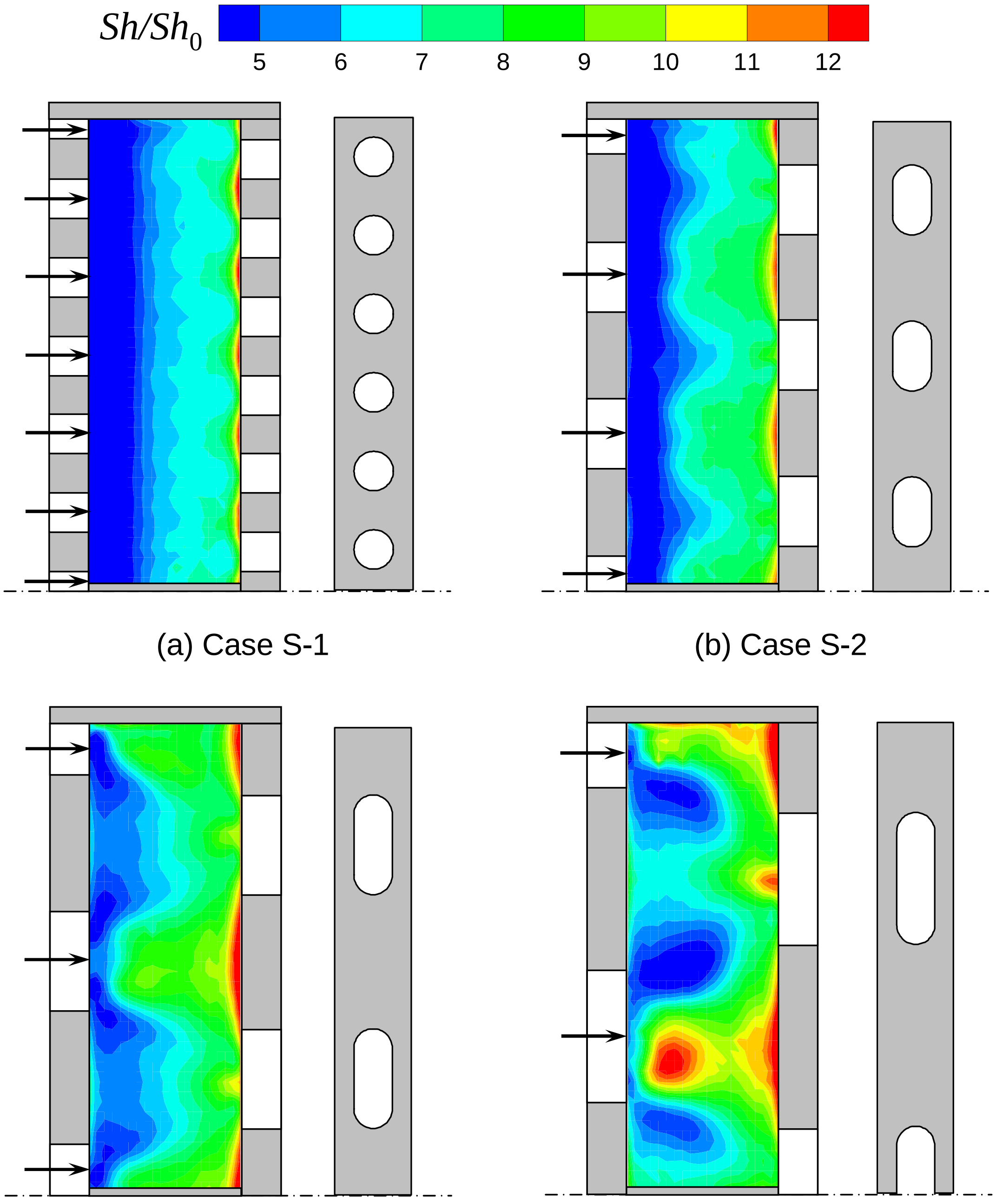

(a) Case S-1

(b) Case S-2

(c) Case S-3

(d) Case S-4

Fig. 15. Local mass transfer distributions on second wall segment downstream of second blockage with the smaller holes, Cases S-1 through S-4, for Re=17,000.

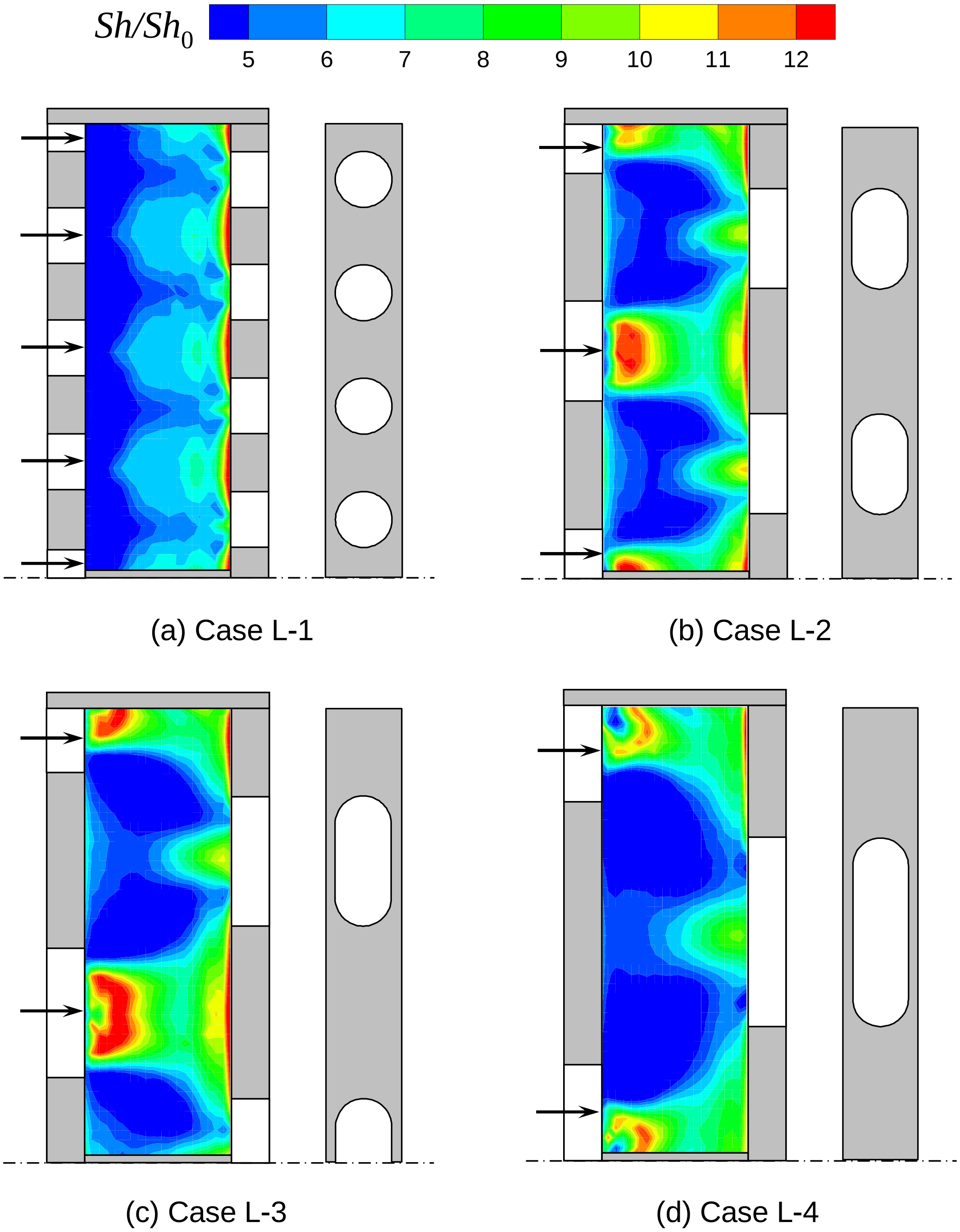

(a) Case L-1

(b) Case L-2

(c) Case L-3

(d) Case L-4

Fig. 16. Local mass transfer distributions on second wall segment downstream of second blockage with the larger holes, Cases L-1 through L-4, for Re=7,000.

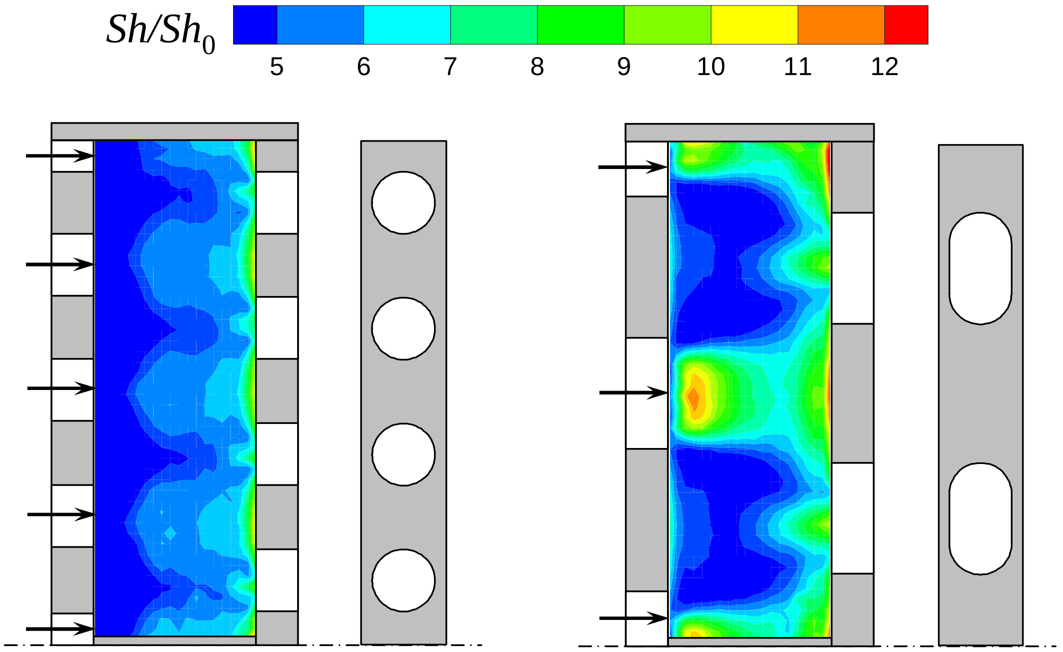

(a) Case L-1

(b) Case L-2

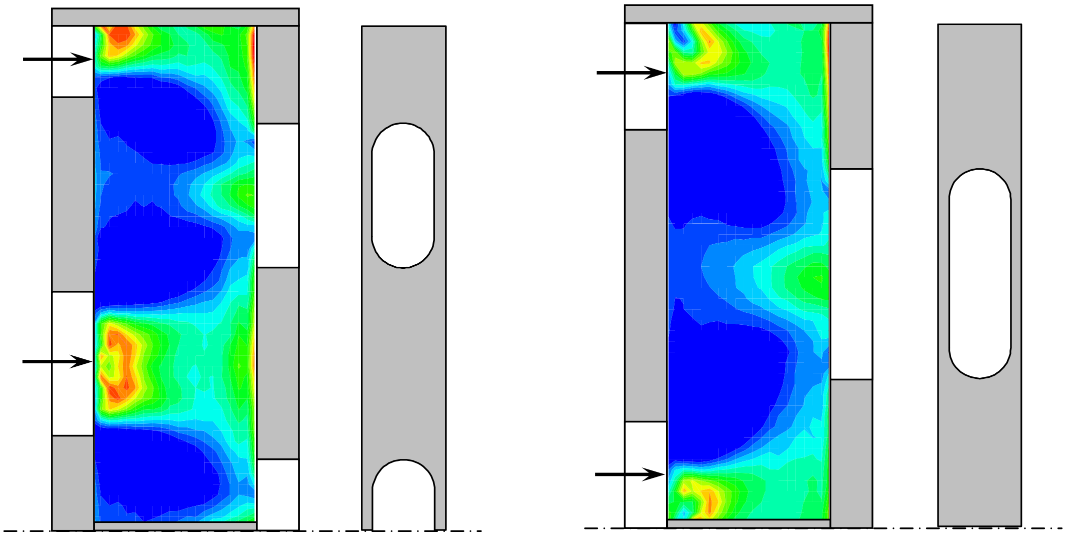

(c) Case L-3

(d) Case L-4

Fig. 17. Local mass transfer distributions on second wall segment downstream of second blockage with the larger holes, Cases L-1 through L-4, for Re=17,000.

experiments, the $\overline{Sh}/Sh_0$ values obtained by weighing the two cassettes differed by less than 2.1% (the average of the variations was 0.4%, with a standard deviation of 1.1%), while the $\overline{Sh}/Sh_0$ values obtained by weighing the cassettes and by averaging the local Sh/Sh_0 values differed by no more than 4.9% (the average of the variations was 1.9% and the standard deviation was 2.2%). These variations were well within the estimated uncertainty value of 8.2% for $\overline{Sh}/Sh_0$.

Supplementary heat transfer experiments were conducted to obtain the average heat transfer coefficients on three wall segments downstream of the same blockages in this study, using the test section of this study, three copper blocks as the wall segments between blockages, three flexible electric heaters to supply heat to the copper blocks, and small-gage thermocouples (seven in each copper block) to measure the wall and air temperatures, for the same two air flow rates. The effect of the hole configuration on $\overline{Nu}/Nu_0$ based on the heat transfer measurements was found to be consistent with the effect on $\overline{Sh}/Sh_0$ in this study. The $\overline{Nu}/Nu_0$ values in the heat transfer study were lower than corresponding $\overline{Sh}/Sh_0$ values in this study by no more than 9.9%. For all eight hole configurations studied, the heat transfer data were lower than the mass transfer data by 4.9% on average, with a standard deivation of 2.7%. The detailed experimental results will be discussed in the next section.

In Fig. 18, the average Sherwood number ratios on the three wall segments for Cases S-1, S-4, L-1, and L-4 are presented. These four cases are for round holes and elongated holes with the largest aspect ratio of 3.4. The corresponding local mass transfer distributions for these cases have already been given in Figs. 10 through 13 and discussed earlier. Based on the results presented in Fig. 18, the following trends can be observed:

1. In all cases, the average mass transfer enhancement is lower when the air flow

rate is higher. The $\overline{Sh}/Sh_0$ value is lower when $Re = 17,000$ than when $Re = 7,000$ - by 3.5 to 6.8%.

2. For the smaller holes, the average mass transfer is about the same on all three wall segments. In Case S-1, for the round holes, the $\overline{Sh}/Sh_0$ values on the three wall segments are within 1.1% of one another, with values of about 6.5 and 6.2, respectively, for $Re = 7,000$ and 17,000. In Case S-4, for the wide elongated holes, the $\overline{Sh}/Sh_0$ values on the two upstream wall segments are within 1.5% of each another, but are slightly higher by 2.1 to 4.5% on the third wall segment. The $\overline{Sh}/Sh_0$ values are 25 and 26% higher in Case S-4 than in Case S-1, for $Re = 7,000$ and 17,000, respectively.

3. For the larger round holes (Case L-1), the average mass transfer is the highest on the first wall segment and the lowest on the last wall segment, but the differences between the $\overline{Sh}/Sh_0$ values on the two wall segments are less than 5.6%. The $\overline{Sh}/Sh_0$ values of between 5.5 to 6.1 on the wall segments in this case (for the larger round holes) are lower than values of between 6.1 and 6.5 in Case S-1, for the smaller round holes.

4. In Case L-4, there are only two large elongated holes along each blockage and it has been shown that the Sh/Sh_0 distributions on the three wall segments were very different and that there were very large regions of low Sh/Sh_0 values in the distribution on the first wall segment. Figure 18 shows that the $\overline{Sh}/Sh_0$ values are small on the first wall segment, but are 14 to 15% larger on the second wall segment, and are the highest on the last wall segment, with values of about 36% over those on the first wall segment.

In Fig. 19, the average Sherwood number ratios on the second wall segment for

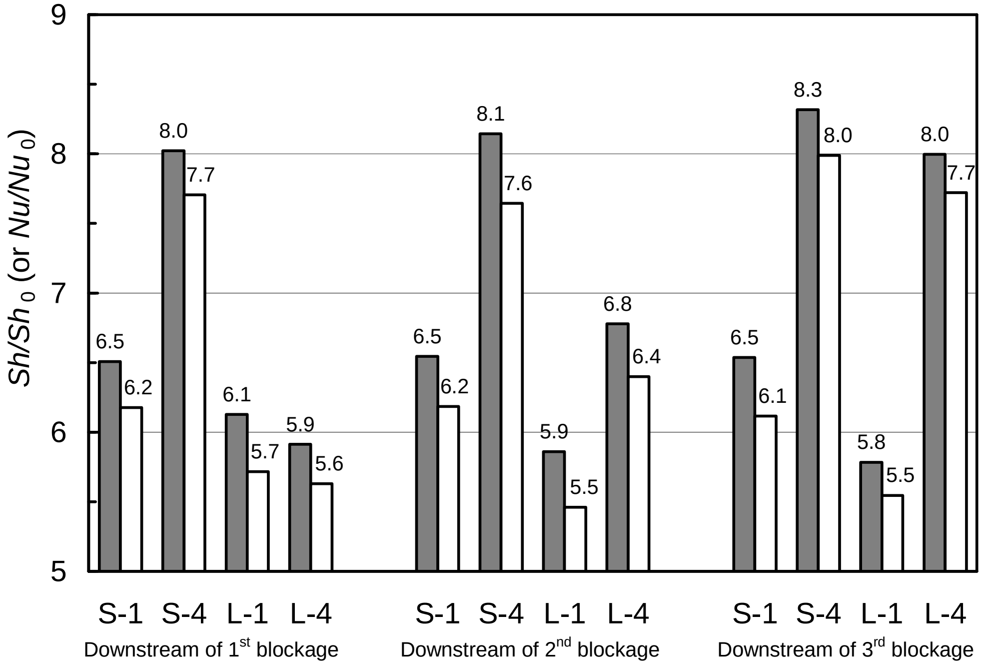

Fig. 18. Heat (mass) transfer enhancement on three wall segments between blockages with round holes and elongated holes with the largest aspect ratio.

all hole configurations are compared. The figure shows that the average mass transfer on the second wall segment is higher in the four cases for the smaller holes than in the corresponding cases for the larger holes. Again, in all cases, the $\overline{Sh}/Sh_0$ value is lower when $Re = 17,000$ than when $Re = 7,000$ - with a maximum difference of 6.8%. For the smaller holes, the average mass transfer increases as the aspect ratio of the holes is increased. The maximum $\overline{Sh}/Sh_0$ values for the widest holes (Case S-4) are about 24% higher than those for the round holes (Case S-1). The local Sh/Sh_0 distributions in Figs. 14 and 15 showed that there was significant mass transfer enhancement downstream of the wider holes, because of flow reattachment, and in regions upstream of the wide sections of the downstream blockage between staggered holes, as a result of the deflection of the flow from the downstream blockage toward the channel wall.

For the larger holes, the average mass transfer is again the lowest for the round holes (Case L-1), but is the highest for the elongated holes with an aspect ratio of 1.8 (Case L-2). With a further increase of the hole aspect ratio, the $\overline{Sh}/Sh_0$ value decreases. The increase of the size of the large low mass transfer regions downstream of the wide sections of a blockage between holes may contribute to the decrease of the average mass transfer with an increase of the aspect ratio of the larger holes (see Figs. 16 and 17).

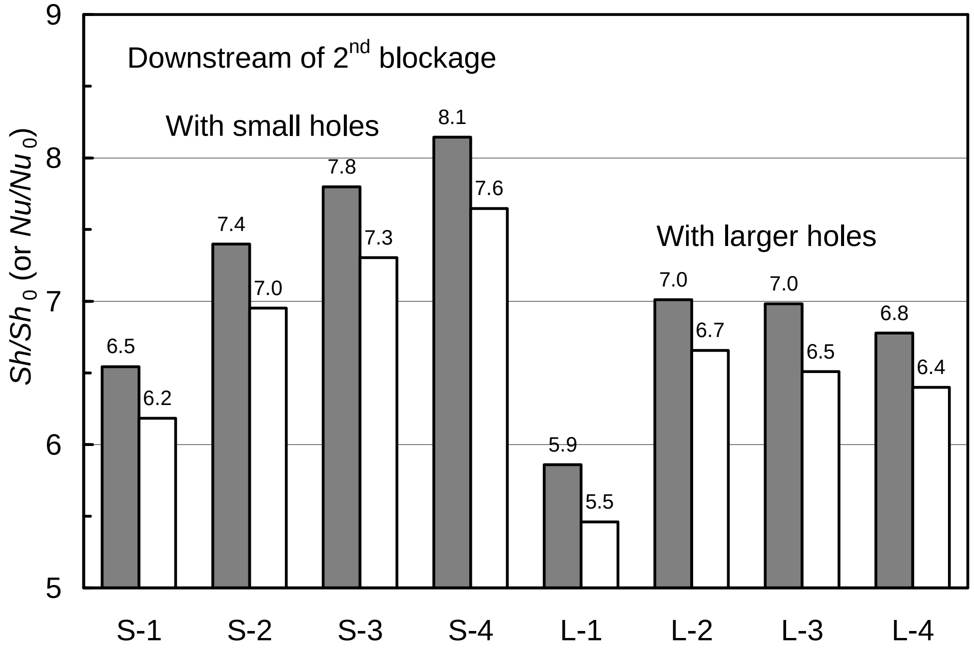

Fig. 19. Heat (mass) transfer enhancement on second wall segment between second and third blockages with round and elongated holes.

B. Heat Transfer Measurement

1. Heat Transfer on Wall Segments

In this study, average heat transfer coefficients were determined on three wall segments between blockages with holes in a wide rectangular channel. Eight different configurations of the holes in the blockages - two holes diameters and four hole aspect ratios - were examined. Experiments were conducted at three different air flow rates. The pressure drops across the blockages were also measured. The heat transfer and pressure drop results are presented in this section in terms of a Nusselt number ratio, $\overline{Nu}/Nu_0$, and a friction factor ratio, f/f_0. These two ratios give, respectively, the heat transfer enhancement by the blockages, and the increase in the pressure drop cause by the blockages.

Figure 20 shows the heat transfer enhancement on the three wall segments by the blockages with holes. In the figure, the $\overline{Nu}/Nu_0$ values for the three Reynolds numbers of about 7,000, 12,000, and 17,000 are presented for the eight cases with different hole configurations - (a) Cases S-1 through S-4 for the blockages with the smaller holes and (b) Cases L-1 through L-4 for the blockages with the larger holes. The results show that the $\overline{Nu}/Nu_0$ values ranging from 5.2 to 8.0. Thus, the heat transfer coefficients on the wall segments downstream of the blockages with holes are much higher than that for fully developed flows through an open channel without blockages at the same Reynolds numbers. The blockages with the smaller holes increase the heat transfer on the wall segments more than those with the larger holes. In all cases, the heat transfer enhancement is lower when the air flow rate is higher. Increasing the Reynolds number from about 7,000 to about 17,000 decreases the $\overline{Nu}/Nu_0$ value by 6.1%, on average, with a maximum change of -9.3%.

For the blockages with the smaller holes, Fig. 20(a) shows that increasing the aspect ratio of the holes from 1.0 to 3.4 increases the Nusselt number ratio monotonically. The $\overline{Nu}/Nu_0$ values for the blockages with the widest holes (Case S-4) are 27% to 34% larger than those for the blockages with the round holes (Case S-1). The $\overline{Nu}/Nu_0$ values are larger on the first wall segment between the first two blockages than on the two downstream wall segments.

For the blockages with the larger holes, Fig. 20(b) shows that the $\overline{Nu}/Nu_0$ values are smaller in Case L-1 for the blockages with the round holes than in Cases L-2 through L-4 for the blockages with elongated holes. In Case L-1, the $\overline{Nu}/Nu_0$ values are the largest on the first wall segment and the lowest on the third wall segments, while in Cases L-2 through L-4, the trend reverses. For the blockages with the elongated holes, with an increase of the aspect ratio of the holes, $\overline{Nu}/Nu_0$ decreases on the first wall segment, remains about constant on the second wall segment, and increases on the third wall segment, with a maximum change of less than 9.1%.

Figure 20 clearly shows the variations of the heat transfer coefficients on the three wall segments for the eight different configurations of the holes in the blockages in this study and that the flows through the blockages were not periodic during the experiments. In Fig. 21, the average heat transfer results over the three wall segments are presented. From these average results, it can be readily seen that the average heat transfer enhancement on the three wall segments decreases with increasing mass flow rate, and is larger in the cases of the blockage with the smaller holes. The average heat transfer enhancement increases monotonically with an increase of the aspect ratio of the smaller holes, and the $\overline{Nu}/Nu_0$ values are lower in the case of the larger round holes than similar values in the three cases with the larger elongated holes.

In the previous section, naphthalene sublimation experiments were conducted to obtain the average mass transfer and local mass transfer distributions on three wall segments downstream of the same blockages considered in this study, using the test section of this study, for $Re = 7,000$ and 17,000. By applying the heat and mass transfer analogy, the measured average and local Sherwood number ratios were converted to average and local Nusselt number ratios. The effects of the hole configuration and mass flow rate on $\overline{Nu}/Nu_0$ based on the mass transfer measurements in the previous section are found to be consistent with the effects on that are reported here. For all eight hole configurations considered, the $\overline{Nu}/Nu_0$ values based on the mass transfer experiments (with an estimated uncertainty of ±8.2%) are slightly higher (by 4.9% on average) than those in this study, with a maximum deviation of 9.9% and a standard deviation of 2.7%. In the previous section, the local heat (mass) transfer distributions helped explain the effect of the hole configuration on the average heat (mass) transfer on the wall segments downstream of the blockages with holes.

2. Friction Factor

The friction factors were calculated with Eq. 3.17 using the pressure drops across two consecutive blockages - between the pressure taps in the first and third rows, between the pressure taps in the second and fourth rows, and between those in third and fifth rows [see Fig. 7(b)]. As expected, because the blockages with the smaller and larger holes in this study block 80% and 70%, respectively, of the flow cross section of the rectangular channel, the pressure drops are much larger across the blockages than for airflows through an open channel at the same flow rates. Figure 22 shows that the blockages with the smaller holes in Cases S-1 through S-4 cause larger pressure drops than the blockages with the larger holes in Cases L-1 through L-4. The friction factor ratio, f/f_0, increases as the hole aspect ratio is increased, with values ranging from about 700 to about 1,900 for the blockages with the smaller holes, and from about 300 to about 1,300 for the blockages with the larger holes.

In all cases, f/f_0 is larger when the Reynolds number is increased. The f/f_0

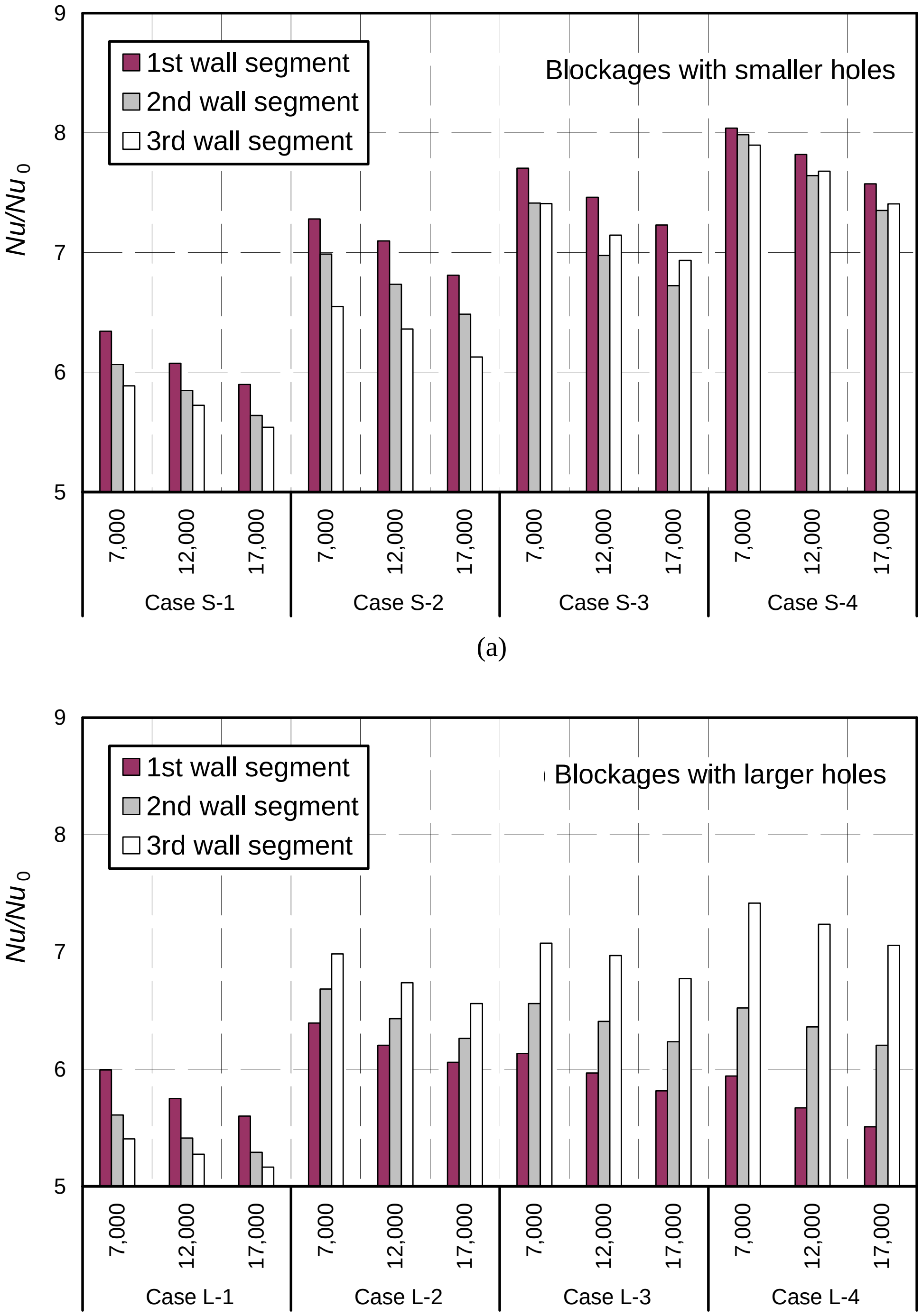

(a)

(b)

Fig. 20. Heat transfer enhancement on wall segments downstream of blockages.

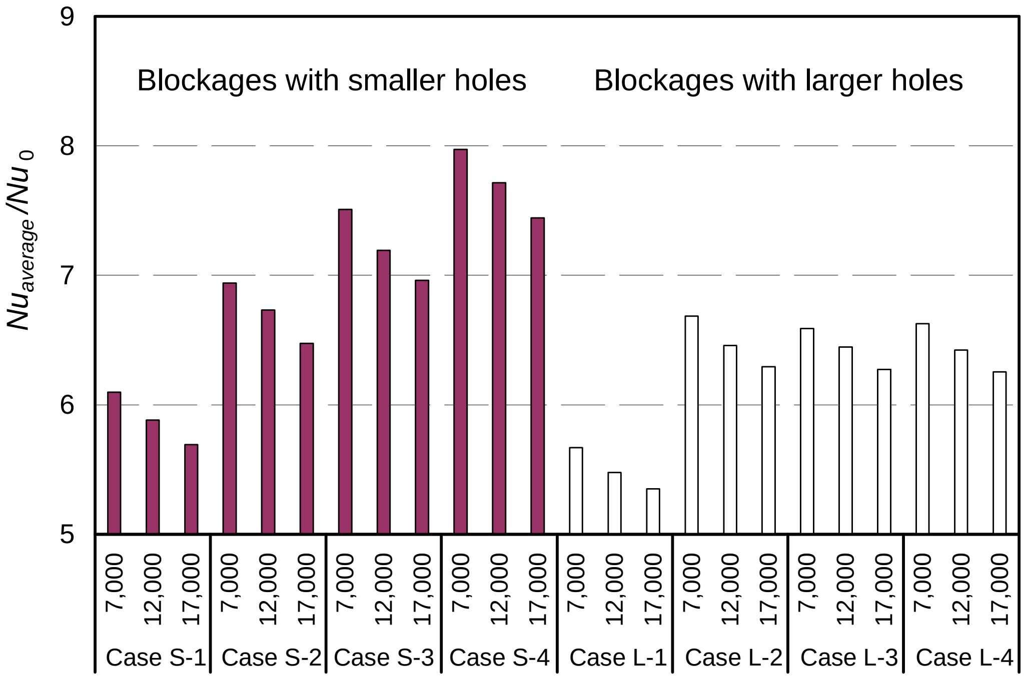

Fig. 21. Average heat transfer enhancement on wall segments downstream of blockages.

values for $Re = 12,000$ and $Re = 17,000$ are about 16% and 27%, respectively, higher than corresponding values for $Re = 7,000$. In almost all cases, f/f_0 is larger when the hole aspect ratio is larger. For the blockages with the smaller holes, increasing the aspect ratio of the holes from 1.0 to 3.4 increases the friction factor ratio by 55% to over 100%. For the blockages with the larger holes, increasing the aspect ratio of the holes from 1.0 to 3.4 may more than triple the f/f_0 values. The wider sections of the blockages between staggered holes with a larger aspect ratio appear to increase the resistance to the air flow through the channel more than the blockages that have holes with a smaller aspect ratio and a smaller spacing between holes.

There are variations of the f/f_0 values for the three wall segments. For the blockages with the round holes, the pressure drops are the largest across the first wall segment (that is, across the first two blockages) and the smallest across the last wall segment (that is, across the last two blockages). For the blockages with the widest elongated holes, the trend reverses. Evidently, the holes with various aspect ratios in the blockages affect differently the air flows from an open channel and those through the holes in one or two upstream blockages.

3. Thermal Performance

The thermal performance was evaluated with Eq. 3.20 using the average Nusselt number over the three wall segments and the average of the friction factors for the three wall segments. Although the smaller holes in the blockages effect more heat transfer than the larger holes in the blockages, they also cause a larger increase of the pressure drop across the blockages than the larger holes. While $\overline{Nu}/Nu_0$ decreases with increasing Re, f/f_0 increases. Figure 23 compares the thermal performances of the blockages with the smaller and the larger holes. In all cases, the TP value decreases with an increase of the Reynolds number. The blockages with the larger

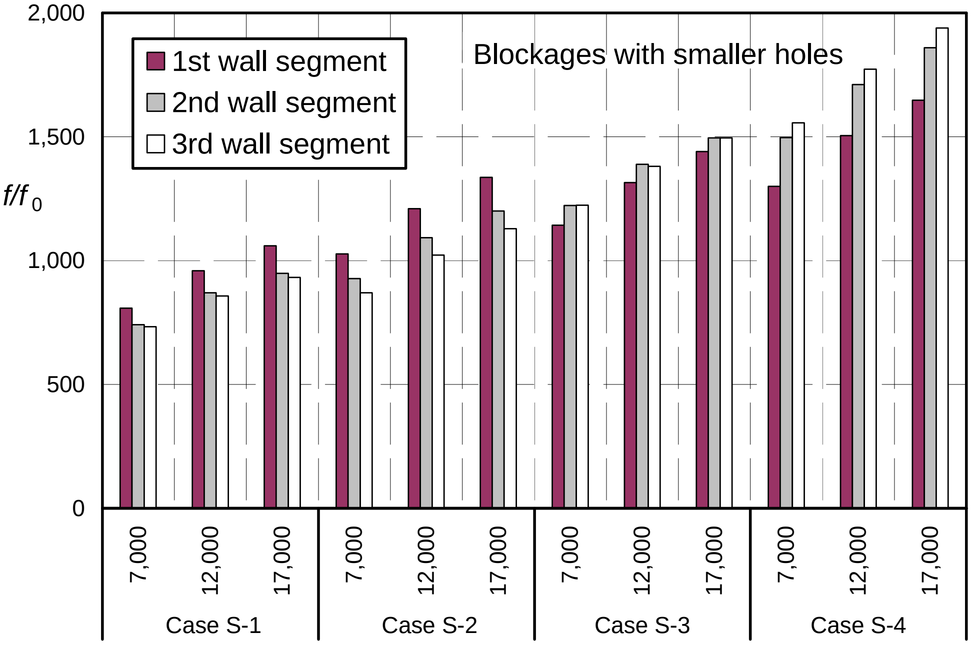

(a)

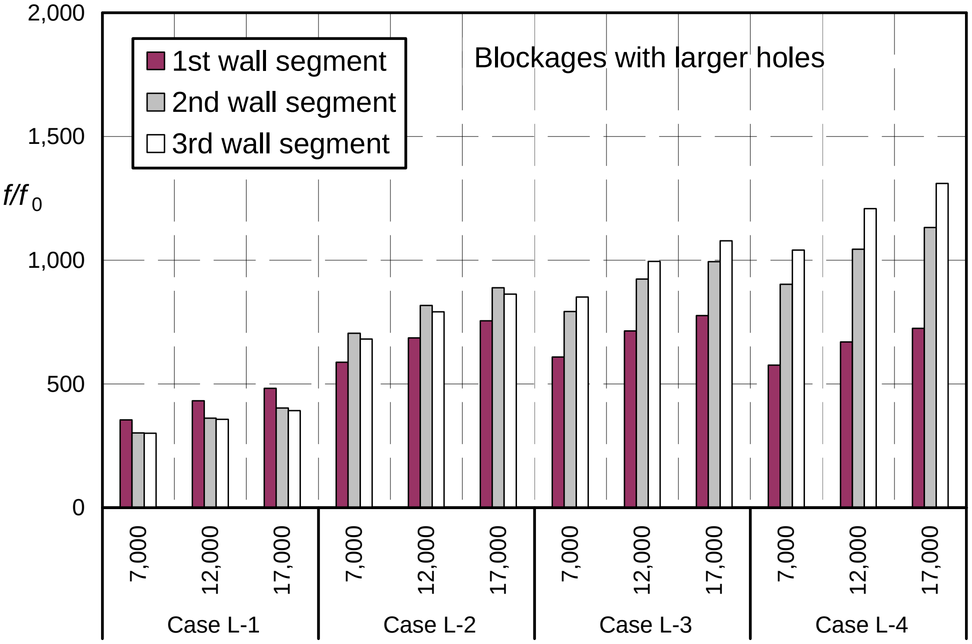

(b)

Fig. 22. Pressure drops across wall segments downstream of blockages relative to that for fully developed turbulent flow through a smooth channel without blockages.

holes outperform those with the smaller holes slightly, with TP values ranging from 0.62 to 0.83 versus values from 0.57 to 0.71. For the blockages with the smaller holes, the TP values for the three elongated hole cases are about the same (within 1% for the same Re) and are about 6% higher than those for the round hole cases. For the blockages with the larger holes, the thermal performance decreases with an increase of the hole aspect ratio while keep the total hole-to-blockage area ratio constant.

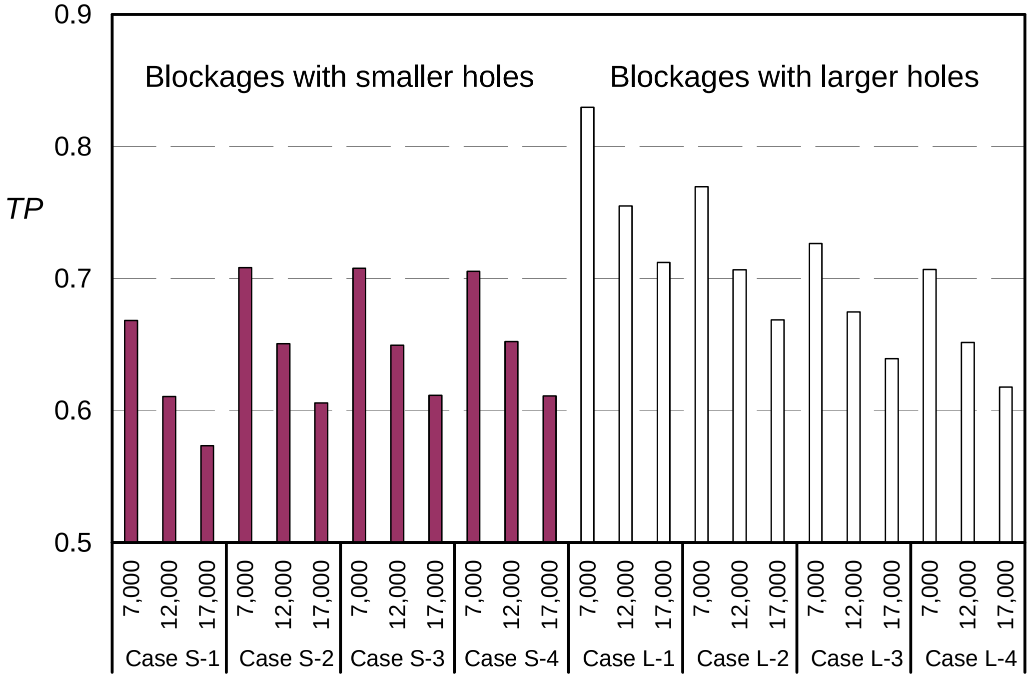

Fig. 23. Thermal performances of blockages with holes — heat transfer enhancement per unit pumping power relative to that for fully developed flow through a smooth channel.

CHAPTER V

SINGLE-PHASE FORCED CONVECTION WITH BLOCKAGES: SUMMARY

A. Mass Transfer Measurement

Naphthalene sublimation experiments were conducted to study heat (mass) transfer enhancement by blockages with round and elongated holes in a wide rectangular channel that modeled the cooling channel in the trailing edge region of an internally-cooled gas turbine blade. Local and average heat (mass) transfer results were obtained for eight configurations of staggered holes with two sizes and four aspect ratios in the blockages, and for two Reynolds numbers. For the conditions under which the experiments were conducted and the geometries of blockages and the test sections that were studied, the results are summarized as follows:

1. The distribution of the local heat (mass) transfer is very much dependent on the configuration of the holes in the blockages. For the blockages with round holes in this study, the heat (mass) transfer on the wall segment between two blockages is low downstream of the upstream blockage and is high upstream of the downstream blockage, with much larger streamwise variation than spanwise variation. For the blockages with elongated holes in this study, the heat (mass) transfer is high downstream of the holes, as a result of flow reattachment, but is very low downstream of the wide section of the blockage between holes, and the spanwise variation of the local heat (mass) transfer may be as large as the streamwise variation. The local heat (mass) transfer distribution is not significantly affected by changing the air flow rate.
2. Blockages with holes may cause the average heat (mass) transfer on the wall segments between two blockages in a channel to be much higher than that for

a fully developed flow through an open channel with no blockages at the same flow rate, but they also significantly increase the pressure drop. The blockages with round and elongated holes in this study increase the average heat (mass) transfer by 4.5 to 7.3 times over the corresponding fully developed channel flow value. The blockages with the smaller holes enhance the average heat (mass) transfer more than those with the larger holes, but also increase the pressure drop more than the blockages with the larger holes, by as much as 136%, for the same hole aspect ratio.

B. Heat Transfer Measurement

Supplementary experiments using copper heaters with embedded thermocouples were conducted to obtain average heat transfer on the channel wall segments downstream of blockages with round and elongated holes. The results of this experimental study are summarized as follows:

1. Blockages with holes significantly enhance the heat transfer on the channel wall segments downstream of the blockages, but they also cause substantial increases of the pressure drop, when compared with the heat transfer and pressure drop for fully developed flows at the same flow rates through a channel with the same cross section but no blockages.

2. The elongated holes in the blockages in this study enhance more heat transfer than the round holes, but they also cause larger pressure drops across the blockages.

3. The blockages with the larger holes in this study outperform the blockages with the smaller holes.

CHAPTER VI

TWO-PHASE POOL BOILING WITH NANO-STRUCTURED SURFACES: LITERATURE REVIEW

A. Background

Several modes of transport processes govern the characteristics of the various regimes of boiling. Scientific research of boiling and its application has spanned several decades since pioneering experiments by Nukiyama [34]. The author reported the boiling curve of water on metal wires in which he described the maximum and minimum heat flux values. Since then, extensive experiments and numerical simulations have been performed to investigate the transport mechanisms in pool boiling [35]. Past research efforts in pool boiling have been primarily focused on drawing the relationship between heat flux and wall superheat for a particular material or configuration (e.g., microgravity). Investigation of micro-scale effects in boiling have gained prominence in recent times primarily due to the promising potential of boiling to thermal management applications such as cooling of micro-electronic devices.

In the nucleate boiling regime, the transport processes are governed by three constituents: the working fluid, heated surface, and interface between the working fluid and heated surface. These processes are known to be three dimensional and nonlinear, and they mutually interact in a very complex manner. For example, the bulk liquid motion is affected by the bubble departure cycle, which in turn is affected by the hydrodynamic interactions between the bubble and the bulk liquid as well as the hydrodynamic interactions between the nucleating, growing, and departing bubbles. Dhir [36], Son et al. [37], Mukherjee and Dhir [38] performed extensive numerical and experimental studies of bubble nucleation and merger on artificially engineered surfaces. Zhang and Shoji [39] observed the high speed video images obtained from boiling experiments to verify the mechanism of nucleation site interaction on an artificial surface. These studies showed that the bubble interactions and mutual coalescence of growing bubbles on the heater surface could enhance the departure frequency of the growing bubbles. These studies also showed that the bubble departure frequency increased with the increase in the bubble coalescences between the adjacent bubbles regardless of the direction of the coalescence.

The surface temperature distribution is affected by the hydrodynamic and thermal interactions between neighboring bubbles. According to Kenning and Yan [40] and Zhang and Shoji [39], during the bubble growth on a heated surface, heat was removed from the contact area between the bubble and the surface due to micro-layer evaporation beneath the bubble followed by the surface quenching by the bulk liquid. As the bubble contact area changed on the heated surface, heat transfer occurred from the surface to the bulk liquid moving in toward the surface. However, this heat transfer was restricted to the projected area of the bubble on the heated surface. In the heater area in the vicinity of the nucleating and growing bubble - the heat transfer occurred by convective cooling due to the bulk liquid motion. This resulted in the region around the bubble having a lower temperature than the surrounding surface area. Mei [41] proposed that in nucleate boiling this cooling effect obstructed the departure of the growing bubble and suppressed the growth of the adjacent bubbles. Hence, it can be concluded that the thermal interactions reduced the bubble departure frequency by inhibiting the growth of the bubbles in the neighboring nucleation sites. The surface temperature fluctuations proposed in these studies were expected to be less than 500 μm in size and have time-scales less than 100 ms.

Film boiling on a horizontal surface encompasses hydrodynamic instabilities with length scales ranging from a few μm to 1 cm. Chang [42] firstly proposed a relation between the Taylor instability wave behavior and the film boiling process. Based on this theory, Zuber [43] postulated that the instability waves with the highest growth rates ("most dangerous wave") governed the bubble spacing and the departure frequency of the bubbles. Sernas et al. [44] proposed that the three dimensional most dangerous Taylor instability wavelength (3D) could be used to explain the bubble spacing in film boiling and was formulated as:

$$\lambda_{3D} = (2\pi\sqrt{3})\sqrt{\frac{\sigma}{g(\rho_l - \rho_v)}} \tag{6.1}$$

where σ is the coefficient of surface tension, g is gravitational acceleration, and ρ_v and ρ_l are density of liquid and vapor, respectively.

In the film boiling regime, the transport mechanisms are significantly different due to the prevalence of the Taylor instabilities [43]. Based on experimental data [45, 46, 47], Henry [48] proposed a bubble departure mechanism at minimum heat flux (MHF). According to this model - when a bubble departs from a heated surface, the liquid around the bubble moves in toward the surface and momentarily contacts and wets the local portion of the heated surface. This process is called "transient contacting" or "transient wetting." During the period of this "transient contacting", typically 0.05 s, the dominant heat transfer mechanism in the liquid is conduction. After the liquid contacts the heated surface, the rate of the local vapor generation at the liquid-solid interface causes evaporation resulting in the formation of a vapor film which ejects the liquid layer from the heated surface. As the liquid-vapor interface retracts, the rapid-heat loss causes the heated surface to be cooled down locally. The extent of local cooling is thought to depend on the liquid thermo-physcial properties, the latent heat of the vaporization, and the enthalpy of the heated surface. Such transient interactions are believed to govern a major proportion of the total heat transfer in film boiling. Recent analytical and numerical analyses performed by Banerjee and Dhir [4, 5] and Banerjee et al. [6], showed that the local cooling of the heated surface occurred at the point of minimum vapor film thickness and moved radially inward with time. This local cooling was manifested as a cold spot on the heated surface under a growing vapor bubble which was found to account for a major portion of the total heat transfer. At the cold spots on the heated surface, the temperature distribution at any instant was lower than the surrounding region. These temperature inversion regions had length scales in the order of 50-500 μm and time-scales in the order of 10-100 ms.

B. Review of Prior Research

1. Surface Temperature Measurement under Boiling Conditions

Prior investigations into micro-scale phenomena in boiling have primarily been restricted to hydro-dynamic measurements. To understand the dynamics of micro-scale effects in pool boiling, it is necessary to measure the micro-scale temperature fluctuations on the boiling surface. Various techniques have been reported in the literature for surface temperature measurements, which include: (1) liquid crystal thermography, (2) embedded thermocouple measurement, (3) electrical resistance measurement, and (4) radiation thermography measurement.

Kenning and Yan [40] used thermochromic liquid crystal with a high-speed video camera to measure the temperature fluctuations on the backside of a thin plate during nucleate boiling of water on the top surface. The heater was a thin, stainless steel plate of which the topside was exposed to water in the bottom of a glass container. The underside was coated with a thin layer of black paint, then a layer of thermochromic liquid crystal and finally a layer of polyester film for protection. Hue component of the video signal was quantitatively converted into temperature to provide information on the spatial variation on the plate surface at a given wall superheat. With this method, the authors could obtain continuous wall temperature distributions at each time step. However, the liquid crystal thermography method has a number of restrictions in its measurement. The liquid crystal used in this experiment had a color-play range from 104°C to 123°C, which was too small to cover the whole range of surface temperature variations for nucleate and film boiling regimes, which were of interest for the current investigation. Also, measurement precision was compromised by this technique since the temperature was calculated using a nonlinear hue-temperature calibration curve. The spatial resolution with the liquid crystal method was limited to 0.25 mm by the camera resolution. This was inadequate for measuring the cold spots which were typically less than 200 μm in size. The data also had a high frequency noise which restricted the temporal resolution as well. Hohmann and Stephan [49] used thermo-chromatic liquid crystals in an un-encapsulated form to study the cold spot formation at an evaporating liquid meniscus. Chromatic property variations of the liquid crystals with temperature were used to measure the temperature field using a microscope attached to a camera. However, the temporal resolution of this technique was limited.

To measure the temperature and heat flux on a surface in pool boiling, a wire-bead thermocouple was embedded into a heated block by Haramura [50] at a distance less than a millimeter from the sueface of the heated block. The authors employed a high response thermocouple in a solder block on the top of a copper block which was heated by a PID controller. An 80 μm O.D. E-Type bare wire thermocouple, insulated with glass, was installed in the solder block beneath the top surface of the heater block. The two wires of the thermocouple were not connected directly to form a junction. They were connected using solder with an intervening distance of approximately 0.5 mm between the two ends of the wires. The sampling rate of the temperature measurement with the thermocouple was 4kHz and the data was recorded for 3.2 s. The complex configuration of the thermocouple, however, restricted the spatial resolution which was needed for characterizing boiling phenomena.

Ohtake and Koizumi [51] measured the electrical resistance of a platinum wire to investigate the mechanism of vapor-film collapse above the thermodynamic limit of liquid superheat. A platinum wire, 1 mm thick and 160 mm long, was connected to a silver electrode inside a double-wall glass vessel. The power was supplied to the platinum wire directly through a DC power supply; both ends of the wire were heated from a cartridge heater through the silver electrode. A number of voltage taps of fine platinum wires were spot-welded to the platinum wire at an interval of 20 mm to measure local electrical resistance. From the experimental results, the authors postulated that the average temperature at MHF (Minimum Heat Flux) was elevated to higher values while the local temperature values in the cooler section of the wire was reduced. The authors performed a numerical simulation with the experimental data and concluded that the vapor film started to collapse in the region where the local temperature was lower than the minimum temperature required to support a stable film of vapor. However, this experimental method was applicable only to wire heaters where the measurement of temperature fluctuations was indirect and provided very low spatial resolution for estimating the local temperatures on the heated surface.

Zhang and Shoji [39] introduced the Nd-YAG laser irradiation method to investigate the nucleation interaction in pool boiling of water on an artificial surface. The surface was a silicon plate with 0.2 mm thickness and 15 mm diameter on which two cylindrical cavities with dimensions of 10 μm diameter and 80 μm depth were microfabricated. The spacing between the two cavities was the main parameter of this study. Nd-YAG irradiation was used to heat the bottom surface of the silicon plate and the temperature fluctuation was measured by a radiation thermometer along a line between the two cavities. The radiation thermometer provided a spatial resolution of 120 μm and a temporal resolution of 3.0 ms with a temperature measurement precision of 0.80 K.

Park and Taya [52] used thin film thermocouples to measure temperatures at a high spatial resolution. They used T-type thermocouples with a thickness of 150 nm. A 10 × 10 junction array in a 1 cm × 1 cm area was used in this study. Kreider and Gillen [53], and, Kreider and DiMeo [54] extensively studied different materials for making TFT to measure high temperatures. Various factors were considered for choosing the correct material for making the TFT. The properties of the metals and their interactions with other metals and the surrounding environment were considered. Uniform composition of the TFT was of great importance for functionality and calibration purposes. The authors proposed using adhesion enhancers since platinum was used for deposition.

Henry and Kim [55] used an array of thin film heaters to study temperature fluctuations in boiling and spray cooling. The size of each heater element was 270 μm which was larger than the size of cold spots (less than 200 μm in diameter). Also, the act of measurement using the heaters could interfere with the local transport mechanisms that govern the formation of cold spots.

2. Boiling Heat Transfer Enhancement Using Engineered Surfaces

Boiling heat transfer can be enhanced by increasing the degree of liquid sub-cooling and employing various types of engineered micro-structured surface morphologies (e.g., surface micro-machined structures, graphite foams, porous surfaces, etc.).

Many researchers reported the enhancement of heat transfer by using newly developed materials or structures combined with pool boiling. Ramaswamy et al.

[56] conducted experiments after employing an enhanced structure composed of six layers of copper plates having rectangular channels cut on either side of the plate to investigate the combined effect of pressure and sub-cooling on the boiling performance of the enhanced structure. The authors reported that the enhanced micro-structure showed high heat flux. The combined effects of sub-cooling and pressure were found to enhance the performance of boiling systems. Ramaswamy et al. [57] also performed experiments to investigate the effect of the dimensions of the enhanced structure on boiling performance. The authors parametrically changed the pore size, pitch and height to optimize the dimensions for maximizing heat transfer. They postulated that the increase in pore size and reduction in pitch would augment the heat dissipation at wall superheat ranging from 4 K to 12 K. However, by increasing the number of stacks, they could obtain high heat dissipation at low and high wall superheat. At intermediate wall superheat, multi-layer stacks were found to have almost the same heat dissipation as a single-layer stack. Research of an enhanced structure was also conducted by Mudarwar and Anderson [58]. The authors employed a cylindrical pin-fin with micro-structures machined into its perimeter for heat transfer enhancement on an electronic chip surface. The test fluid for this experiment was FC-72 and the experiments were performed under saturated and 35°C sub-cooled conditions. By combining the micro-structured surface and sub-cooling, the authors achieved very high critical heat flux (CHF) values on the electronic chip surface. Coursey et al. [59] applied graphite foams to the thermal management of electronics. The foams consisted of graphite ligament which has a thermal conductivity up to five times greater than copper. The bulk graphite foam has a thermal diffusivity four times greater than that of aluminum due to its high thermal conductivity and low density. The effects of chamber pressure, liquid level, and test fluid on the nucleate boiling were considered in the experiments. The authors claimed that the use of graphite foams

as an evaporator in a thermosiphon enhanced the cooling of electronics, especially in the lower chamber pressure due to an increase in saturation temperature.

Since the discovery of carbon nanotubes (CNT) by Iijima [60] in 1991, there has been growing interest in the various applications of CNT. CNT have very broad ranges of thermal, electrical, and structural properties, and various molecular structural types (length, diameter, and orientation), that may be tailored to various applications. According to Berber et al. [61], the thermal conductivity of CNT is 6,600 $W/(m \cdot K)$, or about 16.5 times that of copper, at room temperature, but has a much lower value, at 400 K, of 3,000 $W/(m \cdot K)$, or about 7.6 times that of copper. Recently, research using the enhanced thermal properties of carbon nanotubes was launched for heat transfer enhancement in electronic chips.

In [3], Ujereh et al. reported the results of their experiments on nucleate pool boiling of FC-72 on a carbon nanotube array on a silicon surface under saturated boiling conditions. The area of the heated surface was 12.7 mm × 12.7 mm. The multi-walled carbon nanotubes (MWCNT) were synthesized using a calcined dendrimer catalyst in a plasma enhanced chemical vapor deposition (PECVD) system. The MWCNT were 30 nm in diameter and 20 to 30 μm in length. As a result, the authors postulated that the MWCNT coated on a silicon wafer increased the CHF value by 50% and enhanced the heat transfer coefficient by 400% compared to a bare silicon wafer. However, this study was restricted to the nucleate boiling condition and the performance of the nano-structured surface over the film boiling regime was not reported. The authors noted that the synthesized MWCNT did not provide complete surface coverage. Although the authors showed only SEM pre-experiment images of the MWCNT, not post-experiment images of the MWCNT, they reported no significant degradation of the bonding of the MWCNT structure to the substrate as a result of the experiment.

CHAPTER VII

TWO-PHASE POOL BOILING WITH NANO-STRUCTURED SURFACES: EXPERIMENTAL APPARATUS AND PROCEDURE

A. Experimental Apparatus

1. Heat Transfer on Nano-Structured Surface

Experiments were performed to study the effect of carbon nanotubes grown on a silicon wafer on boiling heat transfer under three different experimental conditions:

1. saturated condition
2. 5°C sub-cooled condition
3. 10°C sub-cooled condition

The experiments were conducted under nucleate boiling and film boiling conditions. During the experiments, the surface temperature of the nano-structured surfaces could not be measured directly due to their closely aligned morphology. To estimate the surface temperature, a supplementary boiling experiment was conducted using a silicon wafer with micro-machined thin film thermocouples (TFT) on top. This experiment was used to determine the overall thermal resistance correlation between the top surface of the silicon wafer on which boiling occurred and the top surface of the copper cylinder. The supplementary experiment will be discussed in the following section.

The main component of the experimental apparatus was one of three silicon wafers affixed to the top of the copper cylinder. The top surfaces of two of the silicon wafers were coated with multi-walled carbon nanotubes (MWCNT), while the surface of the third silicon wafer was smooth. During an experiment, the top surface of the silicon wafer, with or without MWCNT on it, was exposed to the test fluid of PF-5060 in a viewing chamber with three glass windows, as shown in Fig. 25. Heat was supplied to the copper cylinder from five cartridge heaters embedded in the copper cylinder which was shrouded by a cylindrical stainless steel jacket with an air gap separating the copper cylinder and the stainless steel jacket. A tubular heater was used to raise the temperature of the test fluid and to maintain the test fluid at its saturation temperature of 56°C. For sub-cooled boiling experiments, the temperature of the test fluid was kept below its saturation temperature with a coolant that was circulated from a constant temperature bath through a copper coil located just below the surface of the test fluid. Figure 38 shows a schematic of the experimental apparatus and the instrumentation for the boiling experiments in this study.

a. Synthesis and Growth of MWCNT on Silicon Wafer

For the pool boiling experiments in this study, two silicon wafers were coated with MWCNT arrays using chemical vapor deposition (CVD) techniques. The MWCNT array on one of the silicon wafers had a height of 9 μm and that on a second silicon wafer had a height of 25 μm. Figure 26 shows SEM images of the MWCNT arrays on the silicon wafers. The details about the CVD process for the synthesis and growth of MWCNT arrays are described in [62]. Vertically aligned MWCNT arrays with a diameter of 8 to 15 nm were synthesized by flowing 5-mol% C_2H_2 at 580 sccm (standard cubic centimeter per minute) in helium at atmospheric pressure in a quartz tube furnace that was maintained at 680°C. The synthesis time could range from a few seconds to 10 minutes because the growth rate of the MWCNT was about 1 to 2 μm/min. Prior to performing the CVD synthesis of MWCNT, a 5-nm thick iron

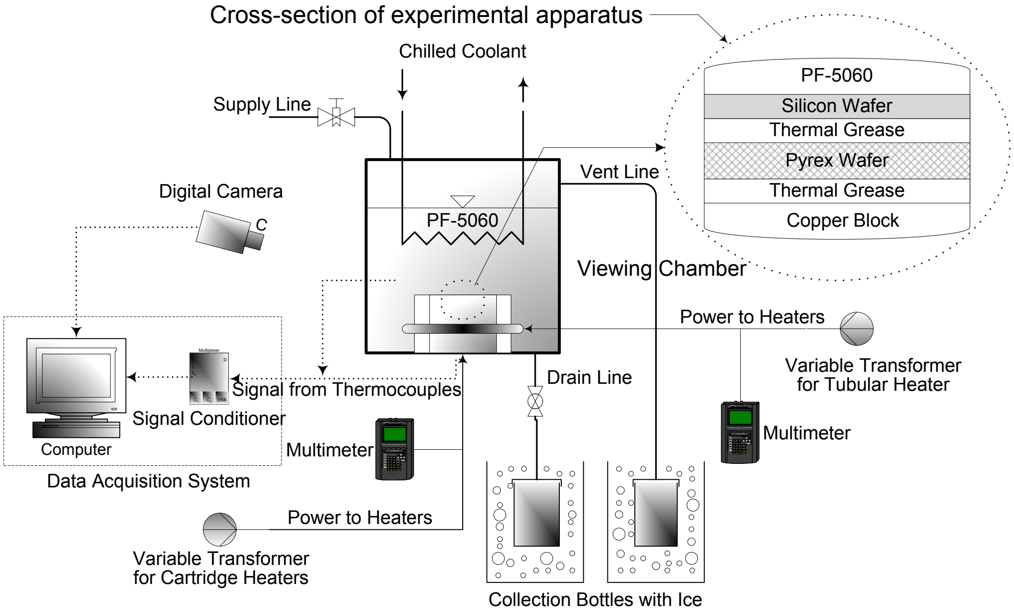

Fig. 24. Design of experimental apparatus for boiling experiment with nano-structured surfaces: Schematic diagram of experimental apparatus.

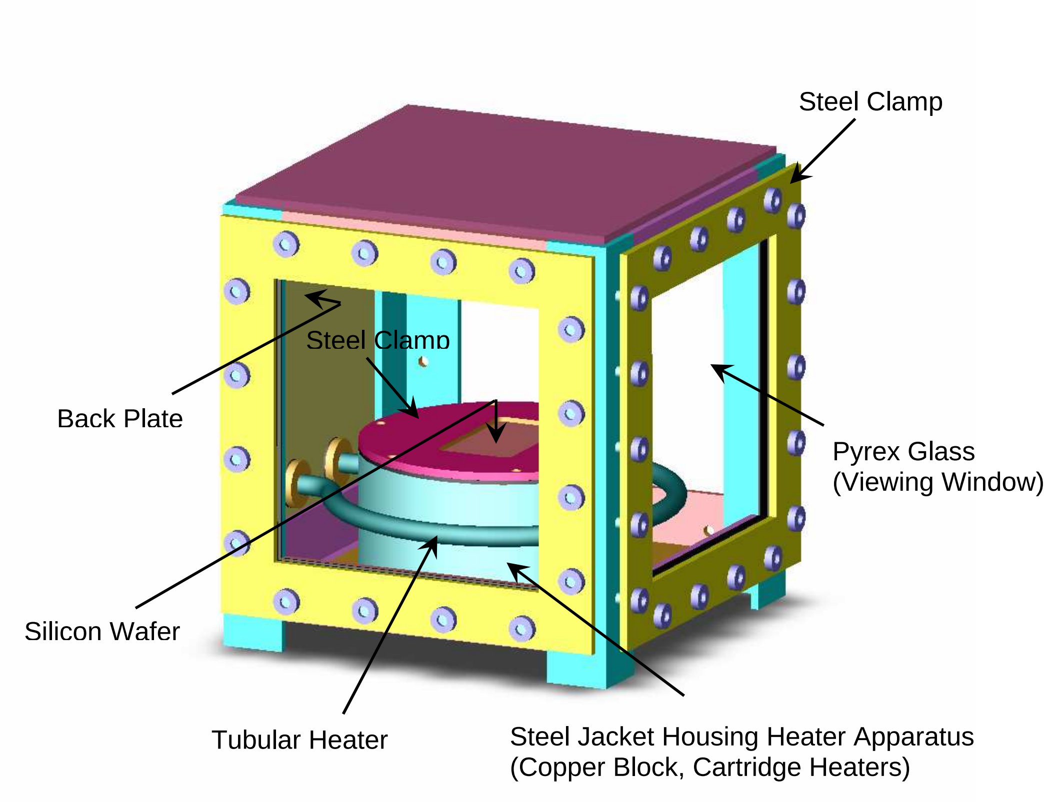

Fig. 25. Design of experimental apparatus for boiling experiment with nano-structured surfaces: 3-Dimensional model of viewing chamber.

film was deposited on the silicon wafers by electron beam evaporation to serve as a catalyst. It was reported in [62] that, based on SEM images and thermal gravimetric measurements, the purity of the MWCNT obtained was very high, with about 96 to 98% carbon in the form of MWCNT, and 2 to 4% iron and amorphous carbon. No carbon particles were observed in this investigation. Figure 27 shows the schematic of the chemical vapor deposition process.

b. Test Section

The copper cylinder had a diameter of 8.9 cm and a height of 5.1 cm. The cylinder was enclosed in a stainless steel jacket with an inside diameter of 9.9 cm and a thickness of 0.76 cm. The silicon wafer was held in place on the top of the copper cylinder with a steel disk that was affixed to the top of the stainless steel jacket with screws. The area of the silicon wafer (with or without MWCNT on it) exposed to the test fluid was 5.9 cm × 3.2 cm with rounded corners that had a radius of 0.3 cm. Five cartridge heaters (three rated at 500 W and two at 300 W) were inserted horizontally into the copper cylinder near its bottom to supply heat to the cylinder. A pyrex wafer was sandwiched between the silicon wafer and the top of the copper cylinder to minimize electrical noise from the heaters. High thermal conductivity grease (Manufacturer: Dow Corning, Model: 340 Heat Sink Compound) was used to minimize thermal contact resistance between surfaces at the various interfaces. Twelve K-type thermocouples were used to determine the temperature distribution in the copper cylinder. The junctions of these thermocouples were installed inside the copper cylinder at various distances from the top of the copper cylinder and at various radial locations. Figure 28 shows the copper cylinder used in this experiment. An additional thermocouple was placed in the test fluid of PF-5060 to monitor the bulk temperature. During an experiment, the output from all of these thermocouples

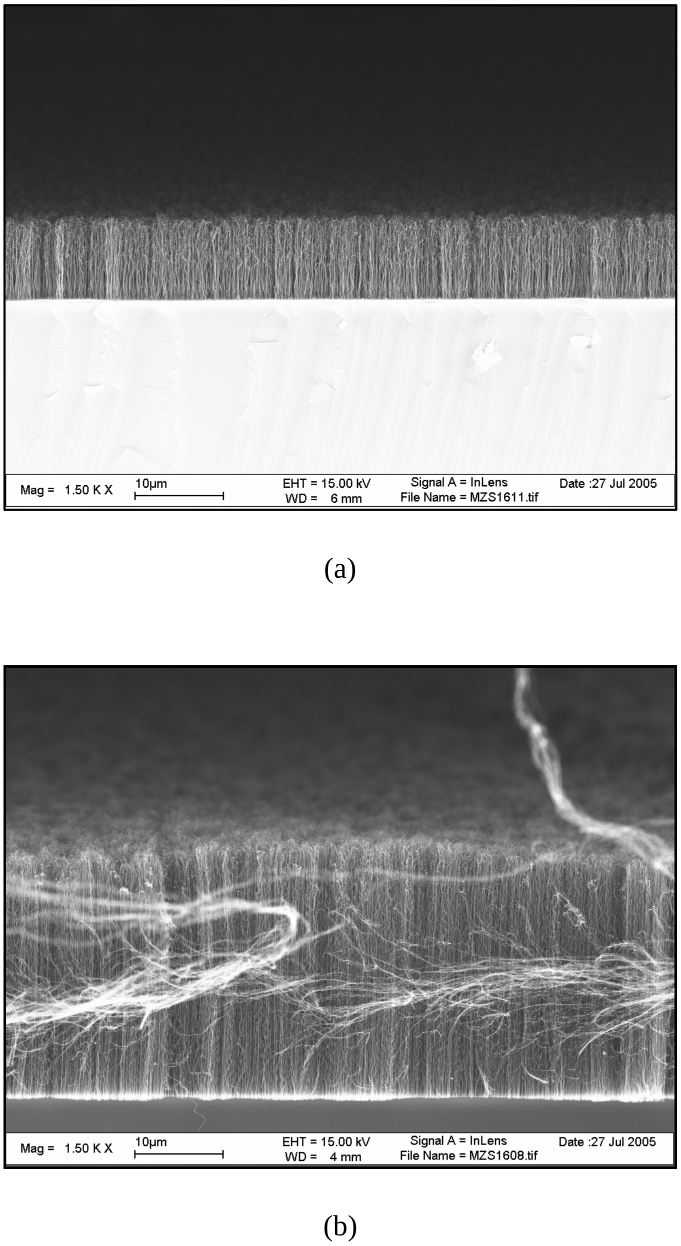

(a)

(b)

Fig. 26. SEM image of MWCNT synthesized on silicon wafer. (a) Type-A: 9 μm height. (b) Type-B: 25 μm height (Source: Dr. R. H. Baughman et al. at the Nanotech Institute, University of Texas at Dallas).

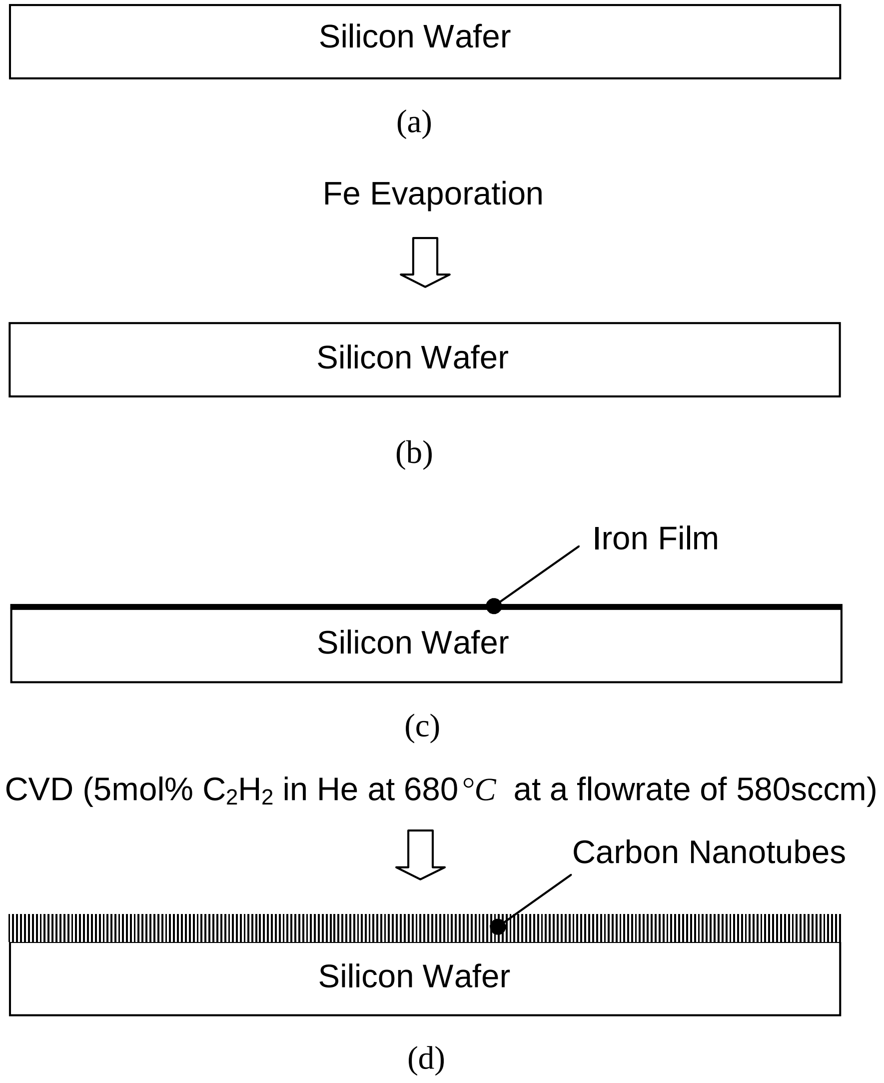

Fig. 27. Schematic depicting the chemical vapor deposition process of carbon nanotubes on a silicon wafer: (a) Preparation (b) Fe evaporation (c) Iron film deposited on the silicon wafer (d) Chemical vapor deposition.

was recorded with a computer-controlled data acquisition system.

c. Viewing Chamber

The structural frame of a viewing chamber was constructed of 2.54 cm × 2.54 cm steel L-beams with a thickness of 0.318 cm. The beams were cut and welded together to form a cubic frame, with the length of each side being 15.2 cm. The top, bottom, and back walls of the viewing chamber were constructed of 0.64-cm thick steel plates, while the front and two side windows were pyrex glass with a thickness of 0.318 cm. To prevent cracking due to thermal expansion, a steel frame and rubber gaskets on both sides of each glass pane were used to mount the glass pane to the frame of the viewing chamber using bolts, nuts, and washers [Fig. 25]. Several holes in the back steel wall vented the evaporated test fluid from the chamber and maintained the test fluid in the viewing chamber at atmospheric pressure. The evaporated test fluid was ducted to an open container, placed in an ice chest filled with ice, where it condensed.

d. Cooling Unit for Sub-cooled Boiling Experiment

During sub-cooled boiling experiments, the test fluid of PF-5060 was maintained at a constant temperature of 5°C or 10°C below its saturation temperature with a coolant in a coiled copper tube that was submerged 1.5 cm below the surface of the test fluid. The coolant was circulated from a constant temperature bath (Manufacturer: PolyScience, Model 9612) with an electronic controller to the coiled copper tube, and the flow rate and the temperature of the coolant were adjusted and monitored to achieve the desired sub-cooling of the test fluid. To minimize heat loss from the test fluid to the environment, an insulation tape was wrapped around the copper tube between the test section and the constant temperature bath. During saturated boiling experiments, the coiled copper tube was lifted above the surface of the test

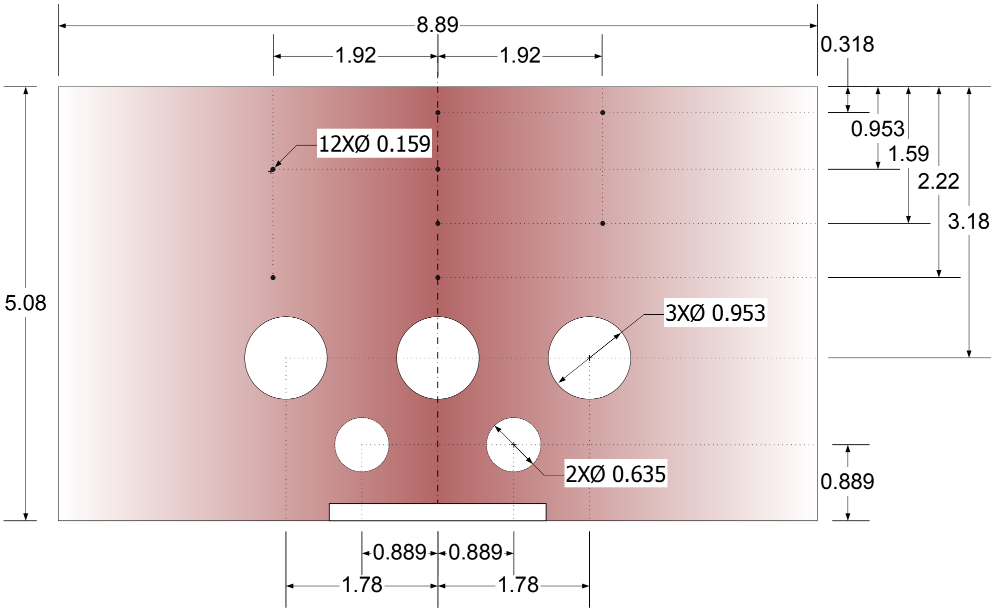

Fig. 28. Schematics of copper cylinder used in the experiments (unit: cm).

fluid to condense the vapor generated during the experiments.

2. Surface Temperature Measurement Using TFT

An experiment was performed to measure the surface temperature on a silicon wafer with a micro-machined thin film thermocouple (TFT) in nucleate and film boiling under saturated conditions.

The experimental apparatus consisted of four different parts:

1. a silicon wafer (containing surface micro-machined thin film thermocouples)
2. a test section (consisting of a copper cylinder covered with a steel jacket, embedded thermocouples, and cartridge heaters)
3. a viewing chamber used for housing
4. a cooling unit

The temperature measurements were performed using a computer-controlled high speed data acquisition system. Fig. 29 shows the schematic diagram of the experimental setup for the nucleate and film boiling experiments.

a. Silicon Wafer with Micro-Machined Thermocouple

Photolithography was used for making the desired features on a silicon wafer. Thin film thermocouples were fabricated in the class 1000 cleanroom of Material Characterization Facility, Texas A&M University. The fabrication process consisted of:

1. Photolithography
2. Oxygen Plasma Cleaning

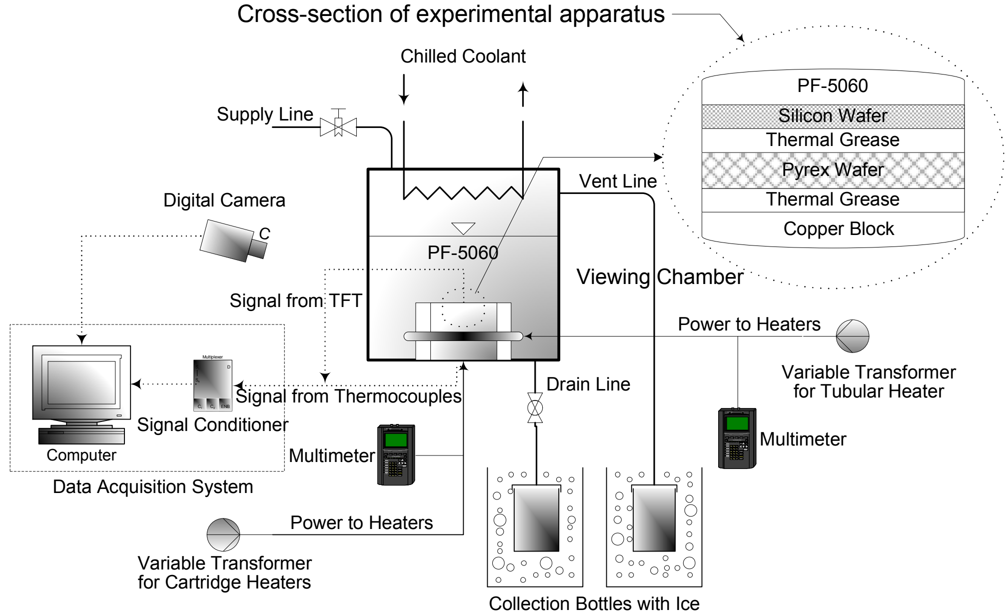

Fig. 29. Design of experimental apparatus for surface temperature measurement using TFT: Schematic diagram of experimental apparatus.

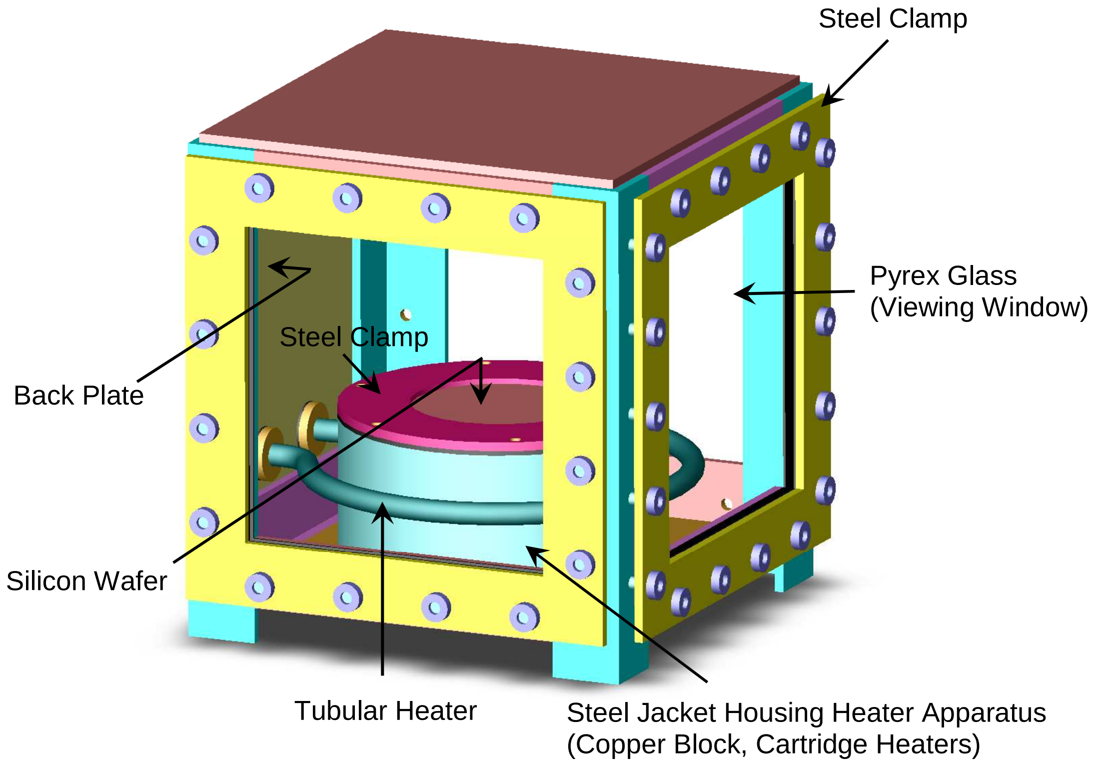

Fig. 30. Design of experimental apparatus for surface temperature measurement using TFT: 3-Dimensional model of viewing chamber.

3. Metal Deposition
4. Lift-off

The details about the process for micro-fabricating the thin film thermocouples on a silicon wafer are described in [63].

PHOTOLITHOGRAPHY

A photolithography process was used to make a desired pattern on a silicon wafer. The process involved:

1. Cleaning: a silicon wafer was first cleaned using acetone and then thoroughly rinsed off using Iso-propanol. The silicon wafer was dried using pressurized nitrogen.

2. Heating: to evaporate any volatile impurities that might be on the silicon wafer, the silicon wafer was heated at 200°C on a hot plate for five minutes.

3. Spin Coating: Shipley 1827 photoresist was spin coated on the silicon wafer using a SCS P6204 (20.3 cm bowl) non-programmable spin coater. After the silicon wafer was held by a vacuum chuck, the device started to spin to coat the photoresist on the silicon wafer. The time and speed of spinning was determined by the desired thickness of the photoresist layer. For this application, the time and speed were set at 60 s and 3000 rpm, respectively.

4. Pre-Baking: After the spin coating, the silicon wafer was heated at 115°C on the hot plate for 60 s.

5. UV Light Exposure: The photoresist was patterned using a Quintel Q400 MA mask aligner. The UV light exposure time was determined by the type of photoresist. For this application, it was set from 8 to 30 s.
6. Developing: The silicon wafer was developed using MF-319 (Manufacturer: MicroChem) developer to remove any unnecessary parts of photoresist from the silicon wafer. The development time was set according to the UV light exposure time. For this application, it ranged from 40 to 90 s.
7. Cleaning: After the development, the silicon wafer was rinsed with only distilled water and then dried using pressurized nitrogen gas.

OXYGEN PLASMA CLEANING

Oxygen plasma cleaning was carried out using a March Plasma System Model CS-1701 reactive ion etcher (RIE) to remove organic components on the silicon wafer. The settings used for this application were as follows:

- Pressure: 0 mtorr
- Power: 350 W
- Time: 10 s
- Temperature: 0°C
- Endpt: 100
- BP/RP: 80 mtorr
- Gas 1(Oxygen): 20 sccm

The process of oxygen plasma cleaning was optional. By performing this process, the height of the photoresist was marginally reduced and excess photoresist on the silicon wafer could be cleaned. This step assisted the lift-off process which followed the photolithography step.

METAL DEPOSITION

Metal deposition of each component of TFT on the silicon wafer was carried out by using a BOC Edwards Auto 306 Meta Evaporation Chamber. This process started with vacuuming the chamber lower than 1×10^{-6} torr. At such low pressure, the metal that is being heated starts to evaporate at its low melting point and the vapor is deposited onto the silicon wafer placed above the metal source. During the process, the silicon wafer was fixed onto the cover plate and the plate was revolved to ensure a uniform deposition onto the silicon wafer. In this system, two different metal sources can be used at the same time. For this application, Chromium and Alumel were used for the first component of TFT and Chromium and Chromel used for the second component of TFT. The Chromium was used as an adhesion layer. The junction of the two alloys form a K-type TFT. The thickness of the chromium adhesion layer was approximately 15-20 nm and the target heights of the deposition of Alumel and Chromel were greater than 200 nm. For the evaporation, two parameters, i.e., density and z ratio (on quartz microbalance) of the metal, must be set to enable the system to calculate the deposition rate of the metal on the silicon wafer. This system employed the resistive heating method for the physical vapor deposition (PVD) process. For this application, a tungsten rod was used for its facilities. After the completion of the PVD process, the chamber was given ample time to cool down to reduce the formation of an oxide layer on the surface of the silicon wafer.

LIFT-OFF

This was the final step in the process of fabricating thermocouple leads on the silicon wafer. After the metal deposition, the photoresist must be removed from the silicon wafer by using Remover PG (Manufacturer: MicroChem). In this process, the temperature of a ultra sonic bath in which the lift-off process was performed was the primary factor that was monitored. For this application, the temperature of the bath was maintained at 65°C. The lift-off process was sensitive to the time required for ultra-sonication. Hence this process required continuous monitoring. After this process, The Remover PG was washed off by using Iso-Propanol and then the silicon wafer was dried by using pressurized nitrogen gas.

COMPOSITION OF THIN FILM THERMOCOUPLE

For this application, two deposition steps were performed: The first deposition step was for fabricating a negative lead of a thermocouple and the second deposition step was for fabricating a positive lead of the thermocouple. The second deposition step was similar to the first deposition step except for the "UV light exposure" in the photolithography process. For the second deposition step, care must be taken to form a thermocouple junction. For the junction formation, the lead end of the thermocouple that was already fabricated during the first deposition step must be aligned with the one that would be fabricated during the second deposition step. For this purpose, alignment marks were patterned on all four corners of the silicon wafer in the process of the first deposition step and used for matching the lead end that would be fabricated in the process of the second deposition step.

For this experiment, as mentioned earlier, K-type thermocouples were surface micro-machined on a silicon wafer. K-type thermocouples consist of Chromel (+) and

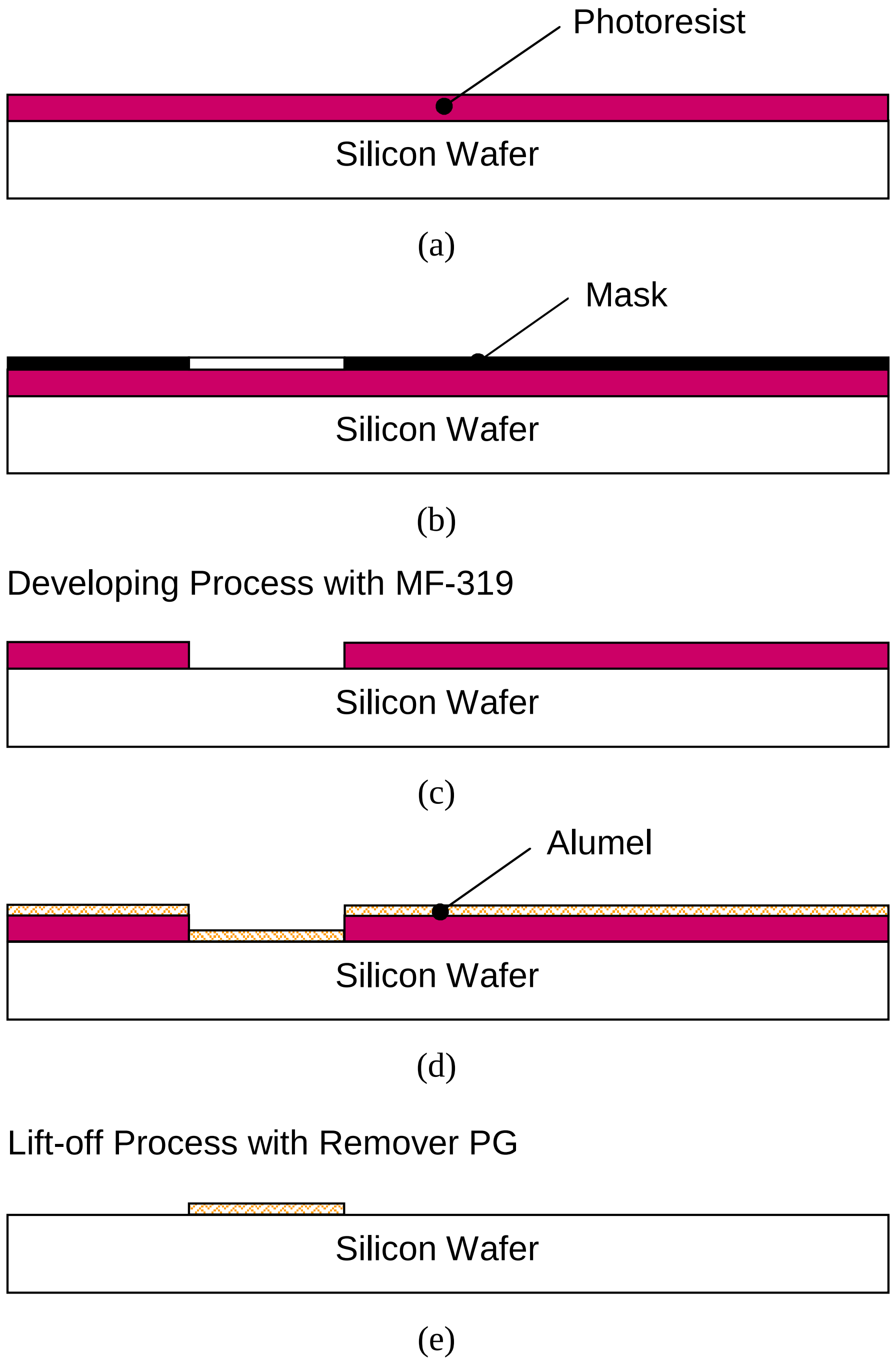

Fig. 31. Schematic depicting the fabrication process of thin film thermocouple on a silicon wafer (the first layer): (a) Spin coating (b) UV light exposure (c) Developing (d) Metal deposition (e) Lift-off.

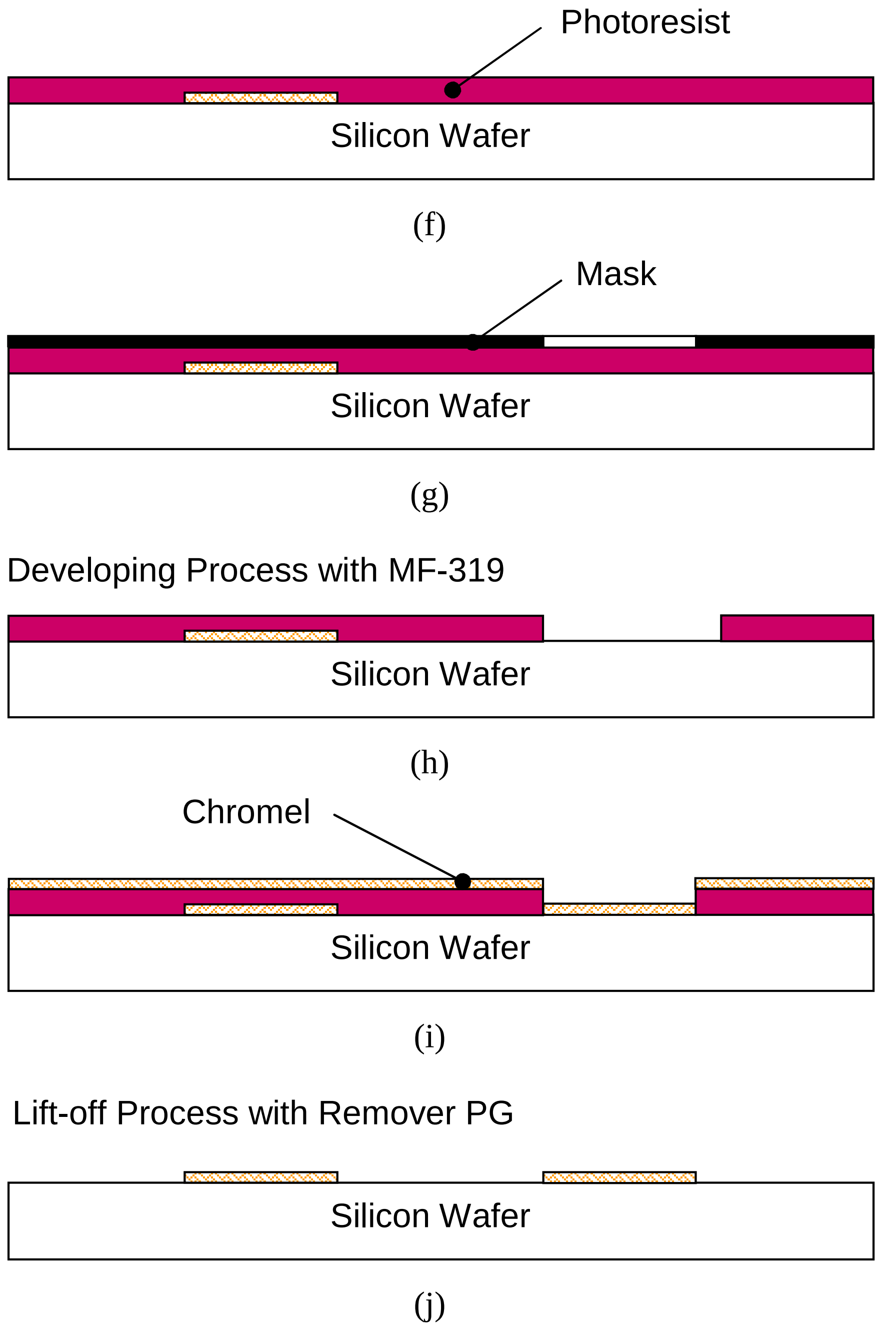

Fig. 32. Schematic depicting the fabrication process of thin film thermocouple on a silicon wafer (the second layer): (f) Spin coating (g) UV light exposure (h) Developing (i) Metal deposition (j) Lift-off.

Alumel (-) junction. The composition of Chromel is 90% Nickel and 10% Chromium. The composition of Alumel is 95% Nickel and 5% Aluminum. K-type thermocouples were chosen for their ease in micro-fabrication because the metal alloys are easily amenable as targets for the physical vapor deposition process and have a high sensitivity and broad range of linear response to the temperature range of the experiments (50-250°C). The targets were formed by using Chromel and Alumel wires (Manufacturer: Omega Inc.). In the layout diagram of Fig. 33, the width of both Chromel and Alumel layers was around 50 μm and the pitch of the thermocouples is 200 μm. An array of 5×2 thermocouples was fabricated in an area of 0.8 mm × 0.2 mm on the surface. In this experimental apparatus, the wires from the heaters and the thermocouples that were embedded in the copper cylinder were routed under the bottom of the copper cylinder and taken out from the bottom of the viewing chamber.

PACKAGING

A number of interconnect methods were explored for packaging the TFT, which included soldering, wire bonding, and bonding with silver paint. Among them, bonding with silver paint was employed for this application because of its stiffness up to the surface temperature of ~200°C and ease in curing.

This method, designed by the author, used the properties of silver paint, i.e.:

- high electrical conductivity
- strong adhesiveness
- high flexibility

With these properties, silver paint (Manufacturer: GC Electronics) was applied to a couple of TFT bondpads fabricated on the silicon wafer for connecting the TFT

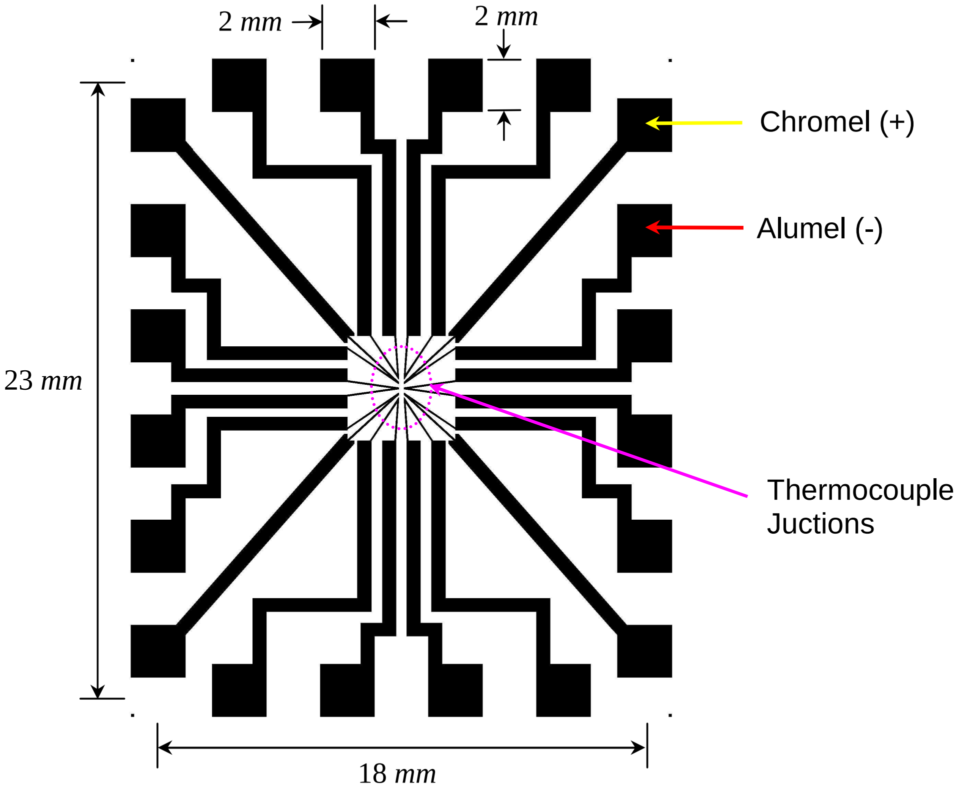

Fig. 33. Schematics of the micro-machined temperature sensors fabricated on a silicon wafer surface [63].

wires to standard thermocouple wires to form a circuit. A couple of 24-gage K-type thermocouple (by Omega Engineering) wires were cut to 1.5 cm in length and affixed to the bondpads by using silver paint. Care must be taken in connecting the standard thermocouple wires to the bondpads; the same type of materials should be in contact. In this process, alligator clips were used to support the wires to be positioned on the top of the bondpads during the bonding step. The curing time of the silver paint to be dried was around 24 hours at ambient temperature. After the silver paint was dried, the alligator clips were released from the standard thermocouple wires. Prior to performing this bonding, the other ends of the 24 gage thermocouple wires were welded to a couple of 36 gage K-type thermocouple wires to connect the TFT wires to a data acquisition system. To tighten the interconnection up to the high temperature, JB Weld (Manufacturer: J-B Weld Company) was applied around the junction between the 24 gage thermocouple wires and the bondpads.

b. Test Section

The test section used for measuring the surface temperature using the TFT was the same as the test section which was used for the boiling experiments performed on nano-structured surfaces except for the silicon wafer and the steel clamp. In this experiment, the silicon wafer with the TFT fabricated on top was placed on the top of the copper cylinder and clamped with an annular steel disk which had 6.35 cm and 11.4 cm inside and outside diameters, respectively. The area of the silicon wafer (with the TFT on top) exposed to the test fluid was 31.7 cm^2.

c. Viewing Chamber

The viewing chamber used for this experiment is shown in Fig. 30. It was the same as the viewing chamber used for the boiling experiments performed on nano-structured

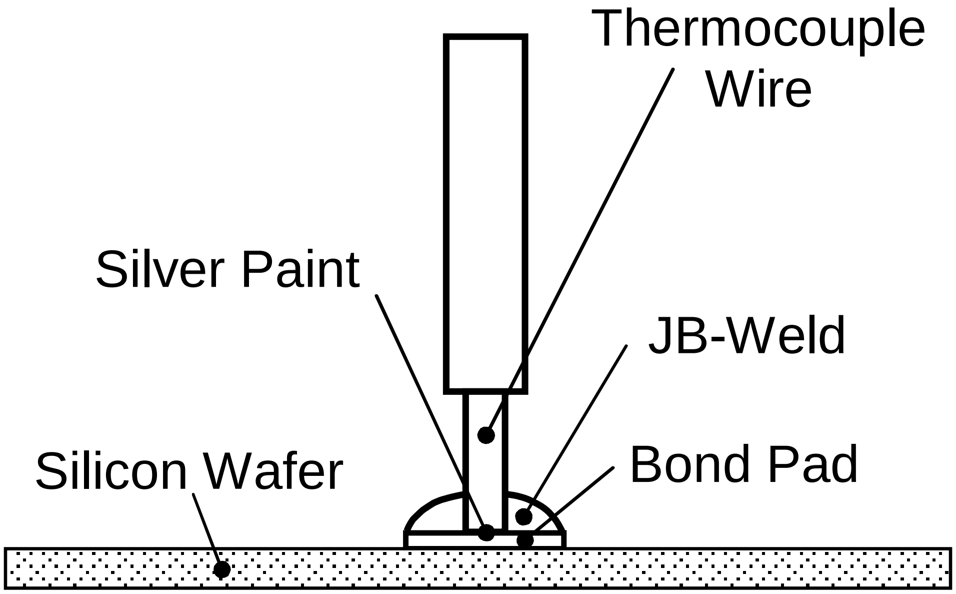

Fig. 34. Schematics of packaging (bonding with silver paint).

surfaces except that the thermocouple wires which were connected to the TFT were passed through the top plate. To minimize the loss of the evaporated test fluid through the viewing chamber, especially the top plate, the thermocouple wires were taped on the top frame of the viewing chamber and then bolted tightly with the top plate. A rubber gasket was placed between the top frame and the top plate.

d. Cooling Unit

For this experiment, the coiled copper tube was lifted up above the level of the test fluid (PF-5060) to condense the vapor generated during the experiment. The coiled copper tube and the constant temperature bath used for this experiment were the same as the ones used for the boiling experiments performed on nano-structured surfaces. The details about the cooling unit was discussed in the previous section

B. Experimental Procedure

1. Heat Transfer on Nano-Structured Surface

Pool boiling experiments were conducted under steady state conditions. To initialize an experiment, one of the three silicone wafers was affixed to the top of the copper cylinder and the viewing chamber was filled with the test fluid of PF-5060. For a saturated boiling experiment, the power was supplied to the tubular heater to boil the test fluid for over five minutes to remove dissolved gases in the test fluid. The input power to the tubular heater was then adjusted to maintain the test fluid at its saturation temperature.

For a sub-cooled boiling experiment, After the coiled copper tube was lowered to a level of about 1.5 cm below the surface of the test fluid, coolant was allowed to flow through the coiled copper tube to achieve the desired degree of sub-cooling of the test fluid. Prior to each test run, the test fluid was boiled by the tubular heater to remove dissolved gases in the test fluid.

After sufficient time was allowed for the test fluid to reach its saturation temperature or a temperature of 5°C or 10°C below its saturation temperature, heat was supplied to the copper cylinder by varying the power input to the cartridge heaters in the copper cylinder. For a nucleate boiling experiment, the initial voltage drop across the cartridge heaters was set so that the temperature on the silicon surface was just above the saturation temperature of the test fluid and natural convection could occur on the surface. The voltage drop was then increased in steps of 5 volts until the critical heat flux (CHF) condition was achieved. To obtain the CHF value, the voltage input to the heaters was reduced quickly just before an abrupt increase of the surface temperature was detected on the heated surface. The heater voltage drop was then increased in steps of 1 volt until the maximum heat flux value was reached.

After the critical heat flux value was obtained, the voltage input was increased slightly to cause film boiling to occur on the heated surface. The heater voltage drop was decreased quickly for the first measurement point in the film boiling regime. After that, the heater voltage was gradually decreased in steps of 1 to 3 volts until transition from film boiling to nucleate boiling occurred. After each time the heater voltage drop was set, for both nucleate boiling and film boiling, a period of 2 to 3 hours was allowed for a steady state to be reached. A longer time was necessary for a steady state to be attained in film boiling. A saturated boiling experiment took 24 to 30 hours to complete, and a sub-cooled boiling experiment took over 35 hours to complete.

After a steady state condition was reached, the temperature in the copper cylinder was recorded with the computer-controlled data acquisition system at a sampling rate of 200 Hz. The data acquisition system consisted of NI SCXI-1102C Analog

MUX, and PCI-6251 DAQ Board with Pentium-4 3.2 GHz computer, and controlled by a program coded using Labview 7.1. The liquid pool temperature and ambient air temperature were also monitored. To estimate the power input to the copper cylinder during an experiment, the heater voltage drop and current were measured with a digital TRMS voltmeter and a digital TRMS clamp ammeter, respectively. During an experiment, the test fluid was replenished periodically to maintain the fluid level at about 5 cm above the silicon wafer surface.

2. Surface Temperature Measurement Using TFT

a. Calibration of TFT

Thin Film Thermocouples were fabricated by the physical vapor deposition process which may cause the composition of the thermocouples to be different from the targeted values. Also, the interconnection of the TFT with standard thermocouple wires for forming a temperature measurement circuit may have some possibility of change in response to a temperature variation. To obtain accurate surface temperature data during boiling experiments, the calibration of the TFT was performed prior to the test run.

To increase the reliability of the result, the calibration was performed in the viewing chamber in which surface temperature measurement experiments would be conducted. After all the experimental set-up for the surface temperature measurements was ready, a standard K-type wire-bead thermocouple was attached to the silicon wafer surface in the vicinity of the TFT. Prior to this calibration, the standard wire-bead K-type thermocouple was calibrated against a NIST calibrated mercury thermometer. During the calibration experiment, the top of the viewing chamber was closed to reduce the convection effect on the measurement.

The first temperature measurement was conducted without any power input to the cartridge heaters to obtain the response of the TFT at the lowest temperature point. After this measuring point, the power input to the cartridge heaters was adjusted by a variable transformer and increased up to 20 volts in steps of 5 volts. At each measuring point, the temperature from the TFT was recorded with the temperature from the standard wire-bead K-type thermocouple after a steady state condition was attained. Using the computer controlled data acquisition system, the temperature data were collected for 2 minutes with a sampling rate of 200 Hz.

b. Surface Temperature Measurement

The experimental procedure for this experiment was similar to the experimental procedure for the boiling experiments performed on nano-structured surfaces. The only exception was the temperature measurement. In this experiment, the temperature data from the TFT was recorded with the temperature data from the thermocouples that were embedded in the copper cylinder to obtain the surface temperature value and the associated wall heat flux value simultaneously. To investigate the fluctuation pattern of the surface temperature during nucleate and film boiling, the temperature was recorded with the data acquisition system at five different sampling rates: i.e., 200, 400, 600, 800, and 1000 Hz. These data can be used to study the micro-scale features of the surface temperature fluctuation on a heated surface under pool boiling conditions.

C. Data Reduction

1. Heat Transfer on Nano-Structured Surface

The heat flux on the silicon surface was determined to be

$$q'' = -k\frac{\Delta T}{\Delta y} \tag{7.1}$$

where k is the thermal conductivity of the copper in [W/m · K], ΔT is the axial temperature gradient along the centerline of the copper cylinder in [K], and Δy is the axial distance between the thermocouples in [m].

In this study, the surface temperature on the silicon wafer was not measured directly, but was calculated using two correlations for the thermal resistance between the top of the silicon wafer and the top of the copper cylinder. The correlations were obtained from a supplemental experiment in which the surface temperature on the silicon wafer was measured with the thin film thermocouple (TFT) micro-fabricated in-situ on the top surface of the silicon wafer.

The correlation of the thermal resistance between the silicon wafer (at boiling side) and the top of the copper cylinder in the nucleate boiling regime was

$$R_{t,rd} = \frac{0.4685}{1 + \left(\frac{T_c}{60.56}\right)^{-6.808}} \tag{7.2}$$

where $R_{t,rd}$ is the thermal resistance between the silicon wafer and the top of the copper cylinder in [W/°C] and T_c is the temperature at the top surface of the copper cylinder obtained by extrapolating the temperatures from the wire-bead thermocouples embedded in the copper block in [°C]. The thermal resistance value used for the film boiling regime was

$$R_{t,rd} = 0.2146 + 2.522 \times 10^{-3} \cdot T_c \tag{7.3}$$

The details about the equations, i.e., Eqs. 7.2 and 7.3 will be discussed in the experimental results section.

The thermal resistance for the heat transfer measurement on the MWCNT surfaces was calculated with the correlation of

$$R_{t,rt} = R_{t,rd}\frac{A_{s,rd}}{A_{s,rt}} \tag{7.4}$$

where $A_{s,rd}$ and $A_{s,rt}$ are surface areas for a round silicon wafer and a rectangular silicon wafer in [m^2], respectively.

With these values, the surface temperature was calculated using Equation 7.5.

$$T_s = T_c - q'' \cdot A_{s,rt} \cdot R_{t,rt} \tag{7.5}$$

where T_c is the temperature at the top of the copper cylinder in [°C].

2. Surface Temperature Measurement Using TFT

The wall heat flux was evaluated from the gradient of the temperature profiles in the copper cylinder using Eq. 7.1.

The wall heat flux measured in close proximity to the CHF point was compared with a correlation suggested by Kutateladze [64] and Zuber [43] which is

$$q''_{max} = C_{max}h_{fg}[\sigma\rho_v^2(\rho_l - \rho_v)g]^{1/4} \tag{7.6}$$

where C_{max} is the experimental constant, h_{fg} is the latent heat in [kJ/kg], σ is the surface tension in [N/m] ρ_l is the liquid density in [kg/m^3], ρ_v is the vapor density in [kg/m^3], g is the gravitational acceleration in [m/s^2]. For this calculation, C_{max} is assumed to be 0.131.

The wall heat flux measured in close proximity to the MHF point was compared with a correlation, assuming film breaksdown occurs when the vapor generation rate becomes too low to sustain Taylor instability wave action on the interface, suggested by Zuber [65]:

$$q''_{min} = C_{min}\rho_v h_{fg}\left[\frac{\sigma g(\rho_l - \rho_v)}{\rho_l + \rho_v}\right]^{1/4} \tag{7.7}$$

where C_{min} is the experimental constant, assumed to be 0.09 for this calculation.

Overall thermal resistance between the boiling surface (silicon wafer) and the top surface of the copper cylinder was defined as:

$$R_{th} = \frac{\Delta T}{q'' A_s} \tag{7.8}$$

where ΔT is the temperature differential between the boiling surface and the top surface of the copper cylinder in [°C] and A_s is the surface area on which boiling occurs in [m^2].

D. Uncertainty Analysis

1. Heat Transfer on Nano-Structured Surface

The uncertainty of the wall heat flux data obtained from the experiments was obtained using:

$$\frac{\omega_{q''}}{q''} = \sqrt{\left(\frac{\omega_k}{k}\right)^2 + \left(\frac{\omega_{\Delta T}}{\Delta T}\right)^2 + \left(\frac{\omega_{\Delta y}}{\Delta y}\right)^2} \tag{7.9}$$

where ω is the statistical uncertainty value for each variable.

The uncertainty of the temperature on the silicon wafer surface could be caused by a number of sources:

1. Resolution of the data acquisition system was set by the 16 bit accuracy of the data acquisition hardware which is equivalent to an absolute error of 0.005 °C for the temperature range used in this study.

2. From the temperature measurements at room temperature it was observed that the standard deviation in measurement of the temperatures in the copper cylinder was approximately 0.03 °C .
3. The standard deviation (σ) of temperature fluctuations during steady state measurement of temperature during the experiments was observed to be 0.05 °C .

Hence the total uncertainty of the temperature measurement was estimated to be 0.055°C . Using the uncertainty values of ±1.0% for a thermal conductivity of copper and ±3.0% for the distance between two thermocouples embedded in the copper cylinder, the estimated maximum uncertainty of the wall heat flux was ±16.3% at the MHF point (in the case with a wall superheat of 50°C for saturated boiling on the silicon wafer with 9-μm tall MWCNT), with a typical uncertainty of ±6.7% at the CHF point (in the case with a wall superheat of 39°C for saturated boiling on the smooth silicon wafer surface).

With the estimated uncertainties of thermal resistance of ±6.6% and ±10.9% at the CHF and MHF points, respectively, the uncertainties of the surface temperature were estimated to be ±9.7% at the CHF point and ±5.9% at the MHF point.

2. Surface Temperature Measurement Using TFT

The uncertainty of the thermal resistance between the boiling surface and the top surface of the copper cylinder was calculated using:

$$\frac{\omega_{R_{th}}}{R_{th}} = \sqrt{\left(\frac{\omega_k}{k}\right)^2 + \left(\frac{\omega_{\Delta T_1}}{\Delta T_1}\right)^2 + \left(\frac{\omega_{\Delta T_2}}{\Delta T_2}\right)^2 + \left(\frac{\omega_{\Delta y}}{\Delta y}\right)^2 + \left(\frac{\omega_D}{D}\right)^2} \tag{7.10}$$

where ΔT_1 is the temperature differential between two thermocouples lying in the same vertical direction in [°C] and ΔT_2 is the temperature differential between the boiling surface and the top surface of the copper cylinder in [°C].

The uncertainty of the wall heat flux obtained from the experiments was obtained using:

$$\frac{\omega_{q''}}{q''} = \sqrt{\left(\frac{\omega_k}{k}\right)^2 + \left(\frac{\omega_{\Delta T_1}}{\Delta T_1}\right)^2 + \left(\frac{\omega_{\Delta y}}{\Delta y}\right)^2} \tag{7.11}$$

The estimated uncertainties in temperature differential inside the copper cylinder were ±4.9% and ±10.0% in proximity to the CHF (wall superheat=28.0°C) and MHF (wall superheat=59.7°C) points, respectively. For the TFT, the uncertainty values of the temperature measurement were estimated to be ±0.6% in the vicinity of the CHF point and ±0.2% near the MHF point.

The uncertainty in determination of the vertical distance between two thermocouples embedded in the copper block was estimated to be ±3.0%, which was determined by the machining accuracy of the holes and positioning accuracy of the thermocouple junction inside the holes. Using the uncertainty of ±1.0% for the thermal conductivity of the copper cylinder, the uncertainties of the heat flux were estimated to be ±5.8% in proximity to the CHF point (wall superheat=28.0°C) and ±10.5% in the vicinity of the MHF point (wall superheat=59.7°C). Based on the uncertainty value of ±1.5% for the diameter of the boiling surface, the uncertainty of the thermal resistance between the boiling surface and the top surface of the copper cylinder were calculated to be ±6.6% and ± 10.9% in the neighbor of the CHF and MHF points, respectively.

CHAPTER VIII

TWO-PHASE POOL BOILING WITH NANO-STRUCTURED SURFACES: EXPERIMENTAL RESULTS

A. Heat Transfer on Nano-Structured Surface

The heat transfer enhancement obtained by using the nano-structured surfaces was compared to the heat transfer data obtained from a smooth surface using a bare silicon wafer (this served as the control experiment). Saturated and sub-cooled experiments were performed to study the effect of liquid sub-cooling on the efficacy of the nano-structured surfaces in enhancing heat transfer.

1. Bare Silicon Wafer

Control experiments were performed using a bare silicon wafer. The control experiments provided an estimate for the heat transfer augmentation using MWCNT arrays. Boiling inception was obtained by increasing the power input to the cartridge heaters (three of 500 W and two of 300 W heaters). The liquid pool temperature was maintained at a sub-cooled temperature of 5°C or 10°C using the cooling unit submerged in the liquid during the experiment. To investigate the effect of sub-cooling on the wall heat flux, an additional experiment was conducted under saturated conditions where the liquid temperature was kept at its saturation temperature using the tubular heater in the viewing chamber. Figure 35 shows the experimental results for the boiling curve.

In nucleate boiling, the heat input to the test section was slightly increased as the liquid bulk temperature in the chamber was lowered; i.e., the liquid sub-cooling was increased due to convection effect under sub-cooled conditions. In this boiling regime, the sub-cooling effect on the wall heat flux increases as the wall superheat is increased. The heat input to the test section is increased significantly at the critical heat flux (CHF) due to the condensing effect of the rising bubble which makes it easier for the liquid to flow toward the heated surface as the liquid sub-cooling is increased. The CHF are obtained at wall superheats of 39°C, 40°C, and 40°C and the associated heat fluxes are 3.3×10^4 W/m^2, 3.7×10^4 W/m^2, and 4.1×10^4 W/m^2 under saturated, 5°C sub-cooled, and 10°C sub-cooled conditions, respectively. During the experiments, no incipience excursion was observed.

Inception of film boiling was obtained by decreasing the power input to the heaters immediately after a rapid increase in surface temperature was detected from the data acquisition system beyond the CHF points. In film boiling, however, the effect of sub-cooling on the wall heat flux at a given wall superheat is not found to be significant for the range of sub-cooling considered in this study - the increase in the wall heat flux, as the liquid sub-cooling is increased, is considered to be marginal heat enhancement. Since steady state conditions were difficult to obtain at the minimum heat flux (MHF), the experimental data were recorded in the vicinity of the MHF. From the experimental results, the MHF appears at a increasingly higher wall superheat as the sub-cooling is increased. The MHF are obtained at wall superheats of 58°C, 59°C, and 68°C and the associated wall heat fluxes are 1.3×10^4 W/m^2, 1.6×10^4 W/m^2, and 1.8×10^4 W/m^2 for saturated, 5°C sub-cooled, and 10°C sub-cooled conditions, respectively.

2. Experiments Using Type-A MWCNT Forests (9 μm Height)

Experiments for Type-A MWCNT (9 μm height) deposited on a silicon wafer were conducted to study the effect of shorter (less than the minimum vapor film thickness), vertically aligned carbon nanotubes on the wall heat flux. Figure 36 shows the pool

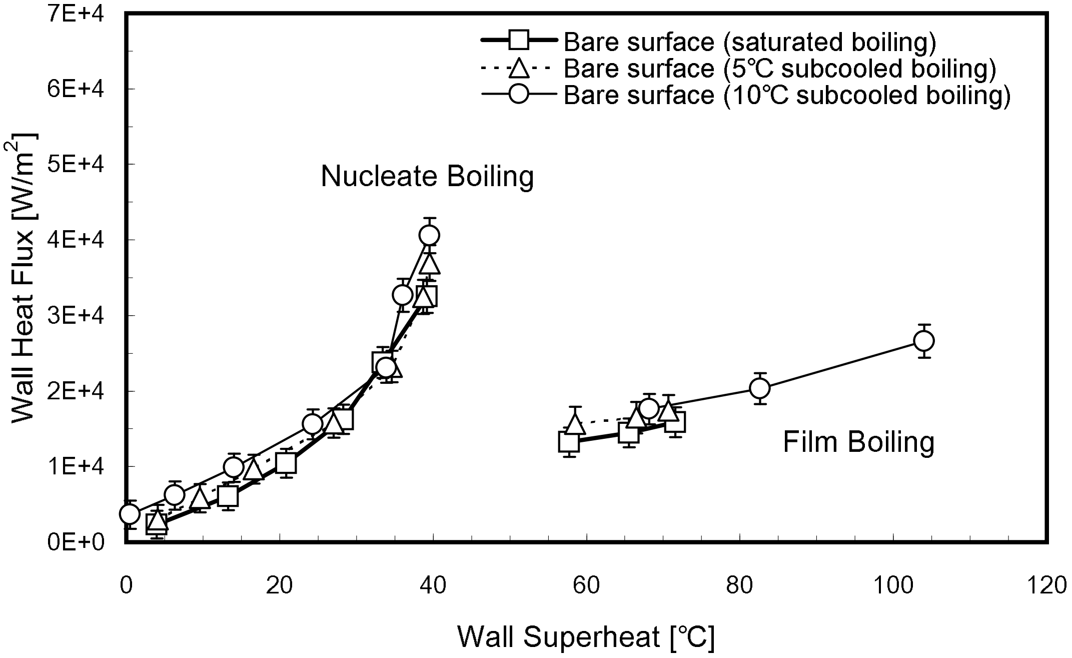

Fig. 35. Pool boiling curve for PF-5060 on bare silicon wafer (Saturation temperature of PF-5060 is 56°C).

boiling curve for Type-A MWCNT under saturated and sub-cooled (5°C and 10°C) conditions. In nucleate boiling, the wall heat fluxes are found to increase as the liquid sub-cooling is increased. However, the CHF point is not obtained at a higher wall superheat as the liquid sub-cooling is increased. For 10°C sub-cooling, as shown in the figure, the CHF point is achieved at a lower wall superheat than 5°C sub-cooled and saturated conditions. Prior to obtaining the CHF condition for the 10°C sub-cooling experiments, the heat exchanger unit could not support the required cooling load. Hence the data for the maximum heat flux shown in Fig. 36 for 10°C sub-cooling is expected to be lower than the CHF value. Under 5°C sub-cooling, the CHF is obtained at a wall superheat of 21°C and the associated wall heat flux is 5.3×10^4 W/m^2. This wall heat flux value is 44% higher than the corresponding CHF value for the bare silicon wafer (control experiment), as shown in the figure. For saturated conditions, the CHF point and the associated wall heat flux are 19°C and 4.9×10^4 W/m^2, respectively. This wall heat flux value is 50% higher than the corresponding CHF value for the bare silicon wafer. In nucleate boiling, Type-A MWCNT yield much higher wall heat flux values than the corresponding values for the bare silicon wafer at a given wall superheat. During the experiments, no incipience excursion was observed for all cases.

In film boiling, marginal enhancement in the wall heat flux values is observed as the liquid sub-cooling is increased. the MHF point is achieved at a higher wall superheat as the liquid sub-cooling is increased. A similar trend was observed for the bare silicon wafer (as discussed in the previous section). The wall heat flux level for Type-A MWCNT is slightly higher than or the same (within the bounds of experimental uncertainty) compared to the corresponding values for the bare silicon wafer. Under saturated and 10°C sub-cooled conditions, the wall heat fluxes for Type-A MWCNT are determined to be 1.7×10^4 W/m^2 and 1.8×10^4 W/m^2, respectively, at a given wall superheat of 70°C. This is ~11% higher than the corresponding values for the bare silicon wafer under the same liquid conditions. As shown in the figure, the MHF point for Type-A MWCNT is observed at a slightly lower wall superheat for saturated and sub-cooled conditions compared to the bare silicon wafer. However, this difference may not be significant if the marginal error for determining the MHF point is considered.

3. Experiments Using Type-B MWCNT Forests (25 μm Height)

Figure 37 shows the experimental results conducted with Type-B MWCNT array (25 μm height) deposited on a silicon wafer. These experiments were conducted to investigate the effect of taller (more than the minimum vapor film thickness), vertically aligned carbon nanotubes on the wall heat flux. As shown in the figure, it is observed that Type-B MWCNT yield higher boiling heat fluxes (compared to the bare silicon wafer) for a given wall superheat under saturated and sub-cooled (5°C and 10°C) conditions in nucleate boiling. For this type of MWCNT, a monotonic increase in the wall heat flux is observed at a given wall superheat, especially for the mid-range wall superheat region (12°C -17°C), as the liquid sub-cooling is increased. The presumed reason is probably because of heat transfer from the boiling surface to the liquid through the taller carbon nanotube structures which can act as "nano-fins." The free ends of the taller carbon nanotubes are thought to have high efficacy in removing heat from the surface to the liquid due to the increase in the temperature differential between the surface and the liquid as the liquid sub-cooling is increased. This trend was not observed for the shorter carbon nanotubes case (Type-A MWCNT discussed in the previous section). For Type-B MWCNT at 10°C liquid sub-cooling, the wall heat flux measurement in close proximity to the CHF point was obtained using a new heat exchanger unit which was able to support the cooling load. Under 10°C sub-

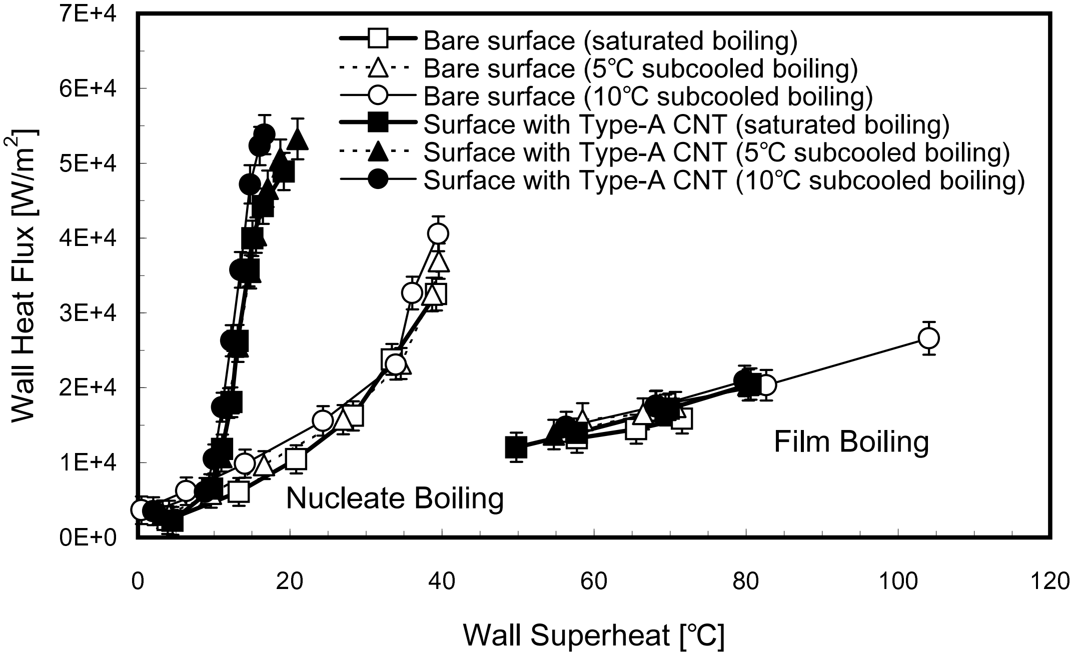

Fig. 36. Pool boiling curve for PF-5060 on MWCNT Type-A (9 μm height) synthesized on silicon wafer (Saturation temperature of PF-5060 = 56°C). Comparison of pool boiling curve of Type-A MWCNT with bare silicon wafer.

cooling, the wall heat flux at the CHF is 6.7×10^4 W/m^2 at a wall superheat of 22°C. The CHF under 5°C sub-cooled and saturated conditions are 6.0×10^4 W/m^2 and 5.5×10^4 W/m^2, respectively, and the associated wall superheats are 22°C and 20°C, respectively. The CHF values for Type-B MWCNT under saturated and 10°C sub-cooled conditions are 68% and 65% higher, respectively, than the corresponding values for the bare silicon wafer. At a given wall superheat of 17°C, under saturated and 10°C sub-cooled conditions, the wall heat fluxes for Type-B MWCNT are 300% and 380% higher, respectively, than the corresponding values for the bare silicon wafer. During the experiments, no incipience excursion was observed for all cases.

For Type-B MWCNT, the extent of the wall superheat for transition boiling region was much longer and more distinct than the bare silicon wafer (and Type-A MWCNT). During transition boiling, a portion of the boiling surface under film boiling conditions was localized near the outer edge of the surface (around the steel clamp). The other portion of the boiling surface under nucleate boiling conditions was localized near the center of the surface. After obtaining a steady state wall superheat of 73°C under a saturated boiling condition, a continuous vapor film was observed over the whole area of the exposed surface. The vapor film was identifiable since it manifested a shiny mirror type of surface which could be clearly observed in the experiments.

In film boiling, at a given wall superheat of 70°C, the wall heat fluxes obtained for Type-B MWCNT are 2.5×10^4 W/m^2, 2.9×10^4 W/m^2, and 3.2×10^4 W/m^2 under saturated, 5°C sub-cooled, and 10°C sub-cooled conditions, respectively, which are 60%, 67%, and 81% higher values, respectively, than the corresponding values for the bare silicon wafer. As the liquid sub-cooling is increased, the MHF point is observed at a higher wall superheat. This is consistent with similar observations for the bare silicon wafer (and Type-A MWCNT). The MHF points for Type-B MWCNT are 58°C, 68°C, and 73°C under saturated, 5°C sub-cooled, and 10°C sub-cooled conditions, respectively. These wall superheat values are much higher than the corresponding values obtained for the bare silicon wafer (The MHF points were observed at wall superheats of 58°C, 59°C, and 68°C under saturated, 5°C sub-cooled, and 10°C sub-cooled conditions, respectively).

4. Type-A, Type-B MWCNT Forests and Bare Silicon

The effect of Type-A MWCNT array on the wall heat flux was compared with that for Type-B MWCNT array in Fig. 38. In nucleate boiling, under saturated conditions, the wall heat fluxes for Type-A MWCNT are higher than the corresponding values for Type-B MWCNT at the mid-range wall superheat region. This trend, however, reverses as the liquid cooling is increased. Under 10°C sub-cooled conditions, the wall heat fluxes for Type-B MWCNT are slightly higher than the corresponding values for Type-A MWCNT. Comparing the two results prompts one to consider the possible reason for this trend which is probably because of heat transfer from the boiling surface to the liquid through the carbon nanotubes vertically aligned. Under saturated conditions, both the shorter and taller carbon nanotubes (Type-A and Type-B MWCNT) probably disrupt the micro-layer under bubbles. Due to their morphology and the size of active nucleation site, the nucleation for Type-A MWCNT is probably higher than for Type-B MWCNT. However, the heat transfer effect, through the carbon nanotube structures, on the wall heat flux becomes more dominant as the liquid sub-cooling is increased. The decrease in the liquid temperature, for more sub-cooling, results in the increase in the temperature differential between the boiling surface and the liquid.

In nucleate boiling, the wall heat fluxes for Type-B MWCNT, at the higher wall superheat region (17°C), are slightly superior to the corresponding values for Type-A

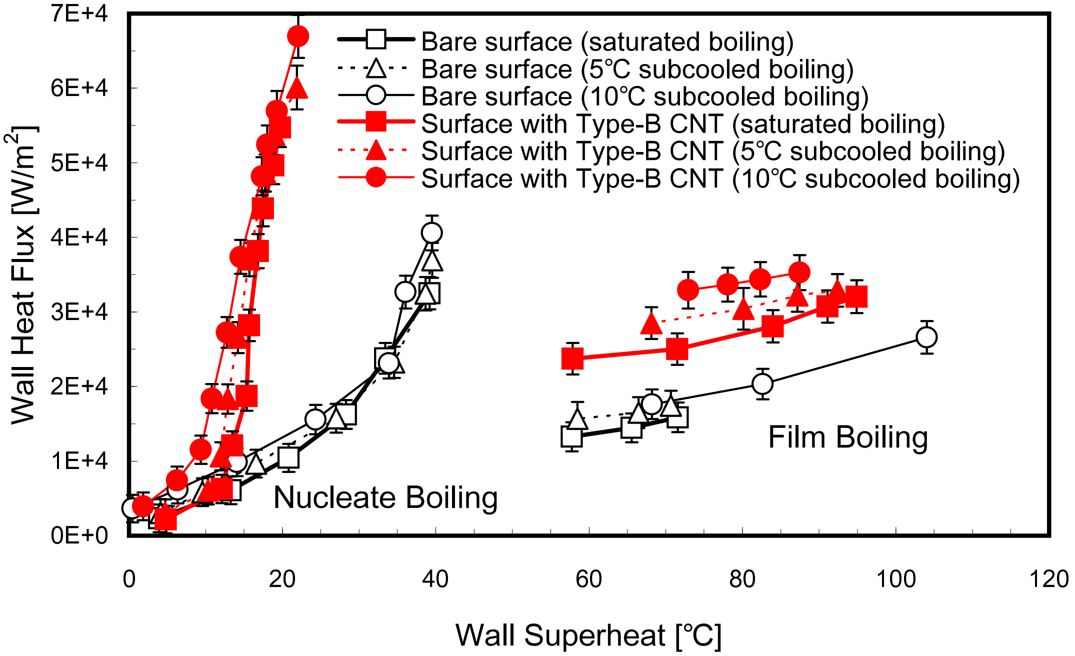

Fig. 37. Pool boiling curve for PF-5060 on MWCNT, Type-B (25 μm height) synthesized on silicon wafer (Saturation temperature of PF-5060 = 56°C). Comparison of pool boiling curve for Type-B MWCNT with bare silicon wafer.

MWCNT regardless of the degree of the liquid sub-cooling. This trend is consistent with the one discussed for investigating the sub-cooling effect on the wall heat flux for Type-B MWCNT in the previous section; The effect of the heat transfer through the carbon nanotube structures on the wall heat flux becomes more dominant as the temperature differential between the boiling surface and the liquid is increased. The temperature differential becomes larger as the wall superheat is increased because the temperature of the liquid stayed constant during the experiments. The taller carbon nanotubes (Type-B MWCNT) have more efficacy in transferring heat from the boiling surface to the liquid than the shorter carbon nanotubes (Type-A MWCNT). Based on the saturation and 5°C sub-cooling experiments, it can be concluded that the CHF values for Type-B MWCNT beyond the wall superheat of 17°C are slightly higher than the corresponding values for Type-A MWCNT. Type-B MWCNT have 12% and 13% higher CHF values under saturated and 5°C sub-cooled conditions, respectively, than Type-A MWCNT. The associated wall superheat values for Type-B MWCNT are also slightly higher than the corresponding values for Type-A MWCNT under both saturated and 5°C sub-cooled conditions. Under 10°C sub-cooled conditions, the wall heat flux value at the CHF point for Type-B MWCNT is much higher than the corresponding value for Type-A MWCNT. However, the direct comparison between the two values is restrained because the experiment with Type-A MWCNT could not attain the CHF point as discussed in the previous section.

In the film boiling regime, the wall heat flux values for Type-B MWCNT are much higher than the corresponding values for Type-A MWCNT at a given wall superheat. At a given wall superheat of 70°C, the wall heat fluxes for Type-B MWCNT are 2.5×10^4 W/m^2 and 3.2×10^4 W/m^2 under saturated and 10°C sub-cooled conditions, respectively, which are 45% and 80% higher values, respectively, than the corresponding values for Type-A MWCNT. As shown in the figure, the effect of sub-cooling on the wall heat flux for Type-B MWCNT is much more significant than Type-A MWCNT. The main reason for this is thought to be the heat transfer through the carbon nanotube structures as shown in Fig. 39. The heights of the carbon nanotubes used in this study were 9 μm for Type-A MWCNT and 25 μm for Type-B MWCNT. As will be discussed in the next section in more detail, the height of Type-B carbon nanotubes is greater than the dynamic value of the minimum vapor film thickness which enables enhanced liquid-solid contacts during film boiling. Under this condition, the heat can be transferred from the boiling surface to the liquid through the carbon nanotube structures. With this heat transfer mechanism, Type-B MWCNT enhances the wall heat flux in film boiling under saturated conditions. As the liquid sub-cooling is increased, the temperature differential between the boiling surface and the liquid becomes larger, which results in better efficacy in enhancing heat transfer from the surface to the liquid through carbon nanotube structures. This can explain why the wall heat flux for Type-B MWCNT is highly dependent on the degree of the liquid sub-cooling. In contrast, the height of Type-A MWCNT is shorter than the dynamic value of the minimum vapor film thickness. Hence this type of carbon nanotubes (shorter than the minimum vapor film thickness) cannot support the boiling surface to touch the liquid through the carbon nanotubes. As a result, for Type-A MWCNT, no wall heat flux enhancement is attained even though the liquid sub-cooling is increased in the film boiling regime.

The effect of the MWCNT arrays (Type-A and Type-B) on pool boiling was also compared with that of the bare silicon wafer in Fig. 38. In nucleate boiling, both Type-A and Type-B MWCNT arrays have higher wall heat flux values than the corresponding values for the bare silicon wafer under saturated and sub-cooled conditions (5°C and 10°C). For example, at a given wall superheat of 13°C and under 10°C liquid sub-cooled condition, Type-A and Type-B MWCNT arrays have higher nucleate boiling heat fluxes by 242% and 205% than the bare silicon wafer. The wall heat flux values at the CHF points for Type-A and Type-B MWCNT arrays are higher than the corresponding values for the bare silicon wafer under all of the liquid conditions. However, the associated wall superheats at the CHF points for Type-A and Type-B MWCNT arrays are much lower than those for the bare silicon wafer.

For the film boiling experiments under saturated and sub-cooled (5°C and 10°C) conditions, the wall heat fluxes for Type-B MWCNT are much higher than the corresponding values for Type-A MWCNT and the bare silicon wafer. The taller MWCNT (Type-B MWCNT) structures enhance the wall heat flux at a given wall superheat and cause the MHF point to be attained at a higher wall superheat by disrupting the vapor film at the points of the minimum vapor film thickness that may lead to possible collapse of film boiling. Within the bounds of the experimental error - the wall heat fluxes are almost identical for a given wall superheat for Type-A MWCNT and the bare silicon wafer in the film boiling regime.

The wall heat fluxes in the vicinity of the CHF and MHF points are summarized in Table IX (Appendix D).

5. Bubble and Boiling Surface Images

The bubbles on the bare silicon wafer, Type-A, and Type-B MWCNT arrays are shown in Figs. 40, 41, and 42. The images were captured during the experiments in proximity to the CHF and MHF points using Sony CyberShot DSC-P10 Digital Camera under saturated and sub-cooled (5°C and 10°C) conditions. As shown in the figures in the vicinity of the CHF points, the degree of the liquid sub-cooling strongly influences the shape of the bubble departing from the boiling surface. Under 10°C sub-cooling, no bubble columns are observed in the vicinity of the CHF point, probably because of the condensation effect of the sub-cooled liquid on the departing

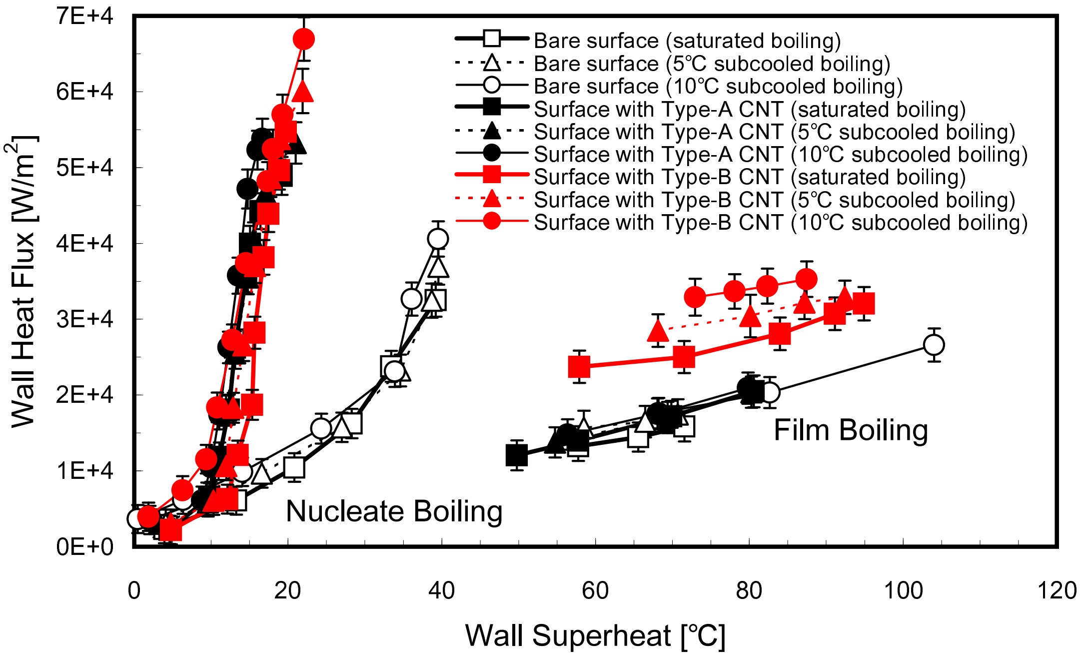

Fig. 38. Comparison of pool boiling curve for PF-5060 on MWCNT, Type-A (9 μm height) and Type-B (25 μm height) synthesized on silicon wafers with a bare silicon wafer (Saturation temperature of PF-5060 =56°C).

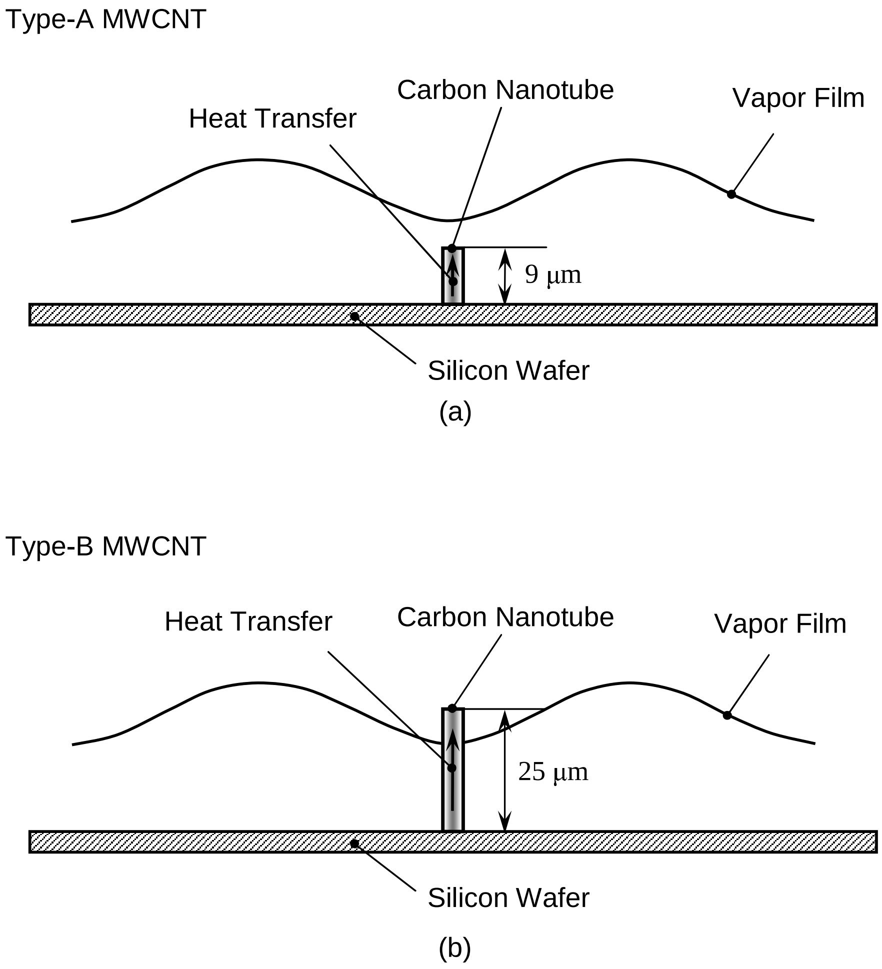

Fig. 39. Schematic of heat transfer mechanism through carbon nanotubes for Type-A and Type-B MWCNT in film boiling.

bubbles. In contrast, bubble columns are noticeable for saturated conditions as shown in Figs. 40(a), 41(a), and 42(a). Relatively weak bubble columns are observed in 5°C sub-cooled conditions. By comparing the bubble images taken under saturated conditions, it can be seen that Type-A and Type-B MWCNT arrays display much more ebullient motion of the bubble columns, after they depart from the boiling surface, than the bare silicon wafer. However, the difference between the two carbon nanotubes (Type-A and Type-B MWCNT) and the bare silicon wafer decreases as the liquid sub-cooling is increased.

The degree of the liquid sub-cooling strongly affects the shape of the bubble departing from the surface in the vicinity of the MHF point as it does in proximity to the CHF point. As the liquid sub-cooling is increased, the amount of vapor bubble released and the size of the bubble departing from the surface decrease. For the images taken in the vicinity of the MHF point under saturated conditions, a thin film is clearly observed on the top of the bare silicon wafer and Type-A MWCNT in the form of a shiny mirror type surface. However, a thin film for Type-B MWCNT is not clearly displayed in Fig. 42(b) because the MHF point for Type-B MWCNT appears at a higher wall superheat than Type-A MWCNT and the bare silicon wafer. According to the direct observation of Type-B MWCNT through the viewing window during the experiment, however, a shiny mirror type surface was observed in the vicinity of the MHF point. For the images taken under sub-cooled conditions, a shiny mirror type surface is clearly observed in proximity to the MHF point regardless of the degree of the liquid sub-cooling (5°C and 10°C).

Figure 43 shows SEM images for the top view of Type-B MWCNT array before and after the boiling experiments, respectively. The SEM image in Fig. 43(a) was obtained before the boiling experiments and shows a network of the thread-like MWCNT structures on the top surface. Figure 43(b) was obtained after the boiling experiments with a higher magnification and shows that the surface morphology of the MWCNT structures was not altered significantly during the boiling experiments. This demonstrates that the bonding strength of the MWCNT structures on the silicon wafer substrate is able to withstand the boiling experiments.

6. Discussion

The effect of the MWCNT on pool boiling can be attributed to two main factors:

1. The higher effective wall thermal conductivity due to the presence of the MWCNT (which can enhance the surface thermal instabilities, e.g., spatial size of the surface temperature fluctuations or “cold spots”); and
2. The height of the stiff “hair-like” MWCNT vertical protrusions (which can disrupt the hydrodynamic instabilities, e.g., by disrupting the micro-layer region in nucleate boiling and the “continuous” vapor film in film boiling).

The experimental results are consistent with numerical models reported in the literature. Previous numerical and experimental results by Banerjee and Dhir [4, 5] and Banerjee et al. [6] showed that the dynamic value of the minimum vapor film thickness for film boiling of PF-5060 was approximately 15-20 μm. The authors discussed that surface roughness (or for example artificially engineered surface micro/nano-structures) greater than 10 μm could disrupt the vapor films at the points of minimum vapor film thickness leading to possible collapse of film boiling.

Comparing the results of Type-A and Type-B MWCNT forests - it is observed that for Type-B (25 μm height) the film boiling is enhanced considerably more than for Type-A (9 μm height). This indicates that an MWCNT forest with heights greater than 10 μm possibly disrupts the vapor film. Therefore MWCNT forests with heights greater than 10 μm have better efficacy in enhancing heat transfer in film boiling.

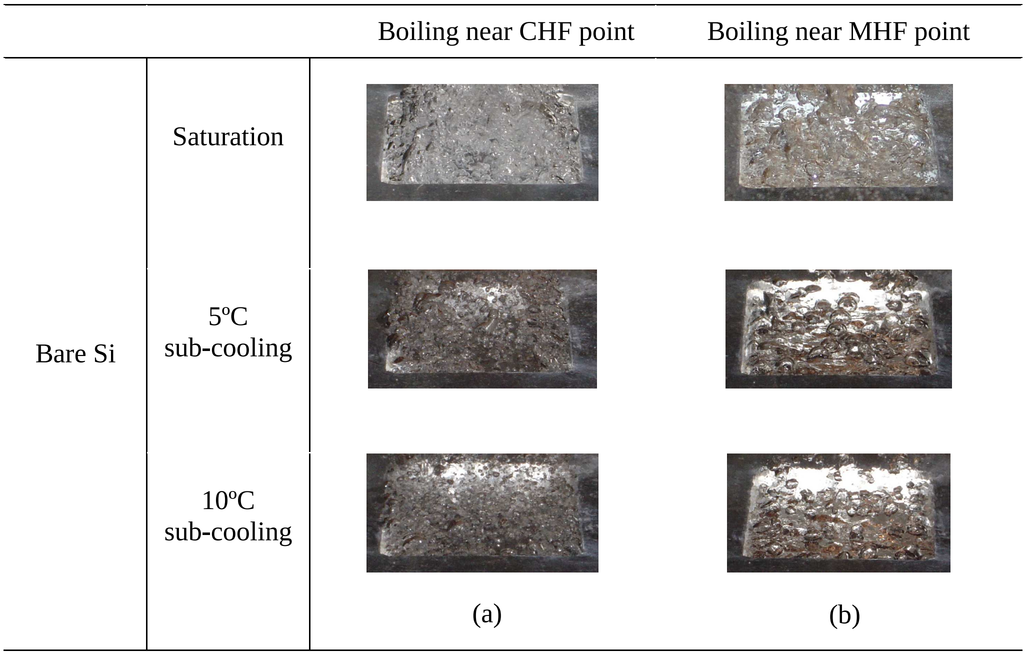

Fig. 40. Boiling of PF-5060 on bare silicon wafer during the experiments: (a) near CHF point (b) near MHF point.

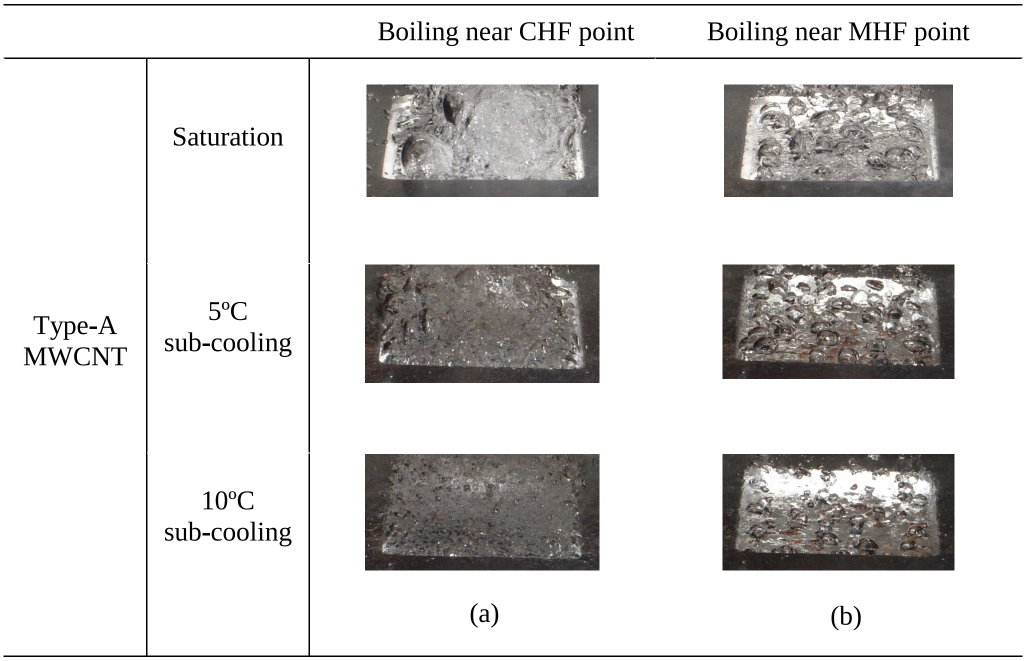

Fig. 41. Boiling of PF-5060 on Type-A MWCNT surface during the experiments: (a) near CHF point (b) near MHF point.

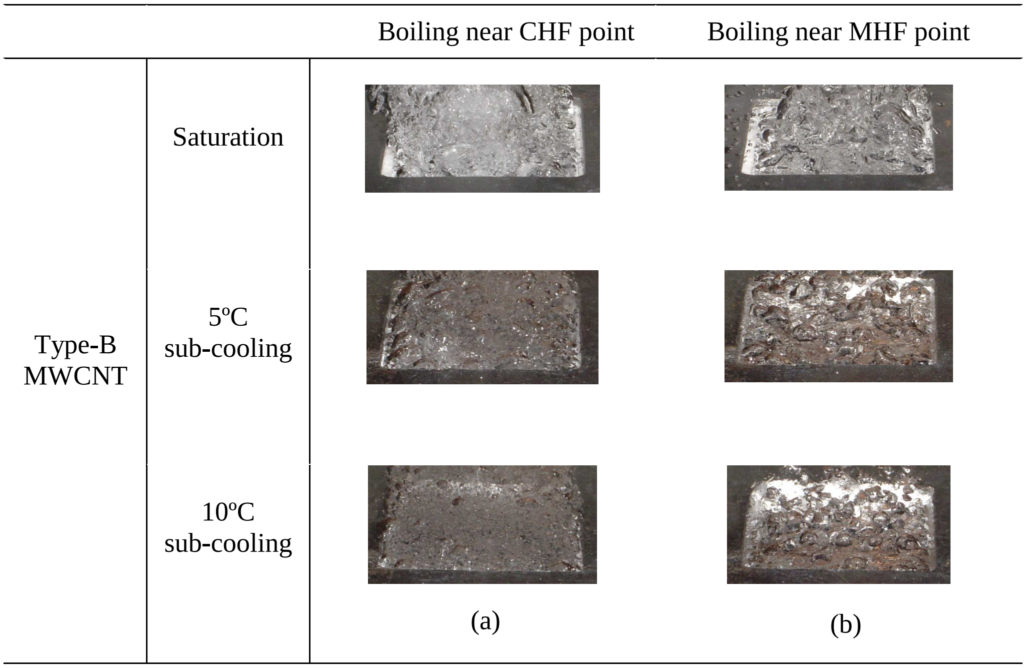

Fig. 42. Boiling of PF-5060 on Type-B MWCNT surface during the experiments: (a) near CHF point (b) near MHF point.

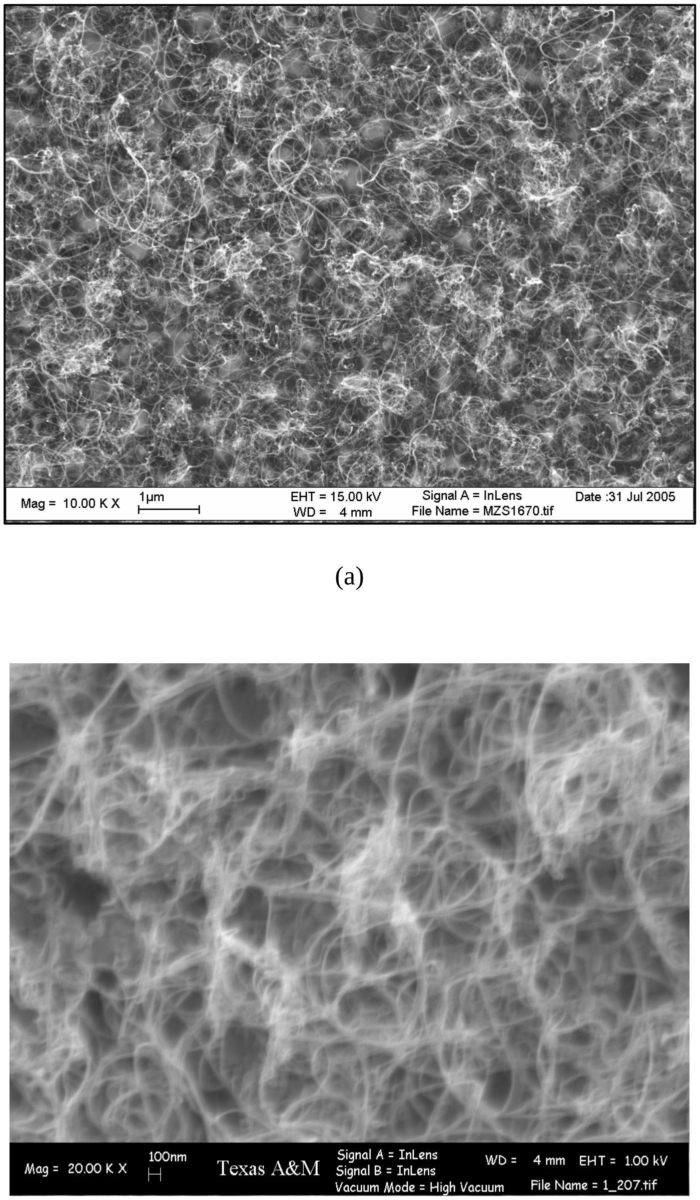

(a)

(b)

Fig. 43. SEM image showing top view of Type-B (25 μm height) MWCNT array, (a) before (Source: Dr. R. H. Baughman et al. at the Nanotech Institute, University of Texas at Dallas); and (b) after the pool boiling experiments.

The effect of sub-cooling on heat flux enhancement is therefore more pronounced for Type-B MWCNT than for Type-A MWCNT.

The study of Banerjee et al. [6] also demonstrated the existence of cold spots in film boiling. Cold spots are regions that have lower surface temperature than the surrounding areas. The study by Banerjee et al. [6] showed that cold spots served as focused conduits for heat transfer in film boiling. The location of the cold spots coincided with the location of the minimum vapor film thickness (showing that these are coupled thermal-hydrodynamic phenomena). The width of the cold spots was found to be a function of the wall thermal conductivity (or more specifically the thermal diffusivity of the wall material). It is expected that similar cold spot regions would develop during nucleate boiling in the micro-layer region on the wall at the location of the liquid-vapor interface. By analogy, it would be expected that the size (or width) of the cold spots would be dictated by the wall thermo-physical properties.

Since MWCNT structures have higher thermal conductivity than the silicon substrate - the size of the cold spots is bigger for the surfaces coated with the MWCNT than for the bare silicon wafer. Hence the efficacy of the cold spots in transferring heat is enhanced due to the presence of the MWCNT structures. The MWCNT structures that disrupt the vapor film at the minimum vapor film thickness (or location of the cold spots) would disrupt the conduits for heat transfer, would enhance the liquid-solid contacts and cause transient quenching of the heated surface with further augmentation of heat transfer in film boiling. Hence, Type-B MWCNT forests cause heat transfer augmentation in film boiling while heat transfer augmentation is not observed during the film boiling experiments for Type-A MWCNT forests. Numerical studies reported by Banerjee and Dhir [4, 5] showed that for 10°C sub-cooling the minimum vapor film thickness was greater than 10 μm. Hence higher sub-cooling is needed for Type-A MWCNT to disrupt the vapor film during film boiling and thereby demonstrate higher heat flux enhancement with the increase in sub-cooling.

Hence for heat transfer augmentation schemes using the MWCNT forests, in the film boiling region (and at the MHF point), the height of the MWCNT forests is critical to the efficacy of the augmentation schemes. For heat transfer augmentation schemes using MWCNT forests, in the nucleate boiling regime (and probably at the CHF), the size of nucleation sites is the limiting design parameter.

In contrast, there is low sensitivity to heat transfer augmentation to the height of the MWCNT forests in nucleate boiling. This is because in nucleate boiling and the CHF the size and distribution of the nucleation sites is expected to be the limiting variable rather than the height of the surface structures. The heights of the MWCNT in these experiments are greater than the size of the micro-layer. Therefore, both types of the MWCNT provide similar heat flux enhancement at comparable wall superheat values.

Increasing the height of the MWCNT from 9 μm to 25 μm (and compared to a bare silicon wafer) is found to slightly extend the wall superheat required for the CHF to occur. A potential mechanism for delaying the occurrence of the CHF to higher superheats can be through the suppression of “mushroom” type of bubbles or enhanced formation of vapor stems that trap superheated liquids at the CHF (e.g., Gaertner [66]). This can occur due to the hair-like protrusion of the MWCNT into the mushroom type bubble or through the formation of additional vapor stems due to the presence of the MWCNT on the surface. Additional investigations are needed to conclusively verify the mechanisms responsible for extending the wall superheat required for the CHF for boiling on the nano-structured surfaces and to understand the effect of the height of the nanostructures on the CHF.

B. Surface Temperature Measurement Using TFT

An experiment was performed under saturated conditions to measure the surface temperature and obtain the overall thermal resistance correlation between the boiling surface (silicon wafer) and the top surface of the copper cylinder.

1. Characteristics of Thin Film Thermocouple (TFT)

a. Response of TFT

A TFT junction used in this experiment had a very small mass (of the order of 10^{-11} kg) compared with a wire-bead thermocouple. This enabled a faster thermal response and a low characteristic time constant for the TFT of the order of 10^{-8} s. The presence of the TFT was expected to have minimal effect on the surface temperature distribution on the boiling surface due to the small footprint and lower thermal inertia of the TFT. The calculated values of the characteristic length, thermal diffusivity, and characteristic time of the micro-machined thermocouple are summarized in Table II.

Due to the extremely low time constant of the TFT, the temporal resolution of measurements was limited by the capability of the data acquisition system. This was also observed by Debey et al. [67].

Table II. Calculated properties of micro-machined thermocouple.

	Unit	Calculated Value
Characteristic Length	m	4.42×10^{-7}
Thermal Diffusivity	m^2/s	2.31×10^{-5}
Characteristic Time	s	8.44×10^{-9}

b. Calibration of TFT

Before boiling experiments were conducted, the calibration of the TFT was performed under steady state conditions. The calibration curve of the TFT is shown in Fig. 44. As shown in the figure, the calibration plot of the TFT has a linear response when compared with the response from the wire-bead K-type thermocouple attached to the surface of the silicon wafer for this calibration. The slope of the calibration line is 0.99 which means the temperature response of the fabricated TFT used in this study is nearly the same as the standard wire-bead thermocouple. Prior to this calibration, the wire-bead K-type thermocouple was calibrated against a NIST calibrated mercury thermometer.

2. Pool Boiling Curve

a. Wall Heat Flux

A pool boiling experiment on the bare silicon wafer with the TFT on top was performed under saturated conditions. Fig. 45 shows the pool boiling curve (wall heat flux vs. wall superheat) obtained by using the experimental apparatus for pool boiling of PF-5060 on a horizontal flat silicon wafer surface. As shown in the figure, the wall heat flux increases with the increase in the wall superheat in nucleate boiling. The wall heat flux which was measured in close proximity to the CHF point is 4.18×10^4 W/m^2 and the associated wall superheat is 28°C. As a reference, a supplementary boiling experiment on a horizontal, flat copper surface was conducted. For this experiment, the silion wafer and the pyrex wafer were removed from the test section (heater apparatus) and then the top surface of the copper cylinder was polished with a fine grit (1200 grit) sandpaper and cleaned with acetone prior to the test run. In this experiment, the surface temperature was calculated by extrapolating tempera-

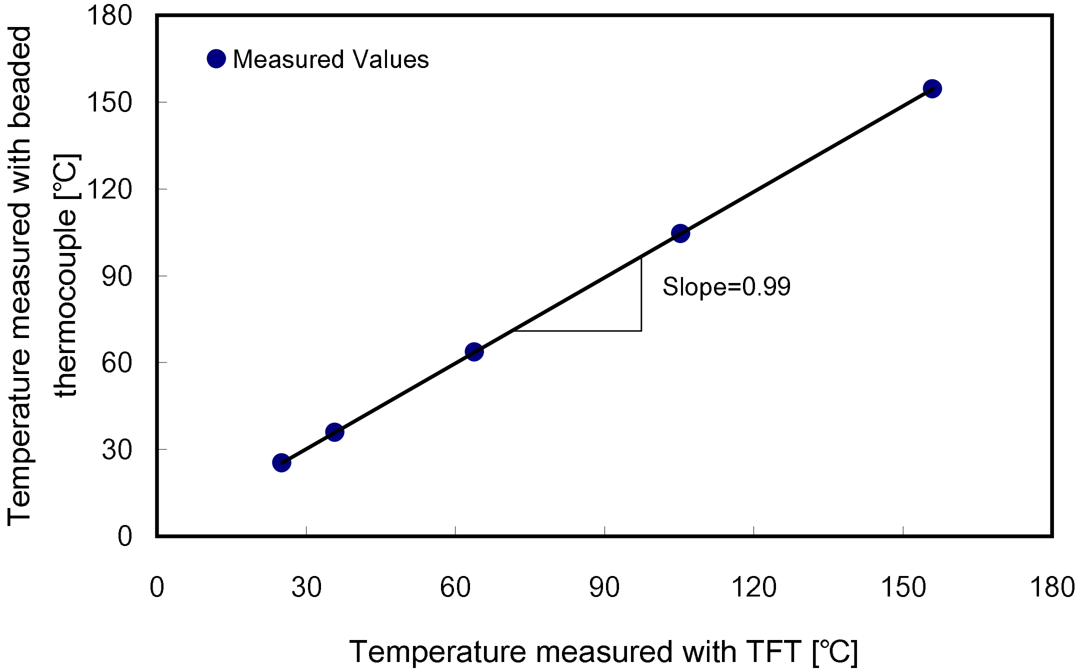

Fig. 44. Calibration curve for a surface micro-machined Thin Film Thermocouple (TFT).

tures measured from the thermocouples that were embedded in the copper cylinder in a vertical direction. Figure 46 shows the experimental results. At a given wall superheat, the wall heat fluxes for the copper surface are much higher than the corresponding values for the silicon wafer surface. The presumed reason for this difference can be summarized as follows:

- Material: the thermophysical properties of copper is different from those of silicon. From the thermo-physical property table, copper has almost a three times higher thermal conductivity value than silicon.
- Surface finish: surface roughness influences the boiling performance. A rough surface provokes more bubble nucleation compared to a smooth surface because of the presence of trapped gas in narrow crevices in the solid surface.

For boiling on the copper surface, the wall heat flux in the vicinity of the CHF point is 1.23×10^5 W/m^2 and the associated wall superheat is 20°C . To validate the data measured from the boiling experiment on the copper surface, this wall heat flux was compared with the value calculated using the correlation proposed by Kutateladze [64] and Zuber [43]. In this calculation, 0.131 was used as C_{max} in Eq. 7.6 that was reported in Zuber's original model. Using this assumed constant, the maximum heat flux value calculated using the correlation is 1.33×10^5 W/m^2. This wall heat flux is 7.5% higher than the corresponding wall heat flux measured for the copper surface. Hence, it can be concluded that the measured value using the experimental set-up built for this boiling experiment is reliable and consistent with the calculated value.

Inception of film boiling was obtained by decreasing the power input to the heaters just after a rapid increase in the surface temperature was detected from the data acquisition system beyond the CHF point. In film boiling, the wall heat flux values were measured by reducing the power input to the heaters. As shown in Fig.

45, the wall heat flux lowered as the wall superheat is decreased. The measured point in proximity to the MHF point is determined at a wall superheat of 59.7°C and the associated wall heat flux is 1.97×10^4 W/m^2. As a reference, this value was also compared with the corresponding value that was measured from the boiling experiment on the copper surface. Figure 46 shows the experimental results. At a given wall superheat, the wall heat fluxes for the silicon wafer surface are slightly higher than the corresponding values for the copper surface. The first presumed reason for this difference is the radiation effect caused by the material property and surface finish. According to Carey [68], the radiation contribution probably depends on the nature of the solid surface. The second reason is probably heat loss through the thermocouple wires bonded to the silicon wafer, caused by the temperature differential between the surface and the test liquid. However, this wall superheat difference between the two surfaces may not be significant if the experimental uncertainties are considered in this analysis. In proximity to the MHF point, the estimated uncertainty of the wall heat flux measurement was ±17.0%.

For the boiling on the copper surface, the wall heat flux in the neighbor of the MHF point is 9.57×10^3 W/m^2 and the associated wall superheat is 50.8°C . Comparing the wall heat flux values and the associated wall superheat for the two different surfaces in proximity to the MHF point, it appears that the wall heat flux and the associated wall superheat for the silicon wafer surface are higher than the corresponding values for the copper surface, which results in the wall heat flux for the silicon wafer surface in the vicinity of the MHF point to be higher than the corresponding value for the copper surface. To validate the data measured from the boiling experiment on the copper surface, this wall heat flux value was compared with the one calculated using the correlation proposed by Zuber [65]. By using Eq. 7.7, the minimum heat flux value is calculated to be 8.07×10^3 W/m^2, which is consistent with the measured wall heat flux for the copper surface in proximity to the MHF point.

b. Surface Temperature

Figures 47 and 48 show surface temperature fluctuation measured, at a sampling rate of 1000Hz, using the TFT under nucleate boiling conditions. In each figure, 3-second-long temperature data is presented for the convenience of comparison. At each measurement point, the temperature was recorded for 3 minutes to obtain the average surface temperature and perform the data analysis. Figure 47(a) shows the temperature fluctuation at a wall superheat of 19.0°C. In the figure, the high frequency components of the temperature fluctuation, that are generally related with the bubble formation on the heated surface and the bubble departure from the surface, are detected with respect to time. However, the low frequency components of the temperature fluctuation, characterized by large amplitude and slow fluctuation, are not shown at this wall superheat. At a wall superheat of 23.6°C, as shown in Fig. 47(b), the high and low frequency components of the temperature fluctuation have a tendency not much different from the one obtained at a wall superheat of 19.0°C. As the surface temperature goes up, however, the low frequency components of the temperature fluctuation become more important probably caused by the increase in the bubble movement on the heated surface. Figure 48(a) shows the surface temperature fluctuation measured at a wall superheat of 26.3°C . The low frequency components of the temperature fluctuation appear more frequently than the previous two results shown in Figs. 47 and 48. In the vicinity of the CHF point, the temperature fluctuation measured at a wall superheat of 28.0°C has more low frequency components. A number of peaks with low frequency fluctuation can be observed from the temperature data even though the low frequency components do not appear on

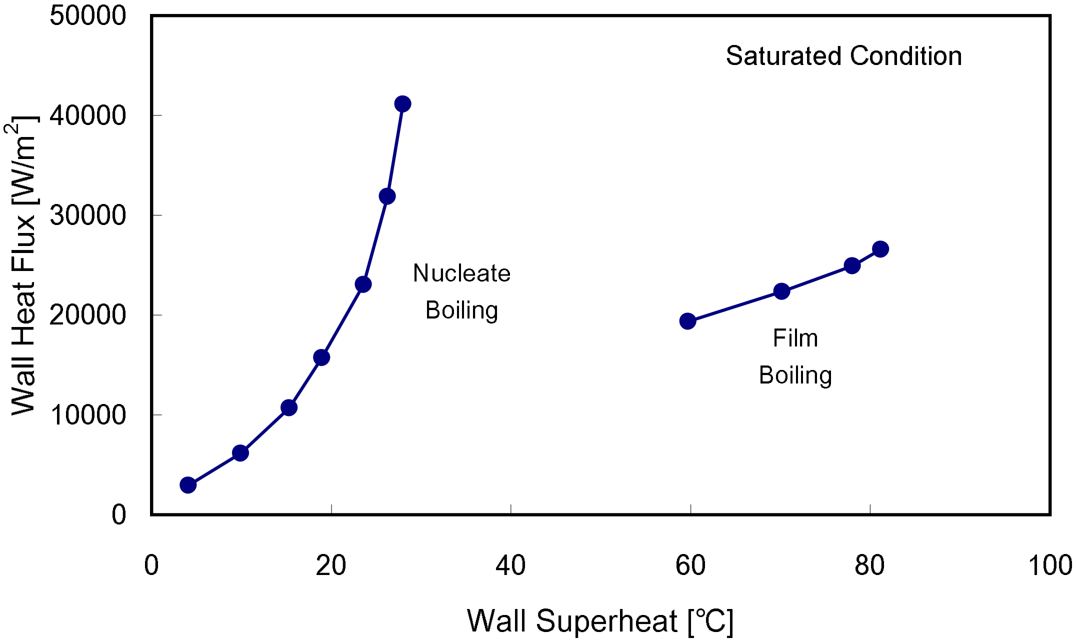

Fig. 45. Pool boiling curve for PF-5060 obtained using the experimental apparatus (Saturation temperature=56°C of PF-5060).

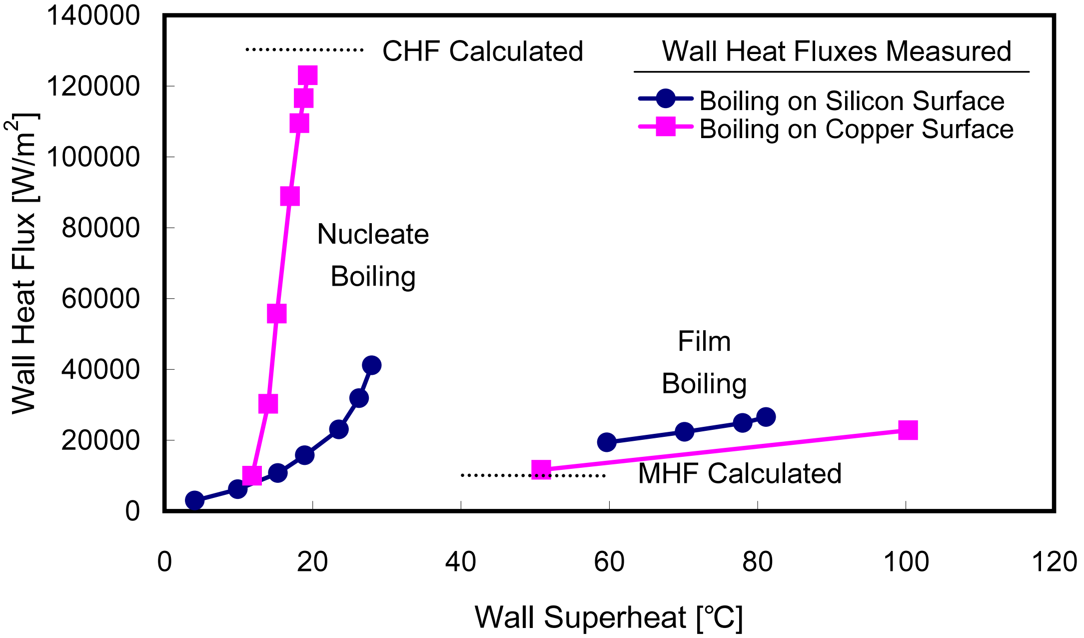

Fig. 46. Comparison of pool boiling curve for PF-5060 on a silicone wafer with that on a copper cylinder (Saturation temperature=56°C of PF-5060).

a regular basis.

Figures 49 and 50 show the surface temperature fluctuation measured, at a sampling rate of 1000Hz, using the TFT under film boiling conditions. In this boiling regime, different patterns are observed for the temperature fluctuations measured under nucleate boiling conditions. Fig. 49(a) shows the temperature fluctuation measured at a wall superheat of 59.7°C in the vicinity of the MHF point. In this figure, the mid-range frequency components of temperature fluctuation, ranging from approximately 6Hz to 10Hz, are observed. The existence of these frequency components in the temperature fluctuation in this boiling regime perhaps indicates that fast vapor bubble flows may subsist on the boiling surface. This movement with the mid-range frequency components, however, is not shown on a regular basis. The temperature fluctuation measured at a wall superheat of 70.2°C is displayed in Fig. 49(b). The temperature fluctuation pattern is practically consistent with the one measured at a wall superheat of 59.7°C. As the wall superheat is increased, the temperature fluctuation with mid-range frequency gradually becomes violent. Figure 50(a) shows the temperature fluctuation measured at a wall superheat of 78.0°C. Comparing Figs. 50(a) and 49(b), the difference between the two temperature fluctuation patterns is not great except for the variance level of the peak amplitude of the fluctuation. The variance of the peaks measured at a wall superheat of 78.0°C is larger than that measured at a lower wall superheat. This pattern is consistent as the wall superheat is increased. For the temperature fluctuation measured at a wall superheat of 81.2°C, the variance of the peaks of the temperature fluctuation is larger than that measured at a wall superheat of 78.0°C .

Figure 51 shows the variations in the average surface temperature as the wall superheat is increased. Instead of the wall superheat, however, the average top surface temperature of the copper cylinder was selected as the abscissa of this figure to study

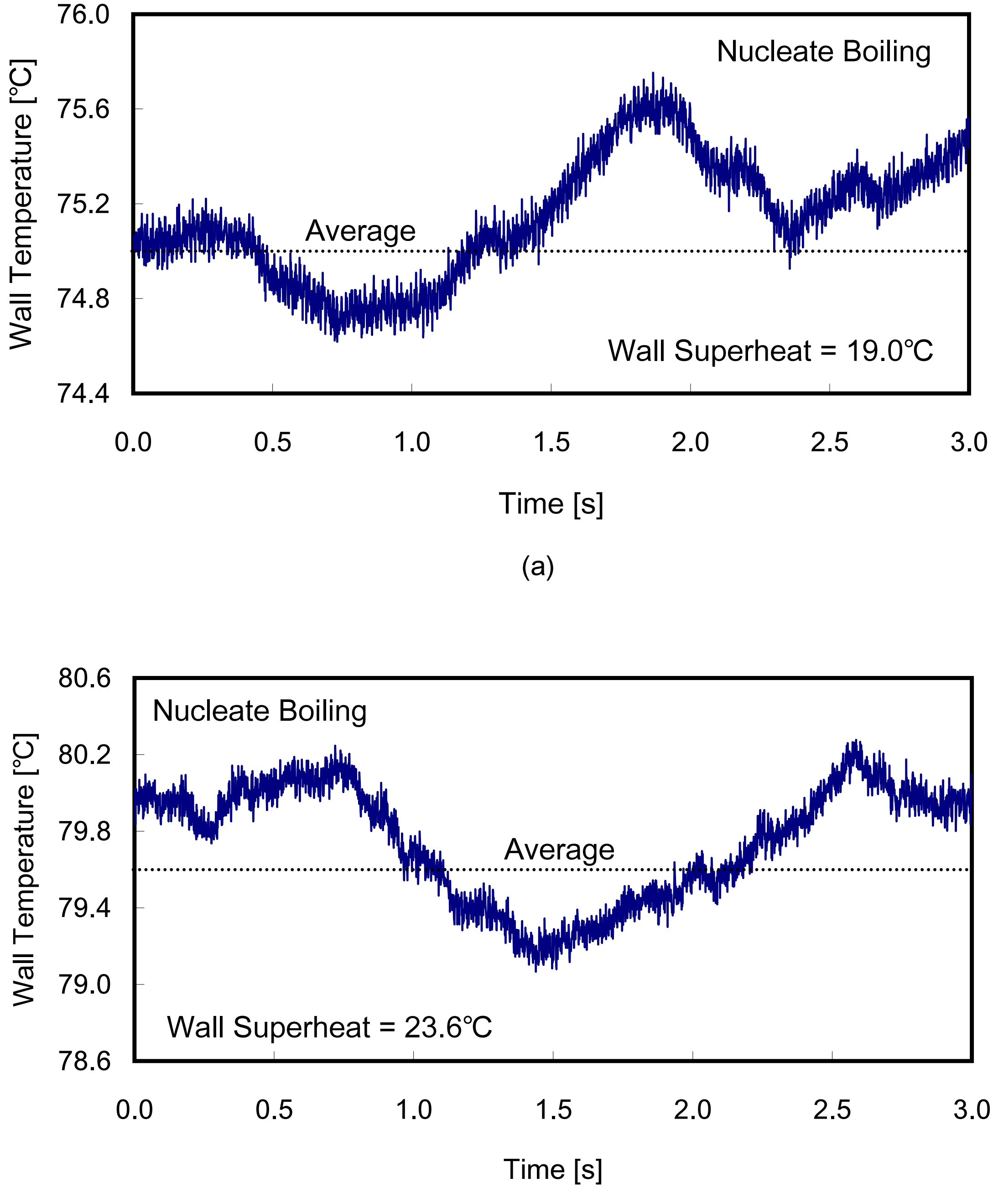

(a)

(b)

Fig. 47. Surface temperature fluctuations measured using TFT in nucleate boiling (a) wall superheat=19.0°C (b) wall superheat=23.6°C .

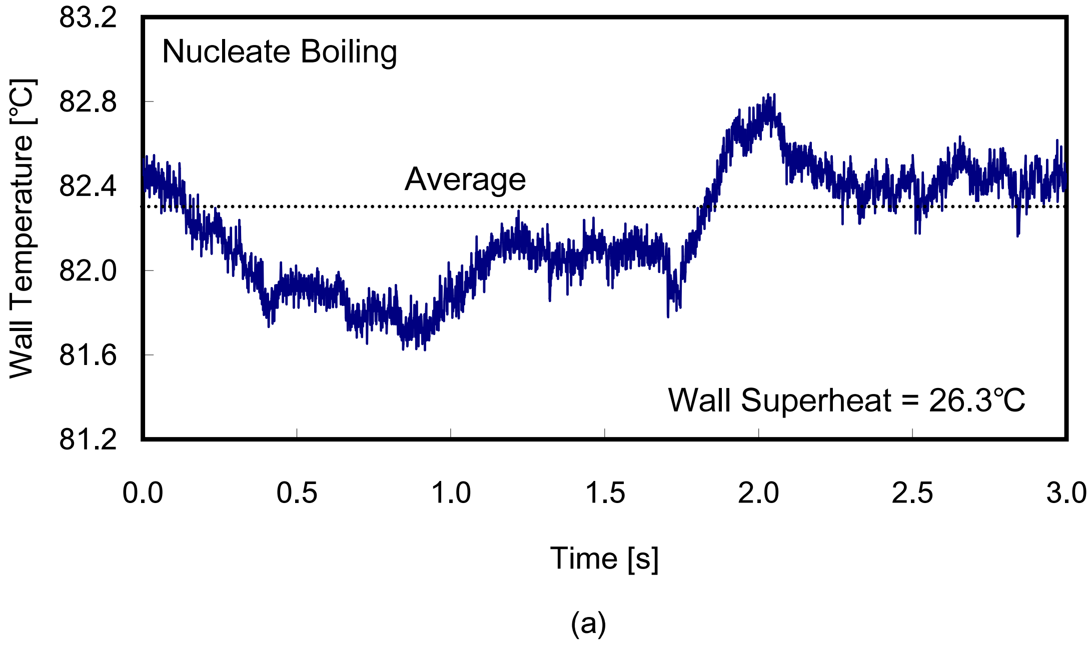

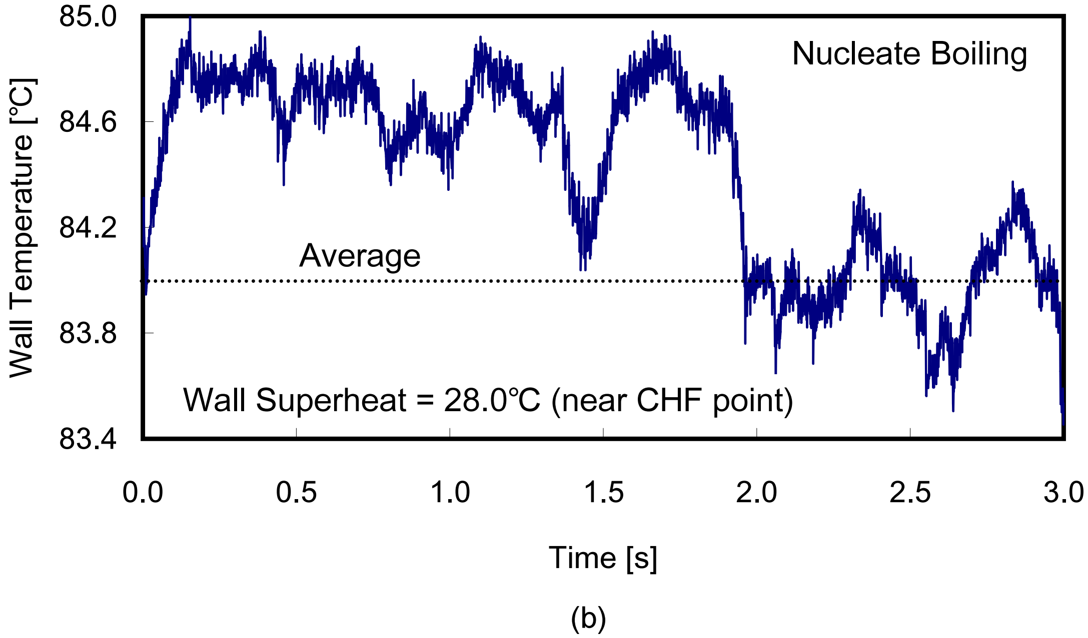

Fig. 48. Surface temperature fluctuations measured using TFT in nucleate boiling (a) wall superheat=26.3°C (b) wall superheat=28.0°C (in the vicinity of CHF point).

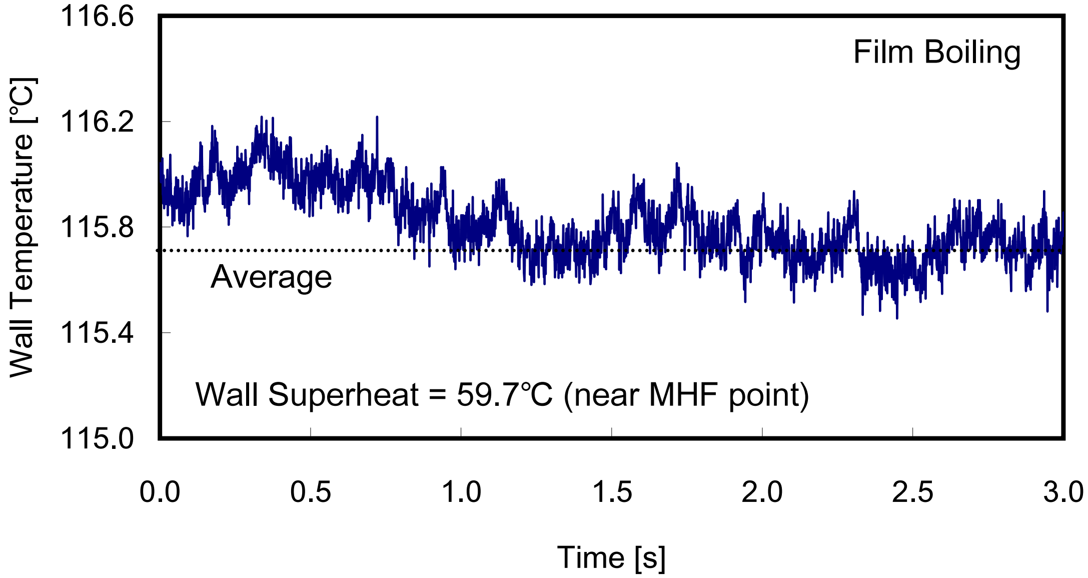

(a)

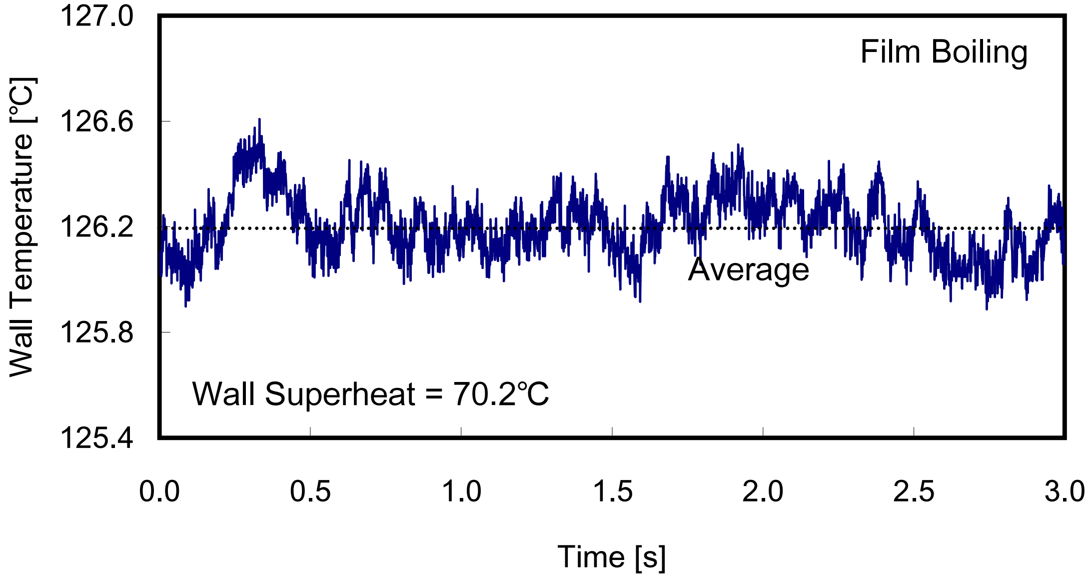

(b)

Fig. 49. Surface temperature fluctuations measured using TFT in film boiling (a) wall superheat=59.7°C (in the vicinity of MHF point (b) wall superheat=70.2°C).

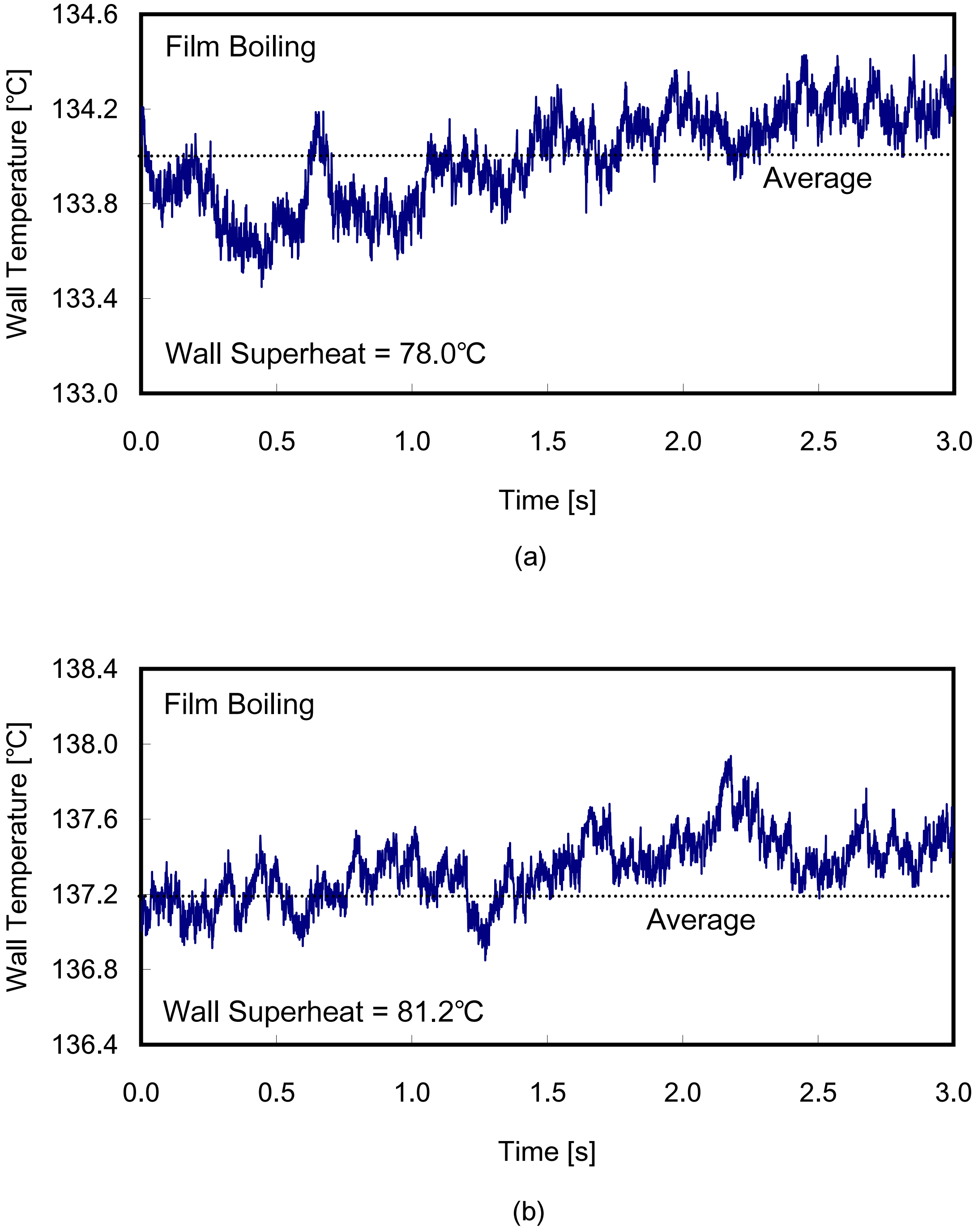

Fig. 50. Surface temperature fluctuations measured using TFT in film boiling (a) wall superheat=78.0°C (b) wall superheat=81.2°C).

any possible relation between the two temperatures. As shown in this figure, the surface temperature has quadratic relation with the top surface temperature of the copper cylinder in nucleate boiling, which is

$$T_s = 17.65 + 0.855T_c - 0.00275T_c^2 \tag{8.1}$$

where T_s is the surface temperature of the silicon wafer (boiling side) in [°C] and T_c is the top surface temperature of the copper cylinder in [°C].

In other words, the rate of increase in the boiling surface temperature is much lower than that in the top surface temperature of the copper cylinder in nucleate boiling. In film boiling, however, the boiling surface temperature has a linear relation to the top surface of the copper cylinder, which shows

$$T_s = 43.83 + 0.4774T_c \tag{8.2}$$

Figure 52 shows the temperature difference between the boiling surface and the top surface of the copper cylinder at a given wall superheat. In nucleate boiling, the rapid temperature separation of the top surface of the copper cylinder from the boiling surface temperature is observed as the wall superheat is increased. In film boiling, however, the gap between the two temperatures increases at a much slower rate than that in nucleate boiling.

c. Overall Thermal Resistance

The overall thermal resistance (including contact resistance) values between the boiling surface and the top surface of the copper cylinder were calculated. The boiling surface temperature was measured using the TFT and the top surface temperature of the copper cylinder was calculated by using the linear extrapolation from tem-

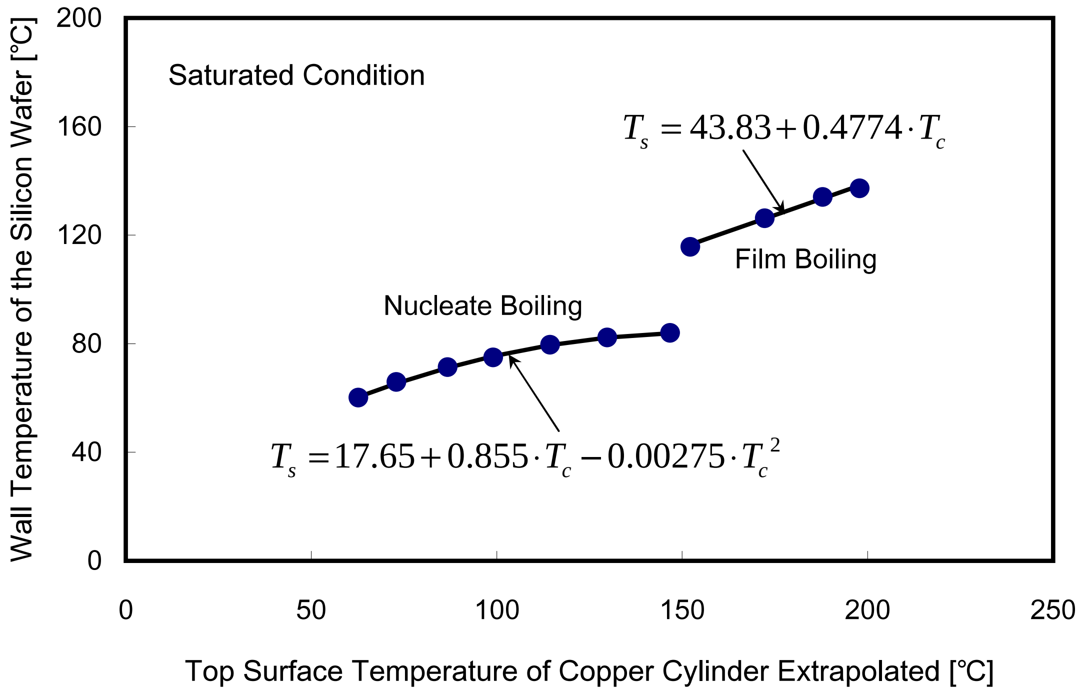

Fig. 51. Surface temperature measured using TFT with respect to the top surface temperature of the copper cylinder observed during boiling experiments.

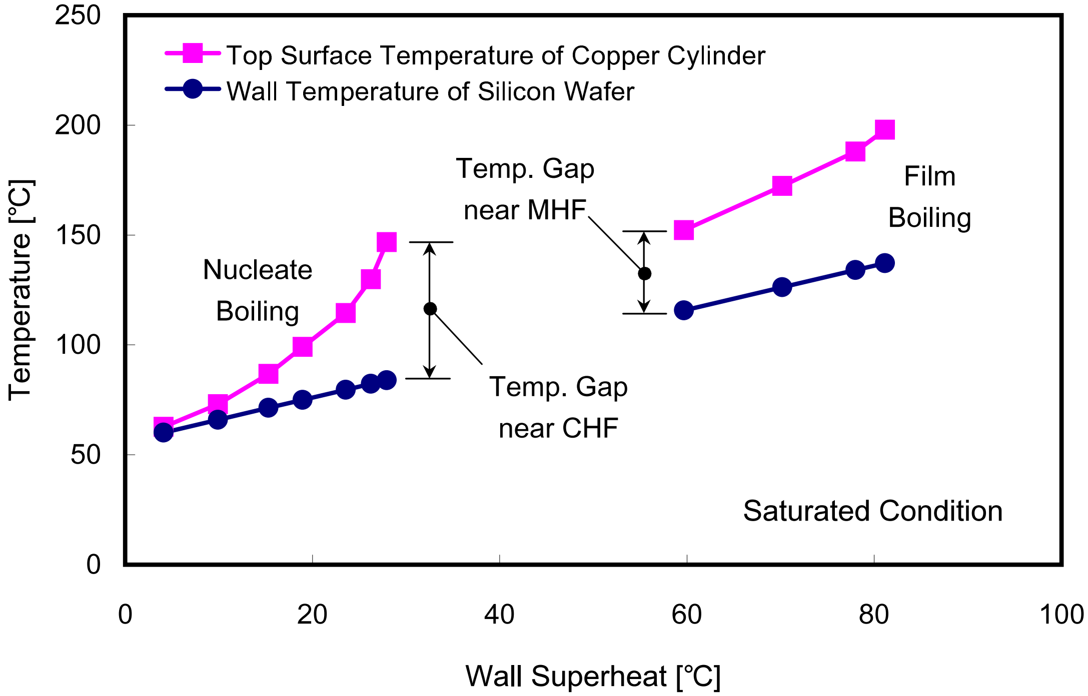

Fig. 52. Temperature difference between the silicon wafer surface (boiling side) and the top surface of copper cylinder observed during boiling experiments.

peratures measured by the K-type thermocouples embedded in the copper cylinder. Between the silicon wafer and the copper cylinder, a pyrex wafer was sandwiched to reduce signal noise from the heaters that were embedded in the copper cylinder. On the top and bottom of the pyrex wafer, there were two layers of thermal grease for removing air that might be trapped between the contacting solids. The distance between the two surfaces was around 1.5 mm. A detailed cross section of the test section (heater apparatus) is shown in Fig. 29. The boiling surface temperatures measured and the top surface temperatures calculated are summarized in Table III. As the wall superheat is increased, the difference between the surface temperature of the silicon wafer and the top surface temperature of the copper cylinder quadratically increases during nucleate boiling. The temperature difference between the two surfaces, however, linearly increases during film boiling. This was discussed in the previous section.

Based on the temperature measurements, the overall thermal resistance between the boiling surface and the top surface of the copper cylinder was calculated. Figure 53 shows the overall thermal resistance correlation. In nucleate boiling, the overall thermal resistance increases as the wall superheat is increased in the lower wall superheat region up to 22°C . After this point, the rate of increase in the overall thermal resistance becomes very small until the boiling is transferred to transition. The presumed reason for this variation in the overall thermal resistance is probably due to the balance of two factors: (1) variation in the thermal properties of the materials (silicon wafer, pyrex wafer, and thermal grease) with temperature and (2) variation in pressure caused by the differential thermal expansion of the two materials (copper and stainless steel) with temperature. At the lower wall superheat region, the thermal properties of the materials is probably a dominant factor that affects the thermal resistance because the pressure differential at this region is too small to influence the

Table III. Surface temperatures on the silicon wafer measured and on the top of the copper cylinder extrapolated.

Nucleate		Wall Superheat			
Boiling		4.1	15.3	23.6	28.0
	Copper Block	62.7	86.8	114.4	146.8
Surface Temperature	Silicon Wafer	60.1	71.3	79.6	84.0
	Difference	2.6	15.5	34.8	62.8

Film		Wall Superheat			
Boiling		59.7	70.2	78.0	81.2
	Copper Block	152.2	172.3	187.9	197.9
Surface Temperature	Silicon Wafer	115.7	126.2	134.0	137.2
	Difference	36.6	46.1	53.9	60.7

thermal resistance. The gasket used between the silicon wafer and the steel clamp for sealing is flexible enough to absorb the pressure force against the materials. This is thought to result in a trend of increase in the overall thermal resistance with the wall superheat at the lower wall superheat region. However, the portion of the pressure force becomes stronger due to the limit of the flexibility of the gasket, as the heater temperature goes up above a wall superheat of 22°C . The increase in the pressure differential squeezes the thermal grease and forces the silicon wafer to move closer to the copper cylinder as the wall superheat goes up, thus, is thought to result in decreased contact resistance during nucleate boiling. In film boiling, the overall thermal resistance increases with a slope of 2.522×10^{-3} as the wall superheat is increased. The presumed reason for this increase is probably due to the variation of the thermal properties of the materials used in this experiment, especially thermal grease and its effect on contact resistance. The portion of the pressure force acting on the silicon wafer probably becomes weaker because the highly increased surface temperature of the silicon wafer causes the gasket to be easily compressed and then releases the pressure force. This variation influences the overall thermal resistance in such a way that it increases with the wall superheat in film boiling.

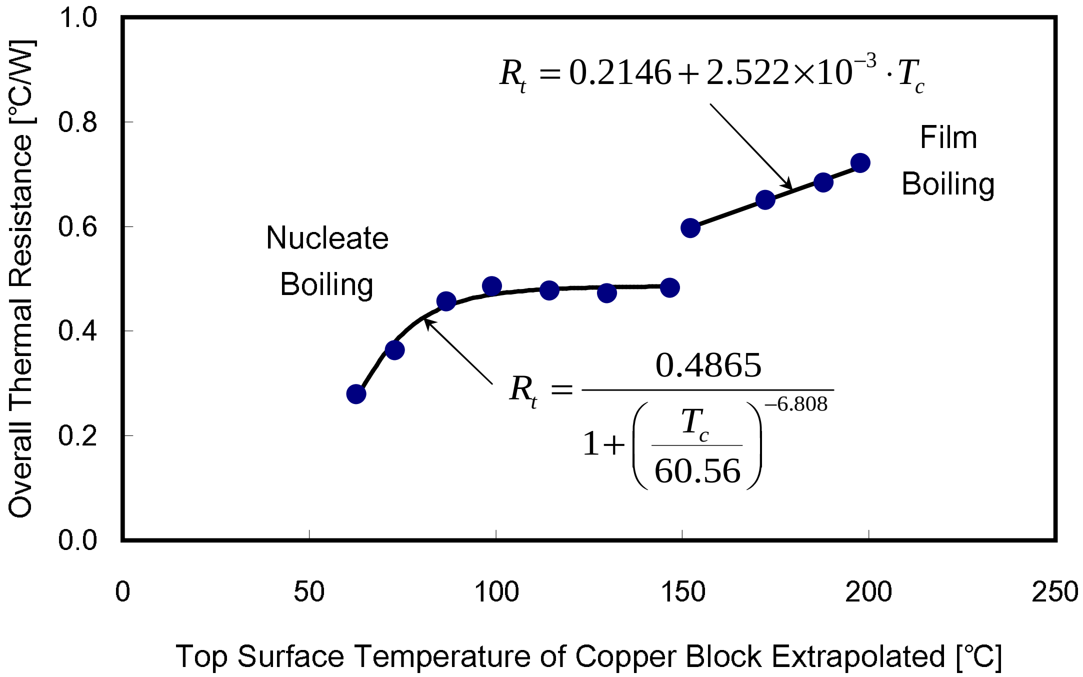

Fig. 53. Overall thermal resistance between the silicon wafer surface (boiling side) and the top surface of copper cylinder observed during boiling experiments.

CHAPTER IX

TWO-PHASE POOL BOILING WITH NANO-STRUCTURED SURFACES: SUMMARY

A. Heat Transfer on Nano-Structured Surfaces

Boiling experiments were conducted using PF-5060 as the test fluid on silicon wafer substrates under saturated and sub-cooled conditions (5°C and 10°C). The experiments were conducted with a bare silicon wafer and two silicon wafers containing uniform layers of vertically aligned multi-walled carbon nanotubes (MWCNT) of two different heights, respectively (Type A: 9 μm and Type B: 25 μm). The results of this experimental study are summarized as follows:

1. For nucleate boiling, the MWCNT forests (both 9 and 25 μm height) yield higher wall heat flux values under saturated and sub-cooled conditions (5°C and 10°C), compared to the bare (smooth) silicon wafer. However, the wall heat flux is found to be less sensitive to the height of the MWCNT. The wall heat flux value in the vicinity of the CHF for Type-B MWCNT exceeds the corresponding value for Type-A MWCNT by 12% under saturated conditions. However, the corresponding wall superheat for Type-B MWCNT is not noticeable compared to Type-A MWCNT.

2. For film boiling, the wall heat flux is strongly sensitive to the height of the MWCNT forests. For Type-B MWCNT (25 μm height) the wall heat flux is enhanced under saturated and sub-cooled conditions (5°C and 10°C), compared to control experiments performed on the bare silicon wafer. However, for Type-A MWCNT (9 μm height), the wall heat flux values are similar to the corrsponding values for the bare silicon wafer during film boiling. During sub-cooled film

boiling, Type-B MWCNT is more sensitive to sub-cooling and causes great enhancement of the wall heat flux with increased sub-cooling compared to Type-A MWCNT and the bare silicon wafer.

B. Surface Temperature Measurement on TFT

Micro-machined thin film thermocouples (TFT) were fabricated to measure the surface temperature on a smooth silicon wafer in nucleate and film boiling. The temperature data measured with the TFT were used to induce an overall thermal resistance correlation between the boiling surface and the top surface of the copper cylinder for predicting surface temperature during the boiling experiments with MWCNT. The results of this experimental study are summarized as follows:

1. The surface micro-machined thin film thermocouple has a low characteristic time constant which enables it to measure the surface temperature with a high temporal resolution. The calibration results show that the temperature response of the micro-machined thermocouple is linear compared with a wire-bead K-type thermocouple calibrated against a NIST calibrated mercury thermometer.

2. The heat transfer performance on a silicon wafer was validated by comparing the wall heat flux values with the corresponding values measured from the boiling experiments performed on a copper surface. The overall thermal resistance correlation between the boiling surface and the top surface of the copper cylinder was derived from the experiment.

CHAPTER X

CONCLUSIONS

A. Effect of Blockages on Heat Transfer

For the experiments conducted to study the local and average heat transfer coefficient on the channel wall, the following conclusions are drawn:

1. The elongated holes in the blockages enhance more heat transfer than the round holes. The smaller elongated holes with the largest aspect ratio (Case S-4) appear to enhance the heat (mass) transfer the most.

2. For the smaller holes in the blockages, increase in hole aspect ratio causes the heat (mass) transfer on the wall segments to be enhanced due to the increase in the reattachment region downstream of the holes. In this case, the flow reattachment is the dominant factor which determines the heat transfer on the channel wall.

3. For the larger holes in the blockages, increase in hole aspect ratio causes the heat (mass) transfer on the wall segments to be reduced slightly due to the increase in the recirculating region downstream of the upstream blockage between the holes. In this case, the flow recirculation is the dominant factor which determines the heat transfer on the channel wall.

4. The average pressure drop across the blockages increases as the hole aspect ratio is increased. The blockages with the smaller holes increase the pressure drop more than the blockages with the larger holes for the same hole aspect ratio.

5. The blockages with the larger holes outperform the blockages with the smaller holes. For the blockages with the smaller holes, the TP values for the three

elongated hole cases are about the same or slightly higher than those for the round hole cases. For the blockages with the larger holes, the TP values decrease with an increase of the hole aspect ratio.

Based on the results of this study, blockages with elongated holes and a small spacing between holes are recommended for a cooling channel near the trailing edge of an internally-cooled gas turbine airfoil. Additional parametric studies are needed to obtain local and average heat transfer data to optimize the size and the aspect ratio of the holes in the blockages, the spacing between the holes, and the spacing between two blockages, relative to the channel height. Heat transfer data are also needed on the upstream surfaces of the blockages and on the surfaces of the holes, where the heat transfer is expected to be very high, and also on the downstream surfaces of the blockages, since a substantial amount of heat may be conducted from the pressure and suction walls to the blockages, and is then transferred from these surfaces to the air in a cooling channel near the trailing edge of an airfoil. The total area of the surfaces of the blockages may be comparable with the area of the surfaces of the pressure and suction walls that are exposed to the cooling air.

B. Heat Transfer on Nano-Structured Surfaces

For the experiments conducted to study the efficacy in heat transfer enhancement on the surfaces with MWCNT, the following conclusions are drawn:

1. In the nucleate boiling regime, the wall heat flux is found to be less sensitive to the height of the MWCNT.
2. For nucleate boiling, the MWCNT arrays (both 9 and 25 μm height) yield higher wall heat fluxes under saturated, 5°C sub-cooling, 10°C sub-cooling conditions, compared to the bare (smooth) silicon wafer.

3. Type-B MWCNT is observed to augment the critical heat flux (CHF) by 68% and 65% compared to the bare silicon wafer under saturated and 10°C sub-cooling, respectively.

4. The wall heat flux value in the vicinity of the CHF for Type-B MWCNT exceeds that for Type-A MWCNT by 12% under saturated conditions. However, the associated wall superheat for Type-B MWCNT is marginally lower compared to Type-A MWCNT.

5. In the film boiling regime, the wall heat flux is strongly sensitive to the height of the MWCNT arrays. For Type-B MWCNT (25 μm height) the wall heat fluxes are enhanced under saturated, 5°C sub-cooling, 10°C sub-cooling conditions (compared to control experiments performed on the bare silicon wafer). However, for Type-A MWCNT (9 μm height) the wall heat fluxes are similar to the corresponding values for the bare silicon wafer during film boiling. This is consistent with dynamic models for film boiling reported in the literature.

6. During sub-cooled film boiling, Type-B MWCNT is more sensitive to sub-cooling and causes greater enhancement of the wall heat flux with increased sub-cooling compared to Type-A MWCNT and the bare silicon wafer.

7. Surface temperature can be successfully measured with the thin film thermocouple micro-machined on a silicon wafer. Comparing the measured temperature data, it can be concluded that the surface temperature data measured in nucleate boiling have a different fluctuation pattern from those measured in film boiling.

8. The induced overall thermal resistance correlation between the boiling surface and the top surface of the copper cylinder shows that this value increases with

the increase in the wall superheat during nucleate and film boiling. However, the trend in nucleate boiling is different from that in film boiling.

REFERENCES

[1] Moon, S.W. and Lau, S.C., “Heat transfer between blockages with holes in a rectangular channel,” *ASME J. Heat Transfer*, vol. 125, pp. 587-594, 2003.

[2] Lau, S.C, Cervantes, J., Han, J.C., and Rudolph, R.J., Flannery, K., “Measurements of wall heat (mass) transfer for flow through blockages with round and square holes in a wide rectangular channel,” *Int. J. Heat Mass Transfer*, vol. 46, pp. 3991-4001, 2003.

[3] Ujereh, O.S., Mudawar, I., Amama, P.B., Fisher, T.S., and Ou, W., “Enhanced pool boiling using carbon nanotube arrays on a silicon surface,” in *Proceedings of the 2005 ASME International Mechanical Engineering Congress and Exposition*, Orlando, FL, pp. 1-6, 2005.

[4] Banerjee, D. and Dhir, V.K., “Study of subcooled film boiling on a horizontal disc: Part 1 Analysis,” *ASME J. Heat Transfer*, vol. 123, pp. 271-284, 2001.

[5] Banerjee, D. and Dhir, V.K., “Study of subcooled film boiling on a horizontal disc: Part 2 Analysis,” *ASME J. Heat Transfer*, vol. 123, pp. 285-293, 2001.

[6] Banerjee, D., Son, G., and Dhir, V.K., “Conjugate thermal and hydrodynamic analysis of saturated film boiling from a horizontal surface,” in *Proceedings of the 1996 ASME International Mechanical Engineering Congress and Exposition*, Atlanta, GA, pp. 57-64, 1996.

[7] Takeishi, K., “Heat transfer research in high temperature industrial gas turbines,” in *Proceedings of International Symposium on Heat Transfer in Turbomachinery*, Marathon, Greece, 1992, pp. 3-18.

[8] Han, J.C. and Park, J.S., “Developing heat transfer in rectangular channels with rib turbulators,” *Int. J. Heat Mass Transfer*, vol. 31, pp. 183-195, 1987.

[9] Han, J.C. and Zhang, Y.M., “High performance heat transfer ducts with parallel broken and V-shaped broken ribs,” *Int. J. Heat Mass Transfer*, vol. 35, pp. 513-523, 1992.

[10] VanFossen, G.J., “Heat transfer coefficient for staggered arrays of short pin fins,” *ASME Journal of Engineering for Power*, vol. 104, pp. 268-274, 1982.

[11] Taslim, M.E. and Spring, S.D., “Effects of turbulator profile and spacing on heat transfer and friction in a channel,” *AIAA Journal of Thermodynamics and Heat Transfer*, vol. 8, pp. 555-562, 1994.

[12] Kukreja, R.T. and Lau, S.C., “Distributions of local heat transfer coefficient on surfaces with solid and perforated ribs,” *Journal of Enhanced Heat Transfer*, vol. 5, pp. 9-21, 1998.

[13] Kukreja, R.T, Lau, S.C., and McMillan, R.D., “Laocal heat (mass) transfer distribution in a square channel with full and V-shaped ribs,” *Int. J. Heat Mass Transfer*, vol. 36, pp. 2013-2020, 1993.

[14] Lau, S.C., Kim, Y.S., and Han, J.C., “Local endwall heat/mass transfer distributions in pin fin channels,” *J. Thermophysics*, vol. 1, pp. 365-372, 1987.

[15] Han, J.C., Dutta, S., and Ekkad, S.V., *Gas Turbine Heat Transfer and Cooling Technology*, New York: Taylor and Francis, 2000.

[16] Lau, S.C., Enhanced internal cooling of gas turbine airfoil, in Sunden, B., Faghri, M, Eds., *Heat Transfer in Gas Turbines*, Southhampton, UK: WIT Press, 2001.

[17] Lau, S.C., Kukreja, R.T., and McMillin, R.D., “Effects of V-shaped rib arrays on turbulent heat transfer and friction of fully developed flow in a square channel,” *Int. J. Heat Mass Transfer*, vol. 34, pp. 1605-1616, 1991.

[18] Buchlin, J.M., “Convective heat transfer in a channel with perforated ribs,” *Int. J. Thermal Sciences*, vol. 41, pp. 332-340, 2002.

[19] Bailey, J.C. and Bunker, R.S., “Heat transfer and friction in channels with very high blockages 45° staggered turbulators,” in *Proceedings of ASME Turbo Expo 2003*, Atlanta, GA, 2003, pp. 451-458.

[20] Armstrong, J. and Winstanley, D., “A review of staggered array pin fin heat transfer for turbine cooling applications,” *Transactions of ASME*, vol. 110, pp. 94-103, 1988.

[21] Metzger, D.E., Berry, R.A., and Bronson, J.P., “Developing heat transfer in rectangular ducts with arrays of short pin fins,” *ASME Paper No. 81-WA/HT-6*, 1981.

[22] Metzger, D.E. and Haley, S.W., “Heat transfer experiments and flow visualization for arrays of short pin fins,” *ASME Paper No. 82-GT-138*, 1982.

[23] Metzger, D.E., Fan, Z.X., and Shepard, W.B., “Pressure loss and heat transfer through multiple rows of short pin fins,” in U. Grigull et al., Eds., *Heat Transfer*, 1982, vol. 3, Washington DC: Hemisphere Publishing Corp., pp. 137-142, 1982.

[24] Metzger, D.E., Shepard, W.B., and Haley, S.W., “Row resolved heat transfer variations in pin fin arrays including effects of non-uniform arrays and flow convergence,” *ASME Paper No. 86-GT-132*, 1986.

[25] Zukauskas, A.A., "Heat transfer from tubes in cross flow," *Adv. in Heat Tranfer*, vol. 8, pp. 116-133, 1972.

[26] Brigham, B.A. and VanFossen, G.J., "Length-to-diameter ratio and row number effects in short pin fin heat transfer," *ASME J. Engineering for Gas Turbines and Power*, vol. 106, pp. 241-245, 1984.

[27] Lau, S.C., Han, J.C., and Kim, Y.S., "Turbulent heat transfer and friction in pin fin channels with lateral flow ejection," *ASME J. Heat Transfer*, vol. 111, pp. 51-58, 1989.

[28] Lau, S.C. and Han, J.C., Batten, T., "Heat transfer, pressure drop, and mass flow rate in pin fin channels with long and short trailing edge ejection holes," *ASME J. Turbomachinery*, vol. 111, pp. 116-123, 1989.

[29] Lau, S.C., McMillin, R.D., and Kukreja, R.T., "Segmental heat transfer in a pin fin channel with ejection holes," *Int. J. Heat Mass Transfer*, vol. 35, pp. 1407-1417, 1992.

[30] Ambrose, D., Lawrenson, I.J., and Sprake, C.H.S., "The vapor pressure of naphthalene," *Journal of Chemical Thermodynamics*, vol. 7, pp. 1172-1176, 1975.

[31] Goldstein, R.J. and Cho, H.H., "A review of mass transfer measurements using naphthalene sublimation," *Experimental Thermal and Fluid Science*, vol. 10, pp. 416-434, 1995.

[32] Eckert, E.R.G., "Analogies to heat transfer processes," in Eckert, E.R.G. and Goldstein, R.J., Eds., *Measurements in Heat Transfer*, New York: Hemisphere Publishing Corp., pp. 397-423, 1976.

[33] Coleman, H.W. and Steele, W.G., *Experimentation and Uncertainty Analysis for Engineers*, New York: John Wiley & Sons, 1989.

[34] Nukiyama, S, "The maximum and minimum values of the heat Q transmitted from metal to boiling water under atmospheric pressure," *Int. J. Heat Mass Transfer*, vol. 9, pp. 1419-1433, 1934.

[35] Dhir, V.K., "Boiling heat transfer," *Annual Review of Fluid Mechanics*, vol. 30, pp. 365-401, 1988.

[36] Dhir, V.K., "Mechanistic prediction of nucleate boiling heat transfer-achievable or hopeless task?" *ASME J. Heat Transfer*, vol. 30, pp. 365-401, 2006.

[37] Son, G., Ramanujapu, N., and Dhir, V.K., "Numerical simulation of bubble merger process on a single nucleation site during pool nucleate boiling," *ASME J. Heat Transfer*, vol. 124, pp. 51-62, 2002.

[38] Mukherjee, A. and Dhir, V.K., "Study of lateral merger of vapor bubbles during nucleate pool boiling," *ASME J. Heat Transfer*, vol. 126, pp. 1023-1039, 2004.

[39] Zhang, L. and Shoji, M., "Nucleation site interaction in pool boiling on the artificial surface," *Int. J. Heat Mass Transfer*, vol. 46, pp. 513-522, 2003.

[40] Kenning, D.B.T. and Yan, Y., "Pool boiling heat transfer on a thin plate: features revealed by liquid crystal thermography," *Int. J. Heat Mass Transfer*, vol. 39, pp. 3117-3137, 1996.

[41] Mei, R., "Vapor bubble growth in heterogeneous boiling-I. Formation," *Int. J. Heat Mass Transfer*, vol. 38, pp. 909-919, 1995.

[42] Chang, Y.P. and Flannery, K., "Wave theory of heat transfer in film boiling," *ASME J. Heat Transfer*, vol. 81, pp. 112-123, 1959.

[43] Zuber, N., “Hydrodynamic aspects of nucleate boiling,” Ph.D. dissertation, Department of Engineering, University of California, Los Angeles, CA, 1959.

[44] Sernas, V., Lienhard, J.H, and Dhir, V.K., “The Taylor wave configuration during boiling from a flat plate,” *Int. J. Heat Mass Transfer*, vol. 16, pp. 1820-1821, 1973.

[45] Bradfield, W.S., “Liquid-solid contact in stable film boiling,” *I&EC Fundamentals*, vol. 5, pp. 200-204, 1966.

[46] Borishansky, V.M., “Influence of pressure and properties of the liquid on the cessation of film boiling with free convection in a large space,” in Kutateladze, S.S., Eds., *Problems of Heat Transfer During a Change of State: a Collection of Articles*, AEC-TR-3405, pp. 101-108, 1953.

[47] Berenson, P.J., “Experiments on pool-boiling heat transfer,”, *Int. J. Heat Mass Transfer*, vol. 5, pp. 985-999, 1962.

[48] Henry, Robert E., “A correlation for minimum film boiling temperature,” *AICHE Symp*, series no. 138, vol. 70, pp. 81-90, 1974.

[49] Hohmann,C. and Stephan, P., “Microscale temperature measurement at an evaporating liquid meniscus,” *Experimental Thermal and Fluid Science*, vol. 26, pp. 157-162, 2002.

[50] Haramura, Y., “Heat flux fluctuation on steady state transition boiling,” in *ASME/JSME Thermal Engineering Conference*, vol. 2, pp. 209-214, 1995.

[51] Ohtake, H. and Koizumi, Y., “Study of propagative collapse of a vapor film in film boiling (mechanism of vapor-film collapse at wall temperature above the

thermodynamic limit of liquid superheat)," *Int. J. Heat Mass Transfer*, vol. 47, pp. 1965-1977, 2004.

[52] Park, J.J. and Taya, M.,, "Design of micro-arrayed thin film thermocouples (TFTC)," in *Proceedings of the 2003 International Electronic Packaging Technical Conference and Exhibition*, IPACK2003-35040, Maui, HI, pp. 213-217, 2003.

[53] Kreider, K.G. and Gillen, G.,, "High temperature materials for thin-film thermocouples on silicon wafers," *Thin Solid Films*, vol. 376, pp. 32-37, 2000.

[54] Kreider, K.G. and DiMeo, F., "Platinum/palladium thin-film thermocouples for temperature measurements on silicon wafers," *Sensors and Actuators A: Physical*, vol. 69, pp. 48-52, 1998.

[55] Henry, C.D. and Kim, J., "A study of the effects of heater size, subcooling, and gravity level on pool boiling heat transfer," *Int. J. Heat and Fluid Flow*, vol. 25, pp. 262-273, 2004.

[56] Ramaswamy, C., Joshi, Y.K, Nakayama, W., and Johnson, W.B., "Combined effects of sub-cooling and operating pressure on the performance of a two-chamber thermo-siphon," *IEEE Transactions on Component and Packaging Technology*, vol. 23, pp. 61-69, 2000.

[57] Ramaswamy, C., Joshi, Y., Nakayama, W., and Johnson, W.B., "Effects of varying geometrical parameters on boiling from microfabricated enhanced structures," *ASME J. Heat Transfer*, vol. 125, pp. 103-109, 2003.

[58] Mudawar, I. and Anderson, T. M., "Optimization of enhanced surfaces for high flux chip cooling by pool boiling," *Trans. ASME J. Electron. Packag.*, vol. 115, pp. 89-100, 1993.

[59] Coursey, J., Roh, H. K., Kim, J. H., and Boudreaux, P. J., "Graphite foam thermosyphon evaporator performance: Parametric investigation of the effects of working fluid, liquid level, and chamber pressure," in *Proceeding of the 2002 ASME International Mechanical Engineering Congress and Exposition*, New Orleans, LA, pp. 165-170, 2002.

[60] Iijima, S., "Helical microtubules of graphitic carbon," *Nature*, vol. 354, pp. 56-58, 1991.

[61] Berber, S., Kwon, Y. K., and Tomanek, D., "Unusually high thermal conductivity of carbon nanotubes," *Phys. Rev. Lett.*, vol. 84, pp. 4613-4616, 2000.

[62] Zhang, M., Atkinson, K.R., and Baughman, R.H., "Multifunctional carbon nanotube yarns by downsizing an ancient technology," *Science*, vol. 306, pp. 1358-1361, 2004.

[63] Sinha, N., "Design, fabrication, packaging and testing of thin film thermocouples for boiling studies," M.S. thesis, Department of Mechanical Engineering, Texas A&M University, College Station, TX, 2006.

[64] Kutateladze, S.S., "On the transition to film boiling under natural convection," *Kotloturbostroenie*, vol. 3, pp. 10-12, 1948.

[65] Zuber, N., "On the stability of boiling heat transfer," *Trans. ASME*, vol. 80, pp. 711-720, 1958.

[66] Gaertner, R.F., "Distribution of active sites in the nucleate boiling of liquids," *Chemical Engineering Progress Symposium Series*, vol. 59, pp. 52-61, 1963.

[67] Debey, D., Bluhm, R., Habets, N. , and Kurz, H., "Fabrication of planar thermocouples for real-time measurements of temperature profiles in polymer melts,"

Sensors and Actuators A: Physical, vol. 58, pp. 179-184, 1997.

[68] Carey, V.P., *Liquid-Vapor Phase-Change Phenomena: an Introduction to the Thermophysics of Vaporization and Condensation Processes in Heat Transfer Equipment*, Hebron, KY: Taylor & Francis, 1992.

APPENDIX A

CALCULATED DATA FOR MASS TRANSFER MEASUREMENT

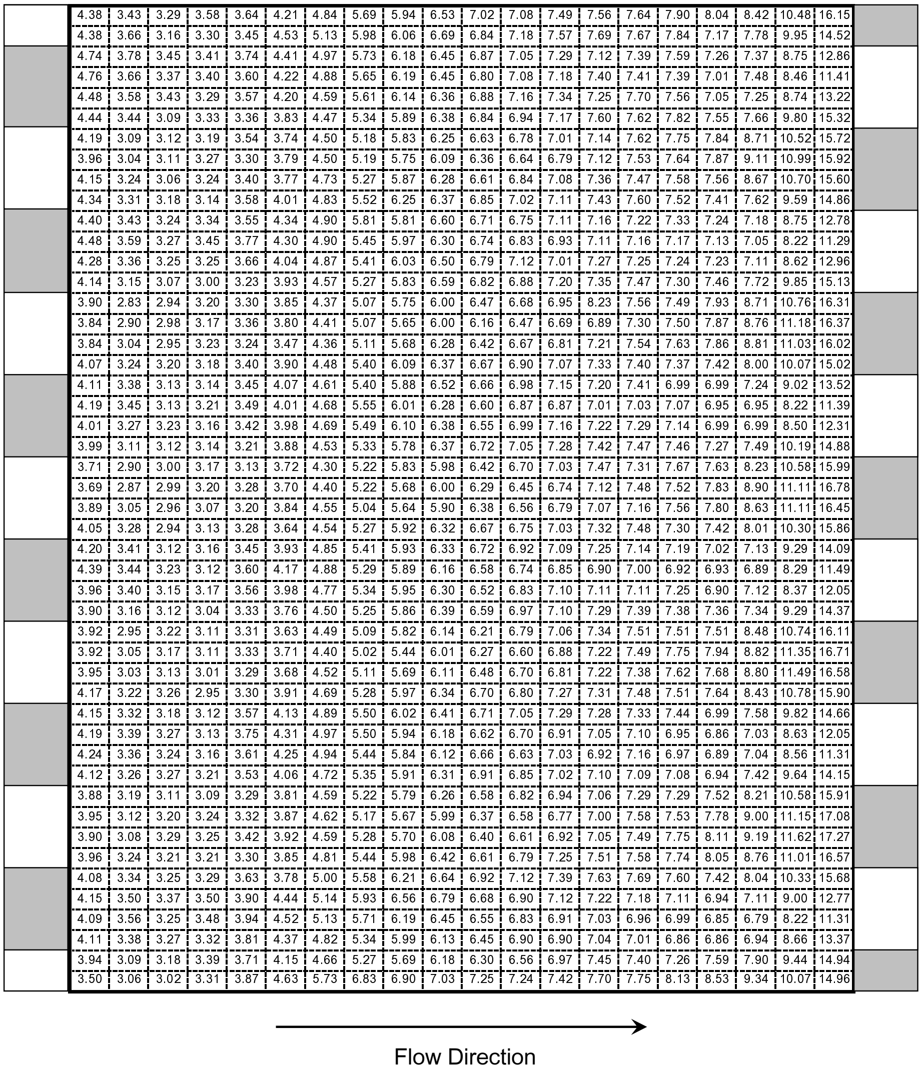

4.38	3.43	3.29	3.58	3.64	4.21	4.84	5.69	5.94	6.53	7.02	7.08	7.49	7.56	7.64	7.90	8.04	8.42	10.48	16.15
4.38	3.66	3.16	3.30	3.45	4.53	5.13	5.98	6.06	6.69	6.84	7.18	7.57	7.69	7.67	7.84	7.17	7.78	9.95	14.52
4.74	3.78	3.45	3.41	3.74	4.41	4.97	5.73	6.18	6.45	6.87	7.05	7.29	7.12	7.39	7.59	7.26	7.37	8.75	12.86
4.76	3.66	3.37	3.40	3.60	4.22	4.88	5.65	6.19	6.45	6.80	7.08	7.18	7.40	7.41	7.39	7.01	7.48	8.46	11.41
4.48	3.58	3.43	3.29	3.57	4.20	4.59	5.61	6.14	6.36	6.88	7.16	7.34	7.25	7.70	7.56	7.05	7.25	8.74	13.22
4.44	3.44	3.09	3.33	3.36	3.83	4.47	5.34	5.89	6.38	6.84	6.94	7.17	7.60	7.62	7.82	7.55	7.66	9.80	15.32
4.19	3.09	3.12	3.19	3.54	3.74	4.50	5.18	5.83	6.25	6.63	6.78	7.01	7.14	7.62	7.75	7.84	8.71	10.52	15.72
3.96	3.04	3.11	3.27	3.30	3.79	4.50	5.19	5.75	6.09	6.36	6.64	6.79	7.12	7.53	7.64	7.87	9.11	10.99	15.92
4.15	3.24	3.06	3.24	3.40	3.77	4.73	5.27	5.87	6.28	6.61	6.84	7.08	7.36	7.47	7.58	7.56	8.67	10.70	15.60
4.34	3.31	3.18	3.14	3.58	4.01	4.83	5.52	6.25	6.37	6.85	7.02	7.11	7.43	7.60	7.52	7.41	7.62	9.59	14.86
4.40	3.43	3.24	3.34	3.55	4.34	4.90	5.81	5.81	6.60	6.71	6.75	7.11	7.16	7.22	7.33	7.24	7.18	8.75	12.78
4.48	3.59	3.27	3.45	3.77	4.30	4.90	5.45	5.97	6.30	6.74	6.83	6.93	7.11	7.16	7.17	7.13	7.05	8.22	11.29
4.28	3.36	3.25	3.25	3.66	4.04	4.87	5.41	6.03	6.50	6.79	7.12	7.01	7.27	7.25	7.24	7.23	7.11	8.62	12.96
4.14	3.15	3.07	3.00	3.23	3.93	4.57	5.27	5.83	6.59	6.82	6.88	7.20	7.35	7.47	7.30	7.46	7.72	9.85	15.13
3.90	2.83	2.94	3.20	3.30	3.85	4.37	5.07	5.75	6.00	6.47	6.68	6.95	8.23	7.56	7.49	7.93	8.71	10.76	16.31
3.84	2.90	2.98	3.17	3.36	3.80	4.41	5.07	5.65	6.00	6.16	6.47	6.69	6.89	7.30	7.50	7.87	8.76	11.18	16.37
3.84	3.04	2.95	3.23	3.24	3.47	4.36	5.11	5.68	6.28	6.42	6.67	6.81	7.21	7.54	7.63	7.86	8.81	11.03	16.02
4.07	3.24	3.20	3.18	3.40	3.90	4.48	5.40	6.09	6.37	6.67	6.90	7.07	7.33	7.40	7.37	7.42	8.00	10.07	15.02
4.11	3.38	3.13	3.14	3.45	4.07	4.61	5.40	5.88	6.52	6.66	6.98	7.15	7.20	7.41	6.99	6.99	7.24	9.02	13.52
4.19	3.45	3.13	3.21	3.49	4.01	4.68	5.55	6.01	6.28	6.60	6.87	6.87	7.01	7.03	7.07	6.95	6.95	8.22	11.39
4.01	3.27	3.23	3.16	3.42	3.98	4.69	5.49	6.10	6.38	6.55	6.99	7.16	7.22	7.29	7.14	6.99	6.99	8.50	12.31
3.99	3.11	3.12	3.14	3.21	3.88	4.53	5.33	5.78	6.37	6.72	7.05	7.28	7.42	7.47	7.46	7.27	7.49	10.19	14.88
3.71	2.90	3.00	3.17	3.13	3.72	4.30	5.22	5.83	5.98	6.42	6.70	7.03	7.47	7.31	7.67	7.63	8.23	10.58	15.99
3.69	2.87	2.99	3.20	3.28	3.70	4.40	5.22	5.68	6.00	6.29	6.45	6.74	7.12	7.48	7.52	7.83	8.90	11.11	16.78
3.89	3.05	2.96	3.07	3.20	3.84	4.55	5.04	5.64	5.90	6.38	6.56	6.79	7.07	7.16	7.56	7.80	8.63	11.11	16.45
4.05	3.28	2.94	3.13	3.28	3.64	4.54	5.27	5.92	6.32	6.67	6.75	7.03	7.32	7.48	7.30	7.42	8.01	10.30	15.86
4.20	3.41	3.12	3.16	3.45	3.93	4.85	5.41	5.93	6.33	6.72	6.92	7.09	7.25	7.14	7.19	7.02	7.13	9.29	14.09
4.39	3.44	3.23	3.12	3.60	4.17	4.88	5.29	5.89	6.16	6.58	6.74	6.85	6.90	7.00	6.92	6.93	6.89	8.29	11.49
3.96	3.40	3.15	3.17	3.56	3.98	4.77	5.34	5.95	6.30	6.52	6.83	7.10	7.11	7.11	7.25	6.90	7.12	8.37	12.05
3.90	3.16	3.12	3.04	3.33	3.76	4.50	5.25	5.86	6.39	6.59	6.97	7.10	7.29	7.39	7.38	7.36	7.34	9.29	14.37
3.92	2.95	3.22	3.11	3.31	3.63	4.49	5.09	5.82	6.14	6.21	6.79	7.06	7.34	7.51	7.51	7.51	8.48	10.74	16.11
3.92	3.05	3.17	3.11	3.33	3.71	4.40	5.02	5.44	6.01	6.27	6.60	6.88	7.22	7.49	7.75	7.94	8.82	11.35	16.71
3.95	3.03	3.13	3.01	3.29	3.68	4.52	5.11	5.69	6.11	6.48	6.70	6.81	7.22	7.38	7.62	7.68	8.80	11.49	16.58
4.17	3.22	3.26	2.95	3.30	3.91	4.69	5.28	5.97	6.34	6.70	6.80	7.27	7.31	7.48	7.51	7.64	8.43	10.78	15.90
4.15	3.32	3.18	3.12	3.57	4.13	4.89	5.50	6.02	6.41	6.71	7.05	7.29	7.28	7.33	7.44	6.99	7.58	9.82	14.66
4.19	3.39	3.27	3.13	3.75	4.31	4.97	5.50	5.94	6.18	6.62	6.70	6.91	7.05	7.10	6.95	6.86	7.03	8.63	12.05
4.24	3.36	3.24	3.16	3.61	4.25	4.94	5.44	5.84	6.12	6.66	6.63	7.03	6.92	7.16	6.97	6.89	7.04	8.56	11.31
4.12	3.26	3.27	3.21	3.53	4.06	4.72	5.35	5.91	6.31	6.91	6.85	7.02	7.10	7.09	7.08	6.94	7.42	9.64	14.15
3.88	3.19	3.11	3.09	3.29	3.81	4.59	5.22	5.79	6.26	6.58	6.82	6.94	7.06	7.29	7.29	7.52	8.21	10.58	15.91
3.95	3.12	3.20	3.24	3.32	3.87	4.62	5.17	5.67	5.99	6.37	6.58	6.77	7.00	7.58	7.53	7.78	9.00	11.15	17.08
3.90	3.08	3.29	3.25	3.42	3.92	4.59	5.28	5.70	6.08	6.40	6.61	6.92	7.05	7.49	7.75	8.11	9.19	11.62	17.27
3.96	3.24	3.21	3.21	3.30	3.85	4.81	5.44	5.98	6.42	6.61	6.79	7.25	7.51	7.58	7.74	8.05	8.76	11.01	16.57
4.08	3.34	3.25	3.29	3.63	3.78	5.00	5.58	6.21	6.64	6.92	7.12	7.39	7.63	7.69	7.60	7.42	8.04	10.33	15.68
4.15	3.50	3.37	3.50	3.90	4.44	5.14	5.93	6.56	6.79	6.68	6.90	7.12	7.22	7.18	7.11	6.94	7.11	9.00	12.77
4.09	3.56	3.25	3.48	3.94	4.52	5.13	5.71	6.19	6.45	6.55	6.83	6.91	7.03	6.96	6.99	6.85	6.79	8.22	11.31
4.11	3.38	3.27	3.32	3.81	4.37	4.82	5.34	5.99	6.13	6.45	6.90	6.90	7.04	7.01	6.86	6.86	6.94	8.66	13.37
3.94	3.09	3.18	3.39	3.71	4.15	4.66	5.27	5.69	6.18	6.30	6.56	6.97	7.45	7.40	7.26	7.59	7.90	9.44	14.94
3.50	3.06	3.02	3.31	3.87	4.63	5.73	6.83	6.90	7.03	7.25	7.24	7.42	7.70	7.75	8.13	8.53	9.34	10.07	14.96

Fig. 54. Local Sherwood number ratios for Case S-1 at *Re*=7,000.

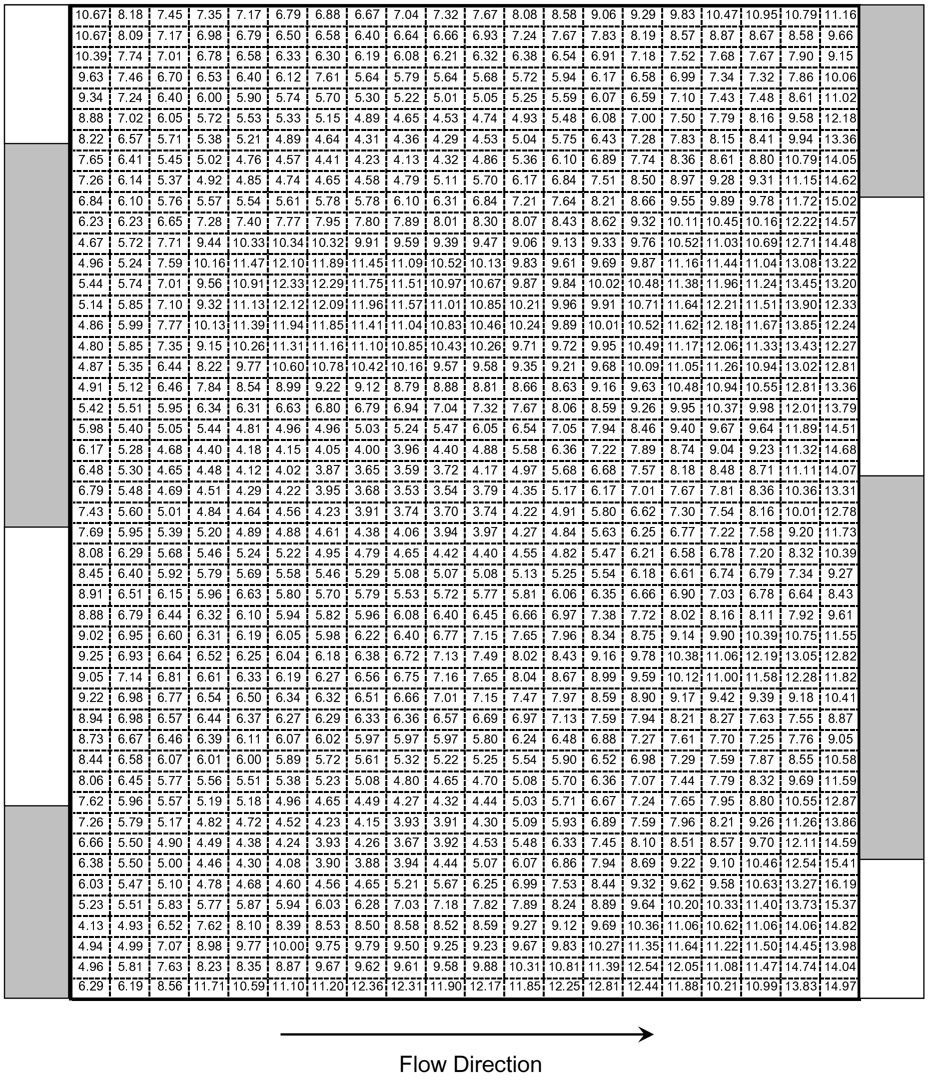

10.67	8.18	7.45	7.35	7.17	6.79	6.88	6.67	7.04	7.32	7.67	8.08	8.58	9.06	9.29	9.83	10.47	10.95	10.79	11.16
10.67	8.09	7.17	6.98	6.79	6.50	6.58	6.40	6.64	6.66	6.93	7.24	7.67	7.83	8.19	8.57	8.87	8.67	8.58	9.66
10.39	7.74	7.01	6.78	6.58	6.33	6.30	6.19	6.08	6.21	6.32	6.38	6.54	6.91	7.18	7.52	7.68	7.67	7.90	9.15
9.63	7.46	6.70	6.53	6.40	6.12	7.61	5.64	5.79	5.64	5.68	5.72	5.94	6.17	6.58	6.99	7.34	7.32	7.86	10.06
9.34	7.24	6.40	6.00	5.90	5.74	5.70	5.30	5.22	5.01	5.05	5.25	5.59	6.07	6.59	7.10	7.43	7.48	8.61	11.02
8.88	7.02	6.05	5.72	5.53	5.33	5.15	4.89	4.65	4.53	4.74	4.93	5.48	6.08	7.00	7.50	7.79	8.16	9.58	12.18
8.22	6.57	5.71	5.38	5.21	4.89	4.64	4.31	4.36	4.29	4.53	5.04	5.75	6.43	7.28	7.83	8.15	8.41	9.94	13.36
7.65	6.41	5.45	5.02	4.76	4.57	4.41	4.23	4.13	4.32	4.86	5.36	6.10	6.89	7.74	8.36	8.61	8.80	10.79	14.05
7.26	6.14	5.37	4.92	4.85	4.74	4.65	4.58	4.79	5.11	5.70	6.17	6.84	7.51	8.50	8.97	9.28	9.31	11.15	14.62
6.84	6.10	5.76	5.57	5.54	5.61	5.78	5.78	6.10	6.31	6.84	7.21	7.64	8.21	8.66	9.55	9.89	9.78	11.72	15.02
6.23	6.23	6.65	7.28	7.40	7.77	7.95	7.80	7.89	8.01	8.30	8.07	8.43	8.62	9.32	10.11	10.45	10.16	12.22	14.57
4.67	5.72	7.71	9.44	10.33	10.34	10.32	9.91	9.59	9.39	9.47	9.06	9.13	9.33	9.76	10.52	11.03	10.69	12.71	14.48
4.96	5.24	7.59	10.16	11.47	12.10	11.89	11.45	11.09	10.52	10.13	9.83	9.61	9.69	9.87	11.16	11.44	11.04	13.08	13.22
5.44	5.74	7.01	9.56	10.91	12.33	12.29	11.75	11.51	10.97	10.67	9.87	9.84	10.02	10.48	11.38	11.96	11.24	13.45	13.20
5.14	5.85	7.10	9.32	11.13	12.12	12.09	11.96	11.57	11.01	10.85	10.21	9.96	9.91	10.71	11.64	12.21	11.51	13.90	12.33
4.86	5.99	7.77	10.13	11.39	11.94	11.85	11.41	11.04	10.83	10.46	10.24	9.89	10.01	10.52	11.62	12.18	11.67	13.85	12.24
4.80	5.85	7.35	9.15	10.26	11.31	11.16	11.10	10.85	10.43	10.26	9.71	9.72	9.95	10.49	11.17	12.06	11.33	13.43	12.27
4.87	5.35	6.44	8.22	9.77	10.60	10.78	10.42	10.16	9.57	9.58	9.35	9.21	9.68	10.09	11.05	11.26	10.94	13.02	12.81
4.91	5.12	6.46	7.84	8.54	8.99	9.22	9.12	8.79	8.88	8.81	8.66	8.63	9.16	9.63	10.48	10.94	10.55	12.81	13.36
5.42	5.51	5.95	6.34	6.31	6.63	6.80	6.79	6.94	7.04	7.32	7.67	8.06	8.59	9.26	9.95	10.37	9.98	12.01	13.79
5.98	5.40	5.05	5.44	4.81	4.96	4.96	5.03	5.24	5.47	6.05	6.54	7.05	7.94	8.46	9.40	9.67	9.64	11.89	14.51
6.17	5.28	4.68	4.40	4.18	4.15	4.05	4.00	3.96	4.40	4.88	5.58	6.36	7.22	7.89	8.74	9.04	9.23	11.32	14.68
6.48	5.30	4.65	4.48	4.12	4.02	3.87	3.65	3.59	3.72	4.17	4.97	5.68	6.68	7.57	8.18	8.48	8.71	11.11	14.07
6.79	5.48	4.69	4.51	4.29	4.22	3.95	3.68	3.53	3.54	3.79	4.35	5.17	6.17	7.01	7.67	7.81	8.36	10.36	13.31
7.43	5.60	5.01	4.84	4.64	4.56	4.23	3.91	3.74	3.70	3.74	4.22	4.91	5.80	6.62	7.30	7.54	8.16	10.01	12.78
7.69	5.95	5.39	5.20	4.89	4.88	4.61	4.38	4.06	3.94	3.97	4.27	4.84	5.63	6.25	6.77	7.22	7.58	9.20	11.73
8.08	6.29	5.68	5.46	5.24	5.22	4.95	4.79	4.65	4.42	4.40	4.55	4.82	5.47	6.21	6.58	6.78	7.20	8.32	10.39
8.45	6.40	5.92	5.79	5.69	5.58	5.46	5.29	5.08	5.07	5.08	5.13	5.25	5.54	6.18	6.61	6.74	6.79	7.34	9.27
8.91	6.51	6.15	5.96	6.63	5.80	5.70	5.79	5.53	5.72	5.77	5.81	6.06	6.35	6.66	6.90	7.03	6.78	6.64	8.43
8.88	6.79	6.44	6.32	6.10	5.94	5.82	5.96	6.08	6.40	6.45	6.66	6.97	7.38	7.72	8.02	8.16	8.11	7.92	9.61
9.02	6.95	6.60	6.31	6.19	6.05	5.98	6.22	6.40	6.77	7.15	7.65	7.96	8.34	8.75	9.14	9.90	10.39	10.75	11.55
9.25	6.93	6.64	6.52	6.25	6.04	6.18	6.38	6.72	7.13	7.49	8.02	8.43	9.16	9.78	10.38	11.06	12.19	13.05	12.82
9.05	7.14	6.81	6.61	6.33	6.19	6.27	6.56	6.75	7.16	7.65	8.04	8.67	8.99	9.59	10.12	11.00	11.58	12.28	11.82
9.22	6.98	6.77	6.54	6.50	6.34	6.32	6.51	6.66	7.01	7.15	7.47	7.97	8.59	8.90	9.17	9.42	9.39	9.18	10.41
8.94	6.98	6.57	6.44	6.37	6.27	6.29	6.33	6.36	6.57	6.69	6.97	7.13	7.59	7.94	8.21	8.27	7.63	7.55	8.87
8.73	6.67	6.46	6.39	6.11	6.07	6.02	5.97	5.97	5.97	5.80	6.24	6.48	6.88	7.27	7.61	7.70	7.25	7.76	9.05
8.44	6.58	6.07	6.01	6.00	5.89	5.72	5.61	5.32	5.22	5.25	5.54	5.90	6.52	6.98	7.29	7.59	7.87	8.55	10.58
8.06	6.45	5.77	5.56	5.51	5.38	5.23	5.08	4.80	4.65	4.70	5.08	5.70	6.36	7.07	7.44	7.79	8.32	9.69	11.59
7.62	5.96	5.57	5.19	5.18	4.96	4.65	4.49	4.27	4.32	4.44	5.03	5.71	6.67	7.24	7.65	7.95	8.80	10.55	12.87
7.26	5.79	5.17	4.82	4.72	4.52	4.23	4.15	3.93	3.91	4.30	5.09	5.93	6.89	7.59	7.96	8.21	9.26	11.26	13.86
6.66	5.50	4.90	4.49	4.38	4.24	3.93	4.26	3.67	3.92	4.53	5.48	6.33	7.45	8.10	8.51	8.57	9.70	12.11	14.59
6.38	5.50	5.00	4.46	4.30	4.08	3.90	3.88	3.94	4.44	5.07	6.07	6.86	7.94	8.69	9.22	9.10	10.46	12.54	15.41
6.03	5.47	5.10	4.78	4.68	4.60	4.56	4.65	5.21	5.67	6.25	6.99	7.53	8.44	9.32	9.62	9.58	10.63	13.27	16.19
5.23	5.51	5.83	5.77	5.87	5.94	6.03	6.28	7.03	7.18	7.82	7.89	8.24	8.89	9.64	10.20	10.33	11.40	13.73	15.37
4.13	4.93	6.52	7.62	8.10	8.39	8.53	8.50	8.58	8.52	8.59	9.27	9.12	9.69	10.36	11.06	10.62	11.06	14.06	14.82
4.94	4.99	7.07	8.98	9.77	10.00	9.75	9.79	9.50	9.25	9.23	9.67	9.83	10.27	11.35	11.64	11.22	11.50	14.45	13.98
4.96	5.81	7.63	8.23	8.35	8.87	9.67	9.62	9.61	9.58	9.88	10.31	10.81	11.39	12.54	12.05	11.08	11.47	14.74	14.04
6.29	6.19	8.56	11.71	10.59	11.10	11.20	12.36	12.31	11.90	12.17	11.85	12.25	12.81	12.44	11.88	10.21	10.99	13.83	14.97

Fig. 55. Local Sherwood number ratios for Case S-4 at Re=7,000.

Table IV. Average Sherwood number ratios obtained from mass transfer measurement and their comparison with average Nusselt number ratios obtained from heat transfer measurement.

Case	Re	Sh/Sh_0			Nu/Nu_0	Deviation
		1^{st} segm.	2^{nd} segm.	3^{rd} segm.	2^{nd} segm.	2^{nd} segm.
S-1	7,000	6.51	6.54	6.54	6.07	7.3%
	17,000	6.18	6.18	6.12	5.64	8.8%
S-2	7,000		7.40		6.99	5.6%
	17,000		6.95		6.49	6.7%
S-3	7,000		7.80		7.41	4.9%
	17,000		7.31		6.72	8.0%
S-4	7,000	8.02	8.14	8.32	7.98	2.0%
	17,000	7.71	7.65	7.99	7.35	3.9%
L-1	7,000	6.13	5.86	5.78	5.61	4.3%
	17,000	5.72	5.46	5.55	5.29	3.1%
L-2	7,000		7.01		6.68	4.7%
	17,000		6.66		6.26	6.0%
L-3	7,000		6.98		6.56	6.0%
	17,000		6.51		6.23	4.3%
L-4	7,000	5.91	6.78	8.00	6.52	3.8%
	17,000	5.63	6.40	7.72	6.20	3.1%

APPENDIX B

CALCULATED DATA FOR HEAT TRANSFER MEASUREMENT

Table V. Average Nusselt numbers obtained from heat transfer measurement.

Case	Re	Nu			Nu_0	$\overline{Nu}/Nu_0$
		1^{st} segment	2^{nd} segment	3^{rd} segment		
S-1	7,000	145	143	139	23.6	6.10
	12,000	219	211	207	36.1	5.88
	17,000	283	271	266	48.0	5.69
S-2	7,000	172	165	155	23.6	6.94
	12,000	256	243	229	36.0	6.73
	17,000	326	311	294	47.9	6.47
S-3	7,000	182	175	175	23.6	7.51
	12,000	268	251	257	36.0	7.19
	17,000	345	321	331	47.7	6.96
S-4	7,000	190	188	186	23.6	7.94
	12,000	281	274	276	35.9	7.71
	17,000	360	350	352	47.5	7.44
L-1	7,000	142	133	128	23.7	5.67
	12,000	208	196	191	36.2	5.48
	17,000	270	256	249	48.3	5.35
L-2	7,000	152	158	166	23.7	6.69
	12,000	225	233	244	36.2	6.46
	17,000	292	302	316	48.2	6.29
L-3	7,000	146	156	168	23.7	6.59
	12,000	216	232	252	36.2	6.45
	17,000	280	300	326	48.2	6.27
L-4	7,000	142	156	178	24.0	6.63
	12,000	207	233	265	36.6	6.42
	17,000	268	302	343	48.6	6.26

Table VI. Average friction factors obtained with heat transfer measurement.

Case	Re	f			f_0	$\overline{f}/f_0$
		1^{st} segment	2^{nd} segment	3^{rd} segment		
S-1	7,000	28.2	25.8	25.6	0.0349	761
	12,000	28.8	26.1	25.7	0.0300	895
	17,000	28.9	25.9	25.4	0.0273	980
S-2	7,000	35.8	32.3	30.3	0.0349	941
	12,000	36.3	32.8	30.7	0.0300	1108
	17,000	36.5	32.8	30.8	0.0273	1222
S-3	7,000	39.9	42.7	42.7	0.0349	1196
	12,000	39.5	41.7	41.5	0.0300	1361
	17,000	39.3	40.9	40.8	0.0273	1476
S-4	7,000	45.4	52.2	54.3	0.0349	1451
	12,000	45.2	51.4	53.3	0.0301	1662
	17,000	45.1	50.9	53.1	0.0274	1815
L-1	7,000	12.4	10.6	10.5	0.0349	319
	12,000	12.9	10.8	10.7	0.0300	383
	17,000	13.1	11.0	10.7	0.0272	426
L-2	7,000	20.5	24.5	23.7	0.0348	658
	12,000	20.6	24.5	23.7	0.0300	765
	17,000	20.6	24.2	23.5	0.0272	836
L-3	7,000	21.2	27.6	29.6	0.0348	751
	12,000	21.4	27.7	29.8	0.0300	878
	17,000	21.1	27.1	29.4	0.0272	949
L-4	7,000	20.0	31.3	36.1	0.0347	840
	12,000	20.0	31.2	36.1	0.0299	974
	17,000	19.7	30.8	35.6	0.0272	1056

Table VII. Thermal performances obtained with heat transfer measurement.

Case	Re	TP			$\overline{TP}$
		1^{st} segment	2^{nd} segment	3^{rd} segment	
S-1	7,000	0.681	0.671	0.653	0.668
	12,000	0.616	0.613	0.603	0.611
	17,000	0.579	0.574	0.567	0.573
S-2	7,000	0.722	0.717	0.686	0.708
	12,000	0.666	0.654	0.632	0.651
	17,000	0.618	0.610	0.588	0.606
S-3	7,000	0.737	0.693	0.692	0.708
	12,000	0.681	0.625	0.642	0.649
	17,000	0.640	0.588	0.607	0.612
S-4	7,000	0.737	0.698	0.682	0.705
	12,000	0.682	0.639	0.635	0.652
	17,000	0.641	0.598	0.594	0.611
L-1	7,000	0.847	0.835	0.807	0.830
	12,000	0.761	0.760	0.743	0.755
	17,000	0.714	0.717	0.705	0.712
L-2	7,000	0.764	0.751	0.794	0.769
	12,000	0.704	0.688	0.728	0.707
	17,000	0.665	0.651	0.689	0.668
L-3	7,000	0.724	0.709	0.747	0.726
	12,000	0.668	0.658	0.698	0.675
	17,000	0.633	0.625	0.660	0.639
L-4	7,000	0.714	0.675	0.732	0.707
	12,000	0.648	0.627	0.679	0.651
	17,000	0.613	0.595	0.645	0.618

APPENDIX C

THERMOPHYSICAL PROPERTIES OF PF-5060

PF-5060 was selected as test fluid in this pool boiling experiment because of its frequent use in thermal management system. PF-5060 consists of 95% pure FC-72 (Molecular weight: 338 g/mol) and have thermophysical properties as summarized in the following table. In table VIII, the properties of the test liquid in vapor phase are estimated at atmospheric pressure based on the correlation provided by the manufacturer (3M Company).

Table VIII. Thermophysical properties of PF-5060.

	Unit	Liquid	Vapor
Density	kg/m^3	1610.68	12.52
Kinematic Viscosity	m^2/s	2.78×10^{-7}	1.15×10^{-6}
Prandtl Number	s	9.8	0.81
Specific Heat	$J/kg \cdot K$	1132.62	651
Thermal Conductivity	$W/m \cdot K$	0.0539	0.0124
Surface Tension	N/m	8.448×10^{-3}	-
Latent Heat of Vaporization	J/kg	85034.34	-
Saturation Temperature	°C	56	56

APPENDIX D

CALCULATED DATA FOR POOL BOILING ON MWCNT ARRAYS

Table IX. The wall heat fluxes and associated wall superheats in the vicinity of the CHF and MHF points.

Type	Liquid condition	Critical heat flux		Minimum heat flux	
		($\times 10^{-4}$)	Superheat	($\times 10^{-4}$)	Superheat
Bare Si	saturation	3.3	39	1.3	58
	5°C sub-cooling	3.7	40	1.6	59
	10°C sub-cooling	4.1	40	1.8	68
Type-A	saturation	4.9	19	1.2	50
	5°C sub-cooling	5.3	21	1.4	55
	10°C sub-cooling	5.4	17	1.5	56
Type-B	saturation	5.5	20	2.4	58
	5°C sub-cooling	6.0	22	2.8	68
	10°C sub-cooling	6.7	22	3.3	73

VITA

Hee Seok Ahn

Education:

B.S. Mechanical Engineering, Korea University, Seoul, 1988.

M.S. Mechanical Engineering, Korea University, Seoul, 1990.

Ph.D. Mechanical Engineering, Texas A&M University, College Station, 2007.

Permanent Address:

Kunyung Apt. 102-1608, Sangbong-1-Dong, Joongrang-Gu, Seoul, Korea.

The typist for this dissertation was Hee Seok Ahn.